Applications and Mechanisms of Epitaxy

on Graphene-terminated Surfaces

by

Sebastian O. Manzo

A dissertation submitted in partial fulfilment of

the requirements for the degree of

Doctor of Philosophy

(Materials Science and Engineering)

at the

UNIVERSITY OF WISCONSIN – MADISON

2023

Date of final oral examination: 08/30/2023

The dissertation is approved by the following members of the Final Oral Committee:

Jason K. Kawasaki, Associate professor, Materials Science & Engineering

Michael S. Arnold, Professor, Materials Science & Engineering

Chang-Beom Eom, Professor, Materials Science & Engineering

Luke J. Mawst, Professor, Electrical & Computer Engineering

Daniel A. Rhodes, Assistant professor, Materials Science & Engineering

A mis papás y a mi fiel amigo Rubén

Acknowledgements

And life confided the secret to me: behold, it said, I am that which must always overcome itself.

– Thus Spoke Zarathustra

First and foremost, I would like to thank my parents. A few sentences here are nowhere near enough to express my appreciation for them, nevertheless I will try my best. My parents are remarkably intelligent and have been overachievers their entire lives. They have paved the way for me and given me access to numerous opportunities that have made it easy for me to succeed. They have always trusted me, supported me, and challenged me. Since I was a boy, they told me that I could overcome any obstacle through perseverance. They taught me that being mediocre is a choice and that failure is part of becoming better. Their incredible curiosity has rubbed off on me and I am sure I would not have pursued a Ph. D. without it. They have taken me to countless museums, cities and natural wonders all over the world. We have had deep conversations about life and have laughed hysterically together after sharing a dumb joke. I am impossibly lucky to have them as my family. ¡Gracias y los quiero mucho!

I would also like to thank my advisor, Jason Kawasaki. He is probably the smartest and hardest working person I have ever met. His optimism and excitement about research are truly contagious and have motivated me when I was feeling

pessimistic about my projects. He has been incredibly patient with me throughout my Ph. D., and I am very grateful for that. His honesty and openness make him remarkably approachable, and I think that is one of his greatest strengths. Working with Jason has been an eye-opening experience and his mentorship these past five years has made me a better researcher and person. Jason is a very creative and intelligent advisor, but beyond that, he is a great person. Thank you, Jason.

I would like to thank Patrick Strohbeen, Estiaque Shourov, Dongxue Du, Zheng-Hui Lim, Zachary LaDuca, Josh Eickoff, Taehwan Jung, Kayla Lloyd and Tamalika Samanta from my group and Katherine Su and Christopher Blackwell from Prof. Michael Arnold's group for their friendship these past five years. Without them, graduate school would have been a much more difficult experience. I want to especially thank Patrick, Estiaque and Dongxue, who showed me the ropes as a first-year graduate student and taught me a tremendous amount about MBE growth and maintenance. They were happy to answer my questions and were an invaluable resource as a young researcher.

I also want to acknowledge my family in Mexico, especially my grandparents. I know they wish they could see me more, but every time I do see them, I become revitalized by their love and care. Seeing how proud my family is of my accomplishments has motivated me to keep working hard in times of struggle.

I also want to take this opportunity to thank my brothers Hugh Lovrić, Abdullah Khan, Alexander Hocken, and Olukorede Esan. Seeing them throughout my Ph. D. degree recharged my batteries and motivated me during tough times. Our friendship is something I value tremendously, and they know that I will always be there for them.

Last but not least, I want to thank my undergraduate research advisor at Penn State University, Professor Joshua Robinson. Without him, I would have never gone to graduate school. When I approached him to join his research group, I had quite a rough semester academically and I half-expected him to say no. To my surprise, he welcomed me with open arms. His faith in me motivated me to become a better student and researcher. I had no plans to do a Ph. D. as an undergraduate student until he suggested I apply, because I never saw myself as someone who could do a Ph. D. He made me realize that I was capable of doing it. I am grateful that he took a chance on me and pushed me to pursue this challenging journey.

In truth, this acknowledgements section could be longer than this whole dissertation. I am incredibly grateful and lucky for everyone that has supported me throughout my life and academic career. Gracias, thank you, dankeschön and tusen takk.

Table of contents

Curriculum Vitae

Sebastian O. Manzo

smanzoj@outlook.com

Education

Doctor of Philosophy in Materials Science & Engineering, 2023

University of Wisconsin – Madison, Madison WI

Advisor: Jason K. Kawasaki

Bachelor of Science in Materials Science & Engineering, 2018

Pennsylvania State University, State College PA

Advisor: Joshua A. Robinson

Publications

Underlined entries are publications that are included in this document.

1. **S. Manzo**, P. J. Strohbeen, Z. H. Lim, V. Saraswat, D. Du, S. Xu, N. Pokharel, L. J. Mawst, M. S. Arnold, and J. K. Kawasaki, *Pinhole-Seeded Lateral Epitaxy and Exfoliation of GaSb Films on Graphene-Terminated Surfaces*, Nat. Commun. **13**, 1 (2022).
2. **S. Manzo**, K. Su, M. S. Arnold, and J. K. Kawasaki, *Nucleation selectivity and lateral coalescence of GaAs over graphene on Ge (111)*, Manuscript submitted for publication, (2023).
3. P. J. Strohbeen, **S. Manzo**, V. Saraswat, K. Su, M. S. Arnold, and J. K. Kawasaki, *Quantifying Mn Diffusion through Transferred versus Directly Grown Graphene Barriers*, ACS Appl. Mater. Interfaces **13**, 42146 (2021).
4. Du, **S. Manzo**, C. Zhang, V. Saraswat, K. T. Genser, K. M. Rabe, P. M. Voyles, M. S. Arnold, and J. K. Kawasaki, *Epitaxy, Exfoliation, and Strain-Induced Magnetism in Rippled Heusler Membranes*, Nat. Commun. **12**, 1 (2021).

5. Z. H. Lim, **S. Manzo**, P. J. Strohbeen, V. Saraswat, M. S. Arnold, and J. K. Kawasaki, *Selective Area Epitaxy of GaAs Films Using Patterned Graphene on Ge*, Appl. Phys. Lett. **120**, 051603 (2022).

6. D. Du, T. Jung, **S. Manzo**, Z. LaDuca, X. Zheng, K. Su, V. Saraswat, J. McChesney, M. S. Arnold, and J. K. Kawasaki, *Controlling the Balance between Remote, Pinhole, and van Der Waals Epitaxy of Heusler Films on Graphene/Sapphire*, Nano Lett. **22**, 8647 (2022).

7. Z. LaDuca, K. Su, **S. Manzo**, M. S. Arnold, and J. K. Kawasaki, *Control of Ternary Alloy Composition during Remote Epitaxy on Graphene*, Phys. Rev. Mater. **7**, 083401 (2023).

8. V. Saraswat et al., *Bottom-up Synthesis of Mesoscale Nanomeshes of Graphene Nanoribbons on Germanium*, APL Mater. **11**, 041123 (2023).

9. H. Yoon et al., *Freestanding Epitaxial SrTiO3 Nanomembranes via Remote Epitaxy Using Hybrid Molecular Beam Epitaxy*, Sci. Adv. **8**, eadd5328 (2022).

Abstract

Applications and Mechanisms of Epitaxy

on Graphene-terminated Surfaces

by Sebastian O. Manzo

Remote epitaxy is a method for growing single-crystalline films on a graphene-terminated single-crystalline substrate, in which the epitaxial registry occurs between film and substrate rather than film and graphene. In an idealized picture, it has been argued that epitaxial registry between film and substrate originates from potential fluctuations of polar substrates that penetrate the graphene and template the overlayer [1]. The main advantage of this approach is the absence of direct bonding between the underlying substrate and the film, making it attractive for various applications like highly mismatched heteroepitaxy, graphene-diffusion barriers and the production of single crystalline, flexible membranes. However, the atomic scale mechanisms for remote epitaxy remain unclear because most experiments have relied on post growth analysis of very thick films (several microns), making it difficult to distinguish a remote epitaxy mechanism from alternative mechanisms. In this dissertation, I focus on elucidating the atomistic

mechanisms of remote epitaxy through *ex-situ* and *in-situ* tools and comment on some of the applications enabled by growth on graphene-terminated surfaces.

First, I focus on the most commonly used system for remote epitaxy: transferred graphene on III-V semiconductor substrates. Using the standard cleaning and transfer procedures, we find that pinholes are created in the graphene immediately prior to growth, due to desorption of trapped interfacial oxides at the graphene/III-V interfaces. Crucially, our AFM and SEM studies show that these pinholes are the preferred sites for direct nucleation on the substrate, and that subsequent growth proceeds laterally until full coalescence of GaSb films on graphene/GaSb. Pinhole-seeded epitaxy can produce single-crystalline, exfoliateable membranes, thereby replicating the features of remote epitaxy via an alternate mechanism.

Understanding the possible intrinsic mechanism for remote epitaxy requires very clean graphene/substrate interfaces with a low concentration of pinholes. Model calculations of idealized graphene/substrate interfaces suggest that lattice potential fluctuations through graphene are very weak ($\Delta\varphi$ = 0-40 meV) [1,2], smaller than the thermal energy k_BT (~ 70 meV) at a typical growth temperature of 500 °C. It is unclear how such a low potential could template the growth. As a result, we hypothesize that step-edges provide larger potential fluctuations, which may be transmitted through draped graphene to seed epitaxy to the substrate. I grow

GaAs on gr/Ge (111), a system which has a much lower defect-density than transferred graphene and perform *ex-situ* microscopy measurements to see where GaAs is nucleating. I find that nucleation on clean graphene occurs at defective wrinkles and at step-edges. These results suggest that epitaxy on graphene might not require a polar substrate if sites with enhanced lattice potential fluctuations, like step-edges, are available on the surface. I also comment on related work conducted by my group member Dongxue Du, who discovered a 30°-rotated domain of GdPtSb grown on clean gr/sapphire which cannot be explained by pinhole or van der Waals epitaxy. I also explore other possibilities that could result in epitaxy on graphene such as intercalation and metal carbide formation.

Epitaxial lateral overgrowth using graphene masks is another promising growth approach that enables exfoliateable films with reduced defect densities. However, a clear understanding of the related kinetic factors that control nucleation selectivity and lateral coalescence is missing. I investigate the influence of various growth conditions such as temperature, atomic flux ratio and growth rate on the molecular beam epitaxial (MBE) growth of GaAs on partial coverage graphene masks on Ge (111). Microscopy, in-situ electron diffraction and photoemission demonstrate that elevated growth temperatures (T > 600 °C), low As/Ga flux ratios (~ 28) and moderate growth rates (~ 56 nm/h) improve surface diffusion and

desorption rates, promoting excellent selective nucleation and full coalescence of films within 400 nm.

Lastly, I comment on some of the unique advantages of growing films on graphene-terminated substrates. We show that graphene successfully blocks metal interdiffusion into semiconductor substrates, which paves the way for growing lattice-matched Heusler alloys on graphene-terminated semiconductors for spintronic applications. Furthermore, films grown on graphene can be readily exfoliated to produce flexible single-crystalline membranes. We find that rippling GdPtSb and GdAuGe membranes allows us to access extreme strain states that give rise to magnetic and superconducting phases.

1 Introduction

1.1 Epitaxy on van der Waals solids

Epitaxy comes from the Greek prefix *epi* meaning "above" and *taxia* meaning "arrangement". It is a process to synthesize crystalline films on crystalline substrates. Atoms that are deposited on the substrate will arrange themselves into epitaxial layers that are aligned with the underlying crystal. When the film and substrate are chemically identical, the process is known as homoepitaxy. Heteroepitaxy is the synthesis of a material that is different than the substrate. This technique has led to remarkable discoveries in the field of solid-state physics. Some examples include the growth of HgTe/(Hg,Cd)Te quantum wells — the first realization of a 2D topological insulator [3], the observation of a high mobility electron gas at the $LaAlO_3/SrTiO_3$ interface [4], and many more. In addition, several commercial electronic and photonic technologies rely on epitaxy, such as HgCdTe infrared detectors [5], InGaP/GaAs high-efficiency multi-junction solar cells [6] and InGaAs/AlInAs quantum cascade lasers [7], to name a few.

Epitaxy allows for unprecedented control over the synthesis process, which can result in novel layered structures with atomically abrupt interfaces and exceptional crystal quality. Unfortunately, conventional epitaxy has a strict set of requirements to achieve high-quality films such as matching symmetry, polarity,

and lattice and thermal constants between film and substrate. If these conditions are not met, defective interfaces will be the result, which will lead to diminished device performance. Consequently, growing materials with innovative properties and integrating these with readily accessible substrates is a substantial challenge. There have been great efforts to overcome the compatibility issues between film and substrate. One such approach, known as van der Waals epitaxy (vdWE), involves growing films on 2-dimensional layered materials (2DLMs), such as graphene.

Layered materials that have van der Waals cleavage planes have atomically sharp interfaces with no dangling bonds [8]. In other words, van der Waals crystals are held together by strong covalent forces in-plane and weak van der Waals forces out-of-plane. As a result, the weakly coupled layers of these materials can be easily peeled off. This led to the isolation of graphene using the scotch tape method [9]. The momentous characterization of graphene by Geim and Novoselov in 2004 drove the discovery of many other promising 2DLMs [10–12]. This class of materials have demonstrated novel electronic band structures and fascinating optical properties [13–18]; here, we shall focus on their potential use as a growth substrate and the advantages that they might provide over conventional 3D bulk crystals.

Conventional epitaxy results in direct covalent or ionic bonding at the interface between film and substrate. As a result, the overlayer must share a similar

crystal structure and lattice constant for pseudomorphic growth to occur. On the other hand, in van der Waals epitaxy, weak dispersion forces are the predominant bonding mechanism. The absence of strong covalent bonds allows for complete strain relaxation between two highly mismatched materials [19]. VdwE has been studied for decades as a potential growth method to overcome lattice mismatch, ever since Koma *et al.* first proposed it [20]. The lack of broken bonds at the vdW-interface does mean that vdWE is typically incommensurate, where no orientational relationship between film and substrate exists. However, it has been found that certain systems do exhibit long-range commensurability, even in 3D-on-2D systems [21–23]. When this occurs the epilayer takes on the out-of-plane orientation associated with the lowest energy facet of its crystal structure. For example, in cubic systems, the (111) orientation would be favored [24,25]. Most work to date has focused on the vdWE of 2DLMs on other layered materials to create novel van der Waals heterostructures [10,12,26–29].

1.2 Remote epitaxy

In 2017 Kim *et al.* from MIT proposed a new mechanism for the growth of 3D single-crystalline films on graphene, coined remote epitaxy [2]. This work was motivated by previous studies on the so called “long range effect” through amorphous layers. Several papers published in the mid-70s reported that

crystallographic information from the substrate could be transferred through thin amorphous layers, resulting in single-crystalline overlayers [30–32]. It is worth noting that these results were not without controversy. Other researchers proposed that the amorphous layers were not continuous, resulting direct epitaxy and lateral overgrowth at porous sites on the substrate [33]. Instead of utilizing amorphous layers, Kim *et al*. transferred graphene to single crystal semiconductor substrates, and claimed that a similar "long range effect" could take place [1]. Thick, singly-oriented GaAs films grown on gr/GaAs (001) were in epitaxial registry with the underlying substrate despite the presence of a graphene interlayer [2]. Due to the weak van der Waals interface, the GaAs films could be exfoliated and stacked onto arbitrary substrates, which enabled the substrate to be reused [2].

The key distinction between remote epitaxy and vdWE is that in vdWE the 2DLM serves as the epitaxial seed for crystal growth, which can lead to film orientations that are different to that of the single-crystalline substrate. For most device applications and from the perspective of technological relevance and scalability, this is not favored. The main benefit of remote epitaxy is that the underlying substrate templates the growth without directly bonding with the film. This could make graphene a perfect diffusion barrier material, since it could block adatoms from forming parasitic phases with the substrate, while still allowing for epitaxy [34]. In addition, the same group from MIT demonstrated that mismatched

heteroepitaxy on a graphene-terminated substrate resulted in reduced dislocation densities when compared to direct epitaxy [35]. Raman spectroscopy and STEM geometric phase analysis confirmed that the epilayer underwent spontaneous relaxation on graphene after a critical thickness. Their density functional theory calculations indicated that "slipping" at the interface is more energetically favorable than the formation of misfit dislocations up to a certain lattice mismatch [35].

Clearly, "remote epitaxy" holds a lot of promise, but how does it work? It was theorized that graphene acts as a semi-transparent layer that allows potential fluctuations from the substrate to permeate through it [1]. This "penetration distance" of these fluctuations is dictated by the substrate polarity. In fact, it was shown that "remote epitaxy" on multilayer graphene could still be conducted if the substrate was sufficiently polar [1]. According to this explanation, elemental semiconductor substrates such as silicon or germanium would not support the growth of single-crystalline films on top of graphene. Although the origin of this mechanism sounds plausible, a rigorous atomistic understanding of nucleation, diffusion and desorption on graphene-terminated substrates, is missing. The effect of graphene defects on the growth mechanism has also not been addressed. Furthermore, demonstrations of remote epitaxy outside of MIT remain sparse and the proposed explanation has garnered some skepticism and controversy. The

following chapters will address unanswered questions regarding remote epitaxy and how growing on graphene might be exploited for various applications.

1.3 Scientific questions

The overarching goal of this body of work is to elucidate the mechanisms of epitaxy on graphene-terminated surfaces through rigorous microscopic and spectroscopic characterization. We seek to understand all the possible mechanisms that result in epitaxy on graphene and explore ways in which we can exploit these novel growth techniques to expand the functionality of Heusler alloys, a materials system with rich diversity in electronic, magnetic, topological, and elastic properties [36–41]. Below is a breakdown of the of questions we seek to answer to achieve these goals and the corresponding sections that address them.

1.3.1 Can remote epitaxy occur in defective graphene/substrate interfaces?

Chapter 2 demonstrates that transferred graphene is not the idealized, pristine surface that previous remote epitaxy works assumed it to be. We find that graphene transferred to GaSb and GaAs leads to substantial defect formation due to thermal desorption of the native oxide through graphene. These defects are nucleation sites that seed film growth on graphene, which eventually leads to lateral overgrowth and coalescence. We could also exfoliate our films, which means we

have replicated the features of remote epitaxy without having to use “remote interactions” to explain the growth.

1.3.2 How does nucleation proceed in clean graphene-covered surfaces?

We explore where GaAs nucleation takes place on the cleaner gr/Ge (111) system in section 3.3 and find promising signs of step-flow -like nucleation enabled by draped graphene over Ge step edges. Furthermore, section 3.4 discusses the balance of vdWE, remote epitaxy and pinhole-seeded epitaxy through the growth of GdPtSb, LaPtSb and GdAuGe on gr/sapphire. We find a 30°-rotated domain in GdPtSb films grown on graphene which cannot be explained by a pinhole or vdW mechanism. Lastly, we discuss an important complication when growing stoichiometric films on graphene-covered surfaces in section 3.5, namely low sticking coefficients of metals on graphene.

1.3.3 What are the kinetic factors that control nucleation selectivity and coalescence of films on graphene?

Building from chapter 2 and 3, in chapter 4 we study the kinetic factors that control nucleation selectivity and lateral coalescence during epitaxial lateral overgrowth of GaAs on graphene masks. We report the optimal growth conditions, such as growth temperature, As/Ga atomic flux ratio, and growth rate to enhance nucleation selectivity and obtain coalesced films over graphene.

1.3.4 What are some other epitaxial growth mechanisms enabled by graphene besides van der Waals epitaxy and remote epitaxy?

In chapter 5 we explore the possibility of intercalation and/or carbide formation during film growth on graphene-terminated surfaces. We see signs that Ga intercalation might be taking place in gr/Ge. In addition, after depositing and annealing Gd on highly oriented pyrolytic graphite, we find evidence for Gd_2C formation through x-ray diffraction measurements. We also comment on forming Gd-carbides on graphene/sapphire.

1.3.5 Can we exploit growth on graphene to expand the functionality of Heusler compounds?

We present two cases that demonstrate graphene's potential as a growth substrate for Heusler alloys in chapter 6. First, we quantity graphene's diffusion barrier performance by growing and annealing Mn on graphene while tracking the Mn core level intensity via *in-situ* photoemission. Our results show that transferred and directly grown graphene successfully blocks Mn diffusion on semiconductor substrates. We also demonstrate that crystalline Heusler membranes can be produced by exfoliating from gr/Ge and gr/sapphire. We ripple these membranes and access extreme strain states that give rise to novel properties such as magnetism and superconductivity.

2 Pinhole-seeded lateral epitaxy on graphene-terminated surfaces

This chapter is adapted from the following article:

S. Manzo, P. J. Strohbeen, Z. H. Lim, V. Saraswat, D. Du, S. Xu, N. Pokharel, L. J. Mawst, M. S. Arnold, and J. K. Kawasaki, *Pinhole-Seeded Lateral Epitaxy and Exfoliation of GaSb Films on Graphene-Terminated Surfaces*, Nat. Commun. **13**, 1 (2022).

Author contribution: I performed graphene layer transfers, GaSb film growth and exfoliation, characterization of structure and morphology (AFM, SEM, Raman, XRD, RHEED) and the associated data analysis.

2.1 Abstract

Remote epitaxy is a promising approach for synthesizing exfoliateable crystalline membranes and enabling epitaxy of materials with large lattice mismatch. However, the atomic scale mechanisms for remote epitaxy remain unclear. Here we experimentally demonstrate that GaSb films grow on graphene-terminated GaSb (001) via a seeded lateral epitaxy mechanism, in which pinhole defects in the graphene serve as selective nucleation sites, followed by lateral epitaxy and coalescence into a continuous film. Remote interactions are not

necessary in order to explain the growth. Importantly, the small size of the pinholes permits exfoliation of continuous, free-standing GaSb membranes. Due to the chemical similarity between GaSb and other III-V materials, we anticipate this mechanism to apply more generally to other materials. By combining molecular beam epitaxy with in-situ electron diffraction and photoemission, plus ex-situ atomic force microscopy and Raman spectroscopy, we track the graphene defect generation and GaSb growth evolution a few monolayers at a time. Our results show that the controlled introduction of nanoscale openings in graphene provides an alternative route towards tuning the growth and properties of 3D epitaxial films and membranes on 2D material masks.

2.2 Introduction

Remote epitaxy of three-dimensional materials on graphene-terminated surfaces [2] promises to circumvent many of the limitations of conventional epitaxy. For example, the weak van der Waals interaction between the film and graphene creates new strain relaxation pathways for highly mismatched growth [35,42] and enables exfoliation of free-standing crystalline membranes for flexible devices [2,43] and tuning properties via strain in novel geometries [44]. Since the first demonstrations for compound semiconductors [1,2] epitaxy and exfoliation from graphene have been demonstrated for a variety of other materials

including transition metal oxides [43,45], simple metals [46], halide perovskites [42], and intermetallic compounds [44]. These films are typically thought to grow via a remote epitaxy mechanism [1,2], in which epitaxial registry between film and substrate is achieved via remote interactions that permeate through graphene.

The atomic scale mechanisms of remote epitaxy, however, remain unclear. Model calculations suggest that for perfect graphene/substrate interfaces, the substrate lattice potential permeates through graphene and may be sufficient to template epitaxial growth [1,2,42,46]. However, the magnitude of the potential fluctuations is only $\Delta\phi$ = 0 - 40 meV, which is smaller than the k_BT ~ 70 meV thermal energy at typical growth temperatures 500 °C. Experimentally, the ability to grow and exfoliate crystalline films from graphene is often cited as evidence for growth via these remote (screened) interactions [2,42,45]. In practice, however, it remains an outstanding challenge to fabricate defect-free graphene or perfect graphene/substrate interfaces, especially because graphene cannot be grown directly on arbitrary substrates. Additional layer transfer steps are often required. The effects of native and transfer-induced defects in graphene, which are difficult to control [47–50], are generally overlooked in the remote epitaxy mechanism. Microscopic measurements during growth are required to understand the atomic-scale mechanisms for growth under realistic conditions.

Here we experimentally demonstrate that pinhole-seeded lateral epitaxy explains the growth of atomically smooth, exfoliateable GaSb films on a graphene-terminated GaSb (001) substrate. Using the same graphene transfer procedures as previous reports [2,42,51], we find that pinholes are created by native oxide desorption from the substrate. GaSb nucleates directly from the underlying GaSb substrate in the pinholes, followed by lateral overgrowth and coalescence of a continuous film. The resulting films have similar structural quality as previous reports [1,2,35,42,43,46] and can be exfoliated to produce free-standing membranes. Since GaSb shares similar bonding character, constituent vapor pressures, surface diffusion coefficients, and growth conditions as other III-V materials, we anticipate that the seeded lateral epitaxy mechanism may explain the growth of other materials on transferred graphene. We experimentally track the evolution of GaSb films grown on graphene/GaSb(001) by combining molecular beam epitaxy (MBE) synthesis with in-situ electron diffraction and photoemission spectroscopy (XPS), plus ex-situ atomic force microscopy (AFM) and scanning electron microscopy (SEM).

This growth mode is conceptually similar to selective area epitaxy and epitaxial lateral overgrowth (ELO), that employ openings in a dielectric mask such as SiO_2 to seed growth [52–56]. It improves upon conventional ELO in two key ways. First, due to the weak Van der Waals interactions and small pinholes (10 -

300 nm diameter), graphene masks permit the etch-free exfoliation of large-scale single-crystalline GaSb membranes for applications in flexible electronics. Second, the atomic thinness of graphene is an attractive feature compared to conventional ELO masks, for applications where an electronically transparent interface is desired, e.g. a tunnel junction [57,58]. Seeded lateral epitaxy also carries an advantage over purely remote epitaxy: whereas remote epitaxy is only expected to apply for substrates with polar bonding [1], seeded lateral epitaxy can produce epitaxial films on nonpolar substrates [53]. Remote epitaxy also requires clean graphene/substrate interfaces, free from interfacial oxides or other contaminants [2]. Our experiments demonstrate that the introduction of defects provides powerful knob for controlling epitaxial growth of covalent 3D materials on 2D materials surfaces, similar to recent work on growth of 2D materials on patterned 2D masks [59,60].

2.3 Results

2.3.1 Epitaxy and exfoliation of GaSb films

We first demonstrate the epitaxy and exfoliation of single crystalline GaSb films on a graphene-terminated GaSb (001) substrate. Fig. 2.1 (a,b) shows reflection high energy electron diffraction (RHEED) patterns tracking the MBE-growth of GaSb directly on GaSb (001) and on graphene-terminated GaSb (001).

On this sample, we layer transfer graphene on half of the GaSb (001) substrate using a wet transfer procedure similar to the one that has previously been used for remote epitaxy of GaAs, including an HCl etch to remove native oxides from the substrate [2,51] (Methods). HCl [61–63] and HCl+H_2O_2 solutions [64,65] are also commonly used to etch native oxides from GaSb. The other half of the sample has an exposed GaSb surface for direct epitaxy.

Immediately prior to growth we follow the standard procedure of annealing at 520 °C in an Sb_2/Sb_1 flux to desorb the native oxides from the substrate. On the bare GaSb side, the native oxide removal is confirmed by the appearance of bright semi-streaky spots in the RHEED pattern. The graphene-terminated side looks qualitatively similar, although the pattern is not as bright and there is diffuse intensity around the specular reflection. We attribute these differences in part to scattering through monolayer graphene that is randomly oriented in-plane.

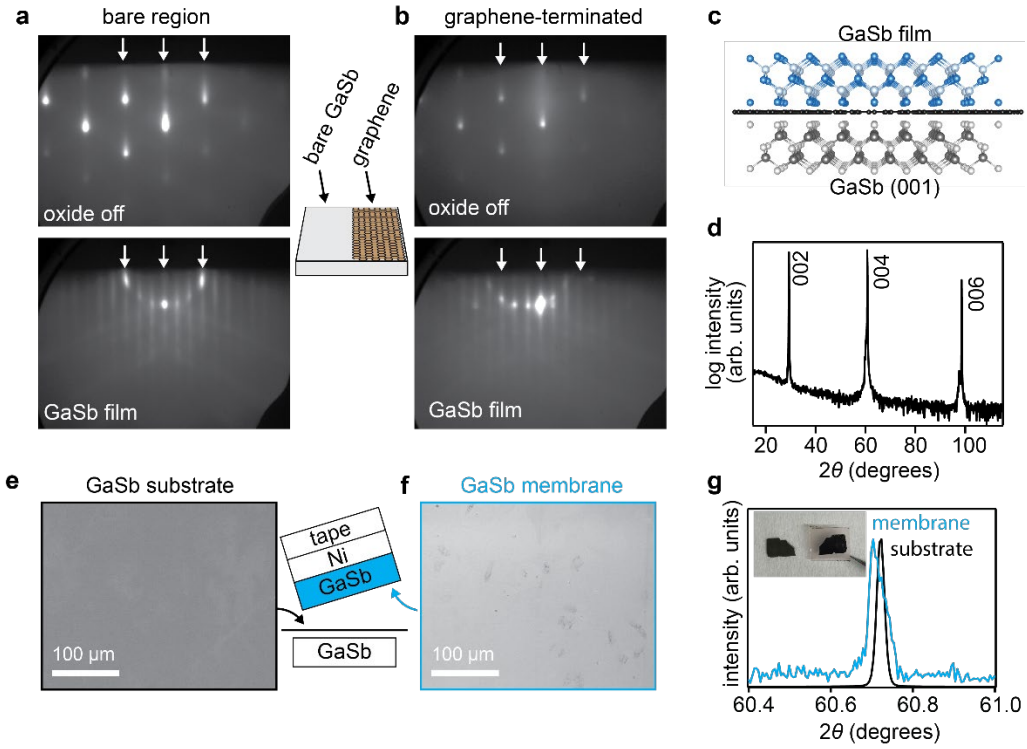

Figure 2.1 - Epitaxy and exfoliation of GaSb on graphene-terminated GaSb (001). (a-d) GaSb epitaxy on a GaSb (001) substrate that is half covered with graphene. (a) Reflection high energy electron diffraction (RHEED) patterns along a [1$\bar{1}$0] azimuth, tracking direct epitaxy on the exposed GaSb region. RHEED after the oxide off step shows a bright three-dimensional pattern. After 75 nm of film growth, an atomically smooth ring of spots RHEED pattern is recovered. (b) RHEED patterns tracking oxide desorption and growth on the graphene-terminated half of the substrate. (c) Schematic of the heterostructure. (d) X-ray diffraction pattern of the GaSb film grown on the graphene-terminated side of GaSb (001). (e-g) GaSb membrane exfoliation using a Ni stressor layer. (e) SEM image of the underside of the exfoliated GaSb membrane. The inset schematic illustrates the exfoliation. (f) SEM images of the substrate after exfoliation. (g) X-ray diffraction patterns of the 004 reflection for the exfoliated GaSb membrane (blue) and the GaSb substrate (black). Insert: example photo of the substrate (left) and GaSb membrane (right) after exfoliation. Membrane dimensions are approximately 10 mm by 6 mm.

After 75 nm of GaSb film growth, on both sides of the sample we observe a distinct ring of spots RHEED pattern with 3× superstructure reflections corresponding to the expected *c*(2×6) reconstruction of GaSb (001) [Fig.2.1a, b, bottom]. The clear superstructure indicates that a well-ordered, smooth epitaxial film has grown on both the bare substrate side and, on the graphene-terminated side. X-ray diffraction measurements confirm epitaxial GaSb growth with no impurity phases or orientations (Fig. 2.1d). Closer inspection of the 006 reflection reveals a subtle shift of the film reflection to lower angle compared to the substrate, or a larger out-of-plane lattice parameter. We speculate that this shift may arise from strain induced by the underlying graphene, e.g. due to the large thermal expansion mismatch between graphene and GaSb. Alternatively, the shift may be due to slight wrinkling of the GaSb film since it resting on a graphene interlayer. XRD rocking curves reveal a similar picture. In the rocking curves of the 004 reflection for a 120 nm GaSb film on graphene/GaSb (Supplementary Figure A.1), in addition to the expected peak at $\omega = 0$, we observe a second peak shifted by $\omega = -15$ arc seconds. The full width at half maxima (fwhm) of these two peaks are 10.44 and 12.59 arc seconds, respectively, compared to a width of 6.74 arc seconds for a homoepitaxial film. In addition, photoluminescence measurements reveal similar materials quality between films grown on graphene/GaSb (001) and a bare GaSb substrate (Supplementary Figure A.2).

Our GaSb films can be mechanically exfoliated from the graphene-terminated side of the sample, using a Ni stressor layer (Methods). Figs. 2.1 (e,f) show scanning electron micrographs of the top side of the substrate and the bottom side of the exfoliated membrane, after exfoliation. The large scale SEM images are comparable to previous demonstrations of remote epitaxy of other III-V materials, including GaAs and InP [1,2], and show minimal spalling marks or tears. ω-2θ X-ray diffraction measurements of the exfoliated membranes (Fig. 2.1g, blue curve) confirm that the membrane itself is single crystalline. We find that the 004 reflection of the membrane is slightly shifted the lower angle and slightly asymmetric compared to the substrate 004 reflection. We attribute these differences to strain, ripples, or slight mis-alignments when measuring thin (75 nm) exfoliated membranes.

2.3.2 Pinholes created by native oxide desorption

We now show that GaSb films grow on graphene-terminated GaSb (001) via a lateral epitaxy, seeded at pinhole defects. We first examine the creation of pinhole defects in graphene, which form due to native oxide desorption from the substrate immediately prior to GaSb film growth.

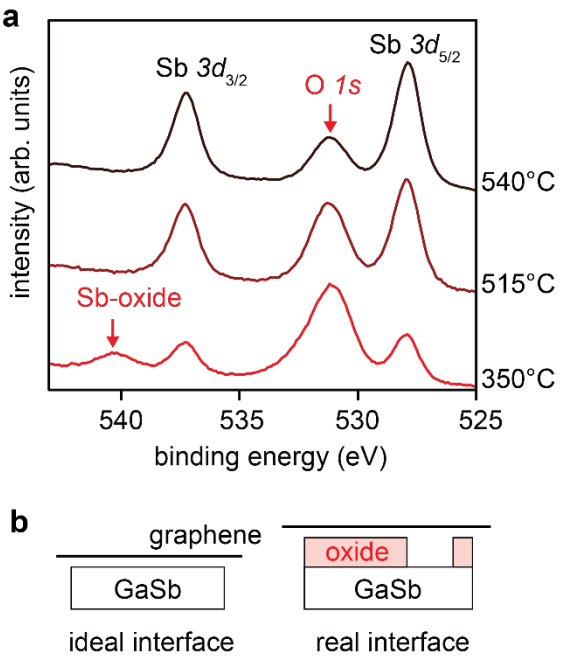

Figure 2.2 – Native oxides desorption from the graphene/GaSb interface. (a) In-situ photoemission spectra of the Sb *3d* and O *1s* core levels, tracking the desorption of native oxides by annealing. (b) Schematics of idealized and real interfaces, after a chemical etch but before thermal oxide desorption.

Fig. 2.2 (b) shows two models of the graphene/GaSb substrate interface, immediately after the graphene layer transfer but before heating the sample to the film growth temperature. For an idealized transfer, the graphene/GaSb interface would be chemically clean and atomically sharp. This is a requirement for the substrate lattice potential to permeate through graphene and template film growth in a remote epitaxy mode [2]. However, such clean interfaces can be difficult to fabricate in practice, especially for III-V semiconductor substrates like GaSb since

III-Vs are typically terminated with an amorphous ~ 3 nm thick native oxide [66]. This oxide must be removed before film growth in order to reveal the underlying crystalline template for an epitaxial film. Although we adopt an HCl etching procedure to remove the substrate native oxides prior to forming the graphene/substrate interface (Methods), some residual oxides may remain.

Our in-situ photoemission spectroscopy measurements reveal that some interfacial oxides remain after the etch procedure. Fig. 2.2 (a) shows in-situ x-ray photoemission spectra (XPS) of the O 1s and Sb 3d core levels for a graphene-terminated GaSb (001) sample, as a function of annealing. These measurements are performed in an interconnected MBE + XPS chamber, such that samples are annealed and measured without removing them from ultrahigh vacuum ($p < 5\times10^{-10}$ Torr). After a 350 °C ultrahigh vacuum anneal to clean surface adsorbates, we observe a significant O *1s* intensity at binding energy of 531 eV. In addition, we observe a satellite to the Sb $3d_{3/2}$ core level at binding energy of 540 eV, indicative of Sb-oxides.

Further annealing of our graphene/GaSb (001) samples removes most of the oxides, despite the presence of the graphene overlayer. After annealing at 515 °C with an Sb_2/Sb_1 flux, no oxide components are detected in the Sb *3d* or Ga *3p* core levels, suggesting that the GaSb-oxides have fully desorbed. We also observe a finite O *1s* core level intensity that decreases as a result of the 515 °C anneal, and

decreases further after the 540 °C anneal. At this point the chemical state of the remaining oxygen above 515 °C is unclear, since no oxide components are detected in the Ga *3p*, Sb *3d*, or C *1s* core levels, suggesting that neither the GaSb substrate nor the graphene itself is oxidized (Supplementary Figure A.3). This suggests that the remaining oxygen at high temperature is weakly coordinated to the graphene or GaSb, yet remains trapped in the near surface region of the sample. Further experiments are needed to understand the oxygen that remains after nominal GaSb-oxide desorption. We observe similar native oxides for graphene/GaAs (001) interfaces even after the HCl etch (Supplementary Figure A.4). Variations on the anneal, including annealing in a H_2/Ar forming gas, also revealed residual oxygen and Sb-oxides after light annealing (Supplementary Figure A.5).

The interfacial oxide desorption creates pinholes in the graphene. Fig. 2.3 tracks the evolution of surface morphology during native oxide desorption. The sample lightly annealed at 350 °C appears qualitatively smooth with no tears or holes observed in the SEM images (Fig. 2.3a). AFM topography reveals a bumpy morphology with height variations of ~ 2 nanometers and hints of the underlying GaSb step and terrace morphology, with terrace length ~ 100 nm (Fig. 2.3b, left). We attribute bumpy morphology to the presence of some interfacial oxides. Raman spectroscopy at this stage shows sharp *G* and *2D* bands with no detectable *D* peak, which is commonly used as a metric to indicate minimal defects in the graphene.

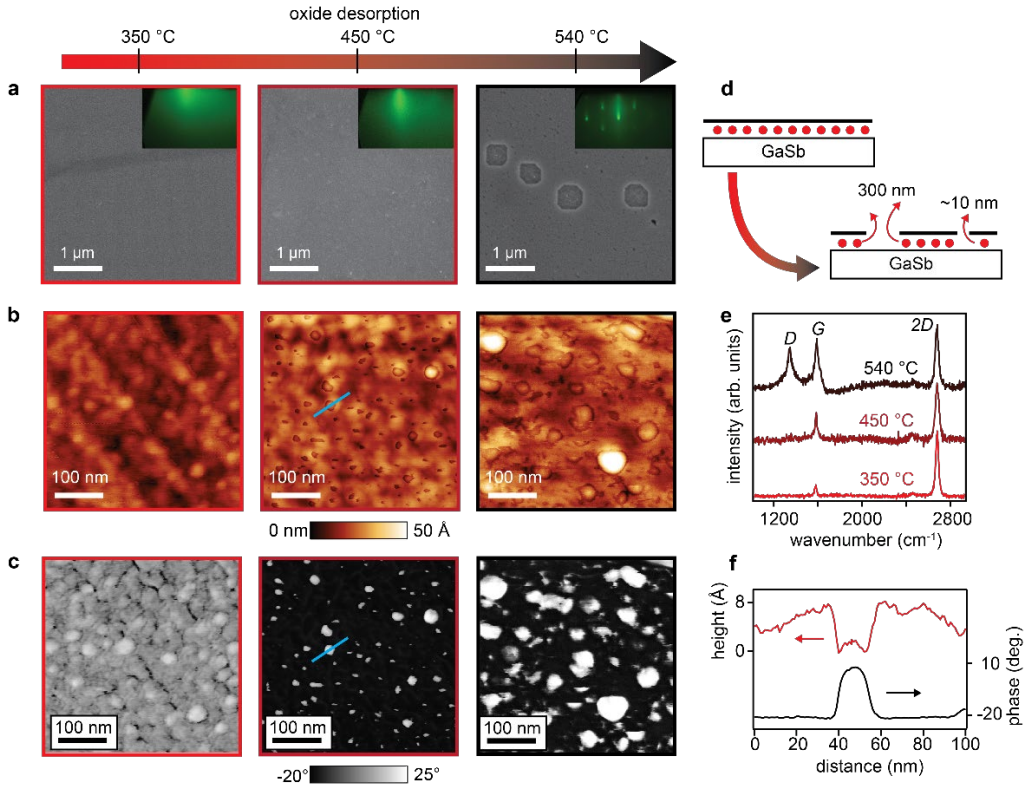

Figure 2.3 – Pinholes created by native oxide desorption. (a) SEM images and RHEED patterns tracking the native oxide desorption and creation of large 300 nm diameter holes. (b) AFM height images. Pinholes with diameter ~ 10 nm appear at the onset of native oxide desorption, 450 °C. (c) AFM phase contrast images. The phase contrast arises from differences in elastic modulus between the graphene and the holes with exposed GaSb. (d) Schematic of the oxide desorption process leading to the creation of holes with different sizes. Red circles represent oxides. (e) AFM height and phase line profiles extracted from the 450 °C sample. The corresponding line cut is marked by the blue line in the AFM images. (f) Raman spectra at various stages during oxide desorption. Strong *D* peak activation coincides with the appearance of large holes after annealing at 540 °C.

These measurements show that before oxide desorption, the transferred graphene has a relatively low defect density.

After annealing at 450 °C, the onset of native oxide desorption, pinholes with diameter ~ 10 nm are observed in the AFM phase and height images (Fig. 2.3b, c and Fig. 2.3e). The distinct contrast in the AFM phase suggests a different elastic modulus in the holes (exposed GaSb) compared to away from the pinholes (graphene). We interpret these holes to be created by the native oxide desorption process, as illustrated in Fig. 2.3 (d). These pinholes are difficult to observe at SEM length scales (Fig. 2.3a) and are not readily detected by Raman spectroscopy since the sample does not have an observable *D* peak (Fig. 2.3f). The RHEED signature of the beginnings of oxide desorption is a sharpening of the specular reflection (Fig. 2.3a, middle insert). An extended analysis of the defects, strain, and doping extracted from Raman is shown in Supplementary Figure A.6.

The pinholes appear to be localized at the bumps that were observed after annealing to 350 °C. However, a more detailed study of samples before and after de-oxidation, at exactly the same location, would provide a more definitive answer to their origin. Oxygen (and oxygen plasmas) are well known to etch graphene [67], particularly at edges and at extended defects like grain boundaries. In the present case, we expect that the larger strains around these protrusions may enhance the oxygen etch rate at these locations, compared to smoother regions of the graphene. Similar enhanced oxygen etching of graphene on other substrates has been attributed to roughness and impurities in the underlying substrate [68].

With further annealing up to 540 °C, the areal density and diameter of the pinholes increases as observed in the AFM images (Fig. 2.3b, c) and in Supplementary Figure A.7. Additionally, we observe larger ~ 300 nm diameter holes in the SEM images. After the 540 °C anneal, a significant *D* band is present in the Raman spectrum, which is indicative of graphene defects. We observe similar pinhole formation for graphene on GaAs (001) (Supplementary Figure A.8).

An important question is whether the presence of oxides and creation of pinholes upon annealing are unique to our wet graphene transfer process, or if the creation of pinholes is more general. Note that we use the same HCl etching procedure that has been used previously for transferred graphene on III-Vs [2]. Additionally, recent XPS measurements show there are oxide satellites in the C *1s* and As *3d* core levels for both wet and dry transferred graphene on GaAs (001) [51]. Therefore, it appears that native oxides trapped at graphene/III-V interfaces are common to both wet (aqueous) and dry (in air) [69] transfer procedures, due to the reactivity of III-V surfaces [70]. Further improvements in interfacial cleanliness may require in-vacuum or glovebox transfer procedures [71].

2.3.3 Seeded lateral epitaxy at pinholes

These pinholes serve as nucleation sites for direct epitaxial growth. Fig. 2.4 tracks the evolution of GaSb film growth on the graphene/GaSb (001) surface after

native oxide desorption. After 0.5 monolayers (ML) of GaSb growth, AFM and SEM measurements show that the GaSb islands selectively nucleate in the ~ 10 nm and 300 nm pinholes rather than on the graphene (Fig. 2.4a, b). We attribute the selective nucleation in the pinholes to the fact that exposed holes to the substrate are more chemically reactive than graphene. At this point we primarily observe nucleation on top of exposed regions of the GaSb substrate, rather than at graphene edges or underneath the graphene. Further experiments are required in order to comment on the possibility of edge initiated epitaxy [72,73] or intercalation under the graphene [74,75], as has been observed in other systems.

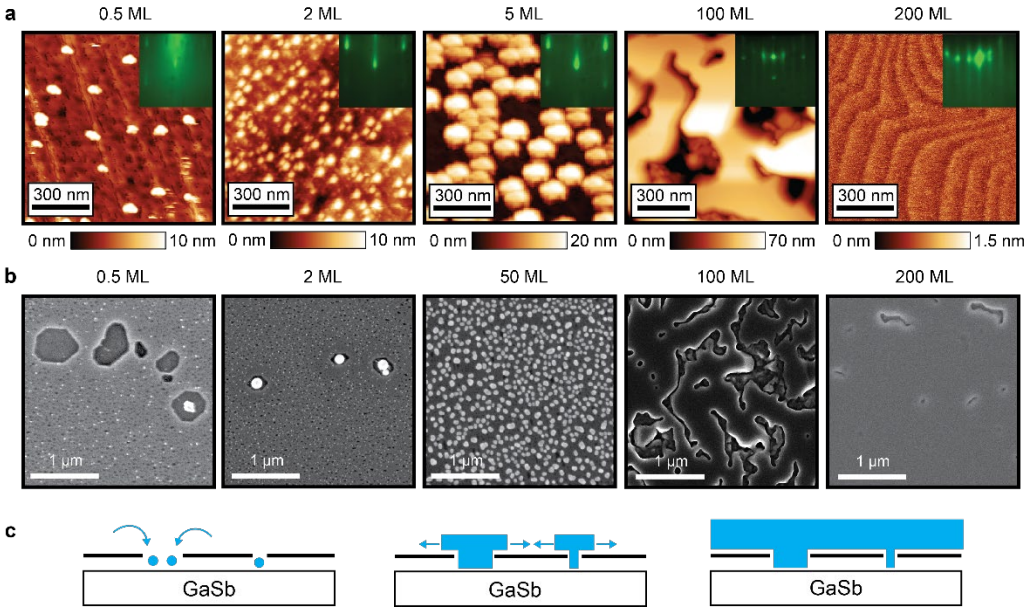

Figure 2.4 – Seeded lateral epitaxy at the graphene pinholes. (a) AFM images tracking the evolution of GaSb nucleation at pinholes in the graphene < 2 monolayers, ML), followed by lateral overgrowth (5 ML) and coalescence into an atomically stepped continuous film (200 ML). One monolayer is defined as half the thickness of a unit cell a/2 = 3 Angstrom, corresponding to an areal density of 5.4×10^{14} atoms/cm^2 each of Ga and Sb. The GaSb growth temperature was 500 °C and the oxide desorption temperatures were 520-540 °C. Inserts show RHEED patterns at each stage of growth. (b) SEM images showing the nucleation at both small and large holes. The islands extend and coalesce around 50-100 ML, and nearly full coalescence is observed after 200 ML film growth. (c) Schematic of lateral epitaxy seeded at holes in the graphene. Blue circles represent GaSb nucleation.

After 2 ML of GaSb growth, nearly all of the holes have nucleated GaSb islands, which we further quantify in Supplemental Fig. A.7. After 5 ML growth, the islands begin to grow laterally (Fig. 2.4a). At 50-100 ML, the islands extend and coalesce (Fig. 2.4b). Finally, after 200 ML a smooth GaSb film surface is

recovered across length scales of several microns, with an atomic step-and-terrace morphology observed by AFM. Our results indicate that the holes created by native oxide desorption serve as sites for the nucleation, lateral epitaxy, and coalescence of GaSb films (Fig. 2.4c).

As a control, we also perform GaSb film grown on a graphene/GaSb (001) sample for which we do not remove the interfacial oxides. For this sample, we anneal to 350 °C, which is below the native oxide desorption temperature. We find that the resulting GaSb film grown at 350 °C is polycrystalline (Supplementary Figure A.9). Therefore, we conclude that removal of the native oxides is a crucial step for growing an epitaxial film.

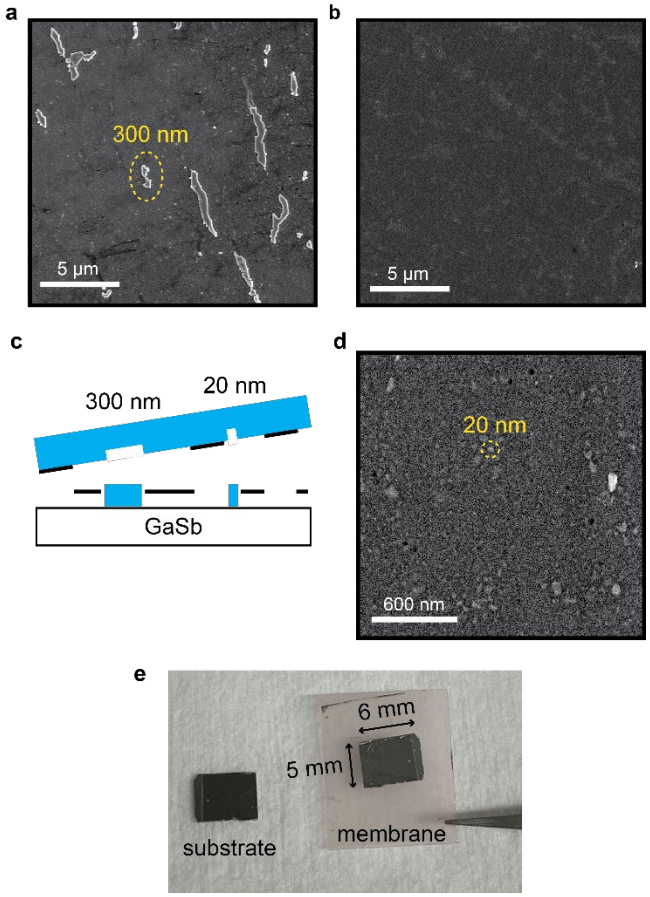

Figure 2.5 – Exfoliation of GaSb membranes that are seeded at pinholes. (a) SEM image of the substrate after exfoliation, showing ~ 300 nm diameter spalling marks and clusters of spalling marks. (b) SEM image of the substrate showing a relatively smooth region with no large spalling marks. (c) Cartoon of the exfoliation. (d) Magnified SEM image of the substrate showing ~ 20 nm spalling marks. (e) Photograph of the substrate and the exfoliated GaSb membrane supported on thermal release tape. The lateral dimensions of the membrane are 5 mm by 6 mm.

Despite the presence of holes, GaSb films grown by a seeded lateral epitaxy mode can be exfoliated, as shown in the large-scale SEM images of Fig. 2.1(e, f). To understand this exfoliation further, in Fig. 2.5 we show higher magnification

SEM images of the substrate after GaSb membrane exfoliation. In Fig. 2.5(a) we observe elongated clusters of spalling marks with width ~ 300 nm and length ranging from 300 nm to several microns, which have approximately the same size and areal density as the 300 nm diameter holes observed in Fig. 2.3(a). We attribute these spalling marks to direct epitaxy in the 300 nm holes, where the film remains stuck to the GaSb substrate rather than being peeled away with the film/membrane. Other regions of the substrate appear relatively smooth at this length scale (Fig. 2.5b), since the original 300 nm holes from oxide desorption are sparsely distributed across the sample. Zooming into this relatively smooth region, we observe smaller scale ~ 20 nm islands (Fig. 2.5d), which we attribute to the film sticking at the ~ 20 nm graphene pinholes. These pinholes are typically evenly distributed across the sample after oxide desorption. After exfoliation we detect Raman *2D* and *G* modes on both the exfoliated membrane side and on the substrate side, indicating that exfoliation tears the graphene (Supplementary Figure A.10).

2.3.4 Comparison with remote epitaxy

Our experiments reveal that pinhole defects drive the seeded lateral epitaxy of GaSb on graphene-terminated GaSb (001). These pinholes are created by native oxide desorption from the substrate. The resulting GaSb films have similar characteristics and structural quality as previous reports of remote epitaxy [1,2,42,44], namely, epitaxial alignment to the underlying substrate,

smooth atomically stepped surfaces, and the ability to exfoliate macroscopically smooth films. We understand the growth in terms of a balance between several atomic scale processes, as illustrated in Fig. 2.6. This balance dictates whether the growth is in a seeded lateral epitaxy regime or a remote epitaxy regime.

Seeded lateral epitaxy occurs in the graphene/GaSb system because (1) graphene is chemically inert and (2) the surface diffusion length λ is long compared to the average spacing L between pinhole defects ($\lambda >> L$). Previous experiments on confinement heteroepitaxy demonstrate that the effective surface diffusion length for group-III metal adatoms on graphene is of order 10 microns, since metal adatoms preferentially nucleate at graphene defects over length scales of order 10 microns [74,75]. Our preliminary experiments on lithographically defined graphene stripes reveal a similar picture (Fig. 2.7). We find that during the early stages of nucleation for GaAs films on patterned graphene/Ge (001), the GaAs preferentially nucleates at exposed regions of the Ge substrate, even when the spacing between graphene openings is 10 microns. This $\lambda \sim 10$ micron effective diffusion length is much larger than the $L \sim 70$ nm spacing between pinhole defects on graphene/GaSb (001). Therefore, adatoms can sample enough of the surface to nucleate at pinhole defects, rather than on the inert graphene. Remote epitaxy would require a larger separation between defects, $L > \lambda$.

The long effective surface diffusion length arises from a combination of long surface diffusion and a high adatom desorption rate (Fig. 2.6a), since the sticking coefficient of Ga and Sb adatoms on inert masks at 500 °C is less than unity. Similar behavior has been observed for selective area epitaxy of III-V films on patterned dielectric masks, such as SiO_2 and SiN_x [52].

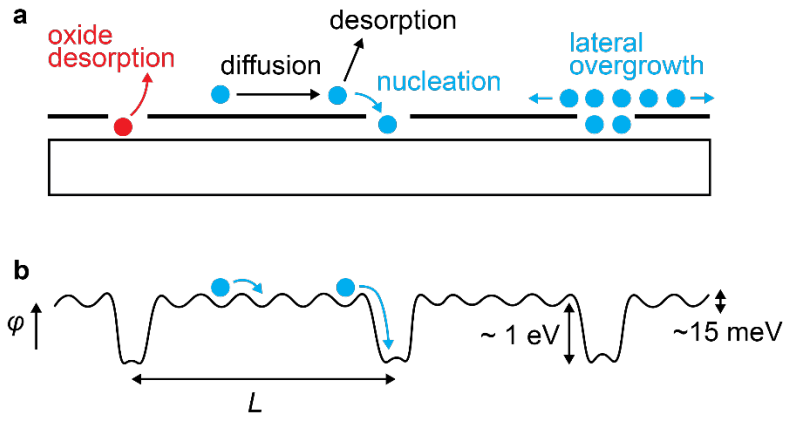

Figure 2.6 – Fast surface diffusion favors seeded lateral epitaxy at pinholes. (a) Pinholes are created by the native oxide desorption, which then serve as nucleation sites for epitaxial growth. (b) Schematic potential φ for adatoms diffusing on the graphene-terminated surface, with diffusion length λ. Seeded lateral epitaxy is expected when L << λ, where L is the spacing between pinholes. Remote epitaxy requires L > λ.

The relative size of potential modulations also explains the preferred nucleation and growth from pinholes (Fig 2.6b). On graphene-terminated regions, the combined potential modulations from the graphene itself and from the substrate that permeate through graphene are expected to be weak. Density functional theory calculations suggest these modulations are of order $\Delta\phi \sim 15$ meV [1], which is

smaller than the thermal energy $k_BT \sim 70$ meV at growth temperature 500 °C. An estimate of the free carrier screening from graphene also suggests this potential should be weak. For a free electron gas with density 10^{19}-10^{20} cm^{-3}, the same density as graphene (graphite) [76], the Thomas-Fermi screening length is approximately $1/k_0 \sim 2$ Å. This is less than the film/substrate layer spacing of ~ 5 Å [2], suggesting that the screened potential above the graphene is exponentially weak. In contrast, the potential modulation at a graphene pinhole is expected to be much larger, $\Delta\phi \sim 1$ eV, since this involves adatoms making chemical bonds to the graphene or to the underlying substrate. The pinholes provide the low energy sites for nucleation and growth. Epitaxial registry is obtained because the pinholes are locations of direct epitaxy to the substrate. Given these factors that favor seeded lateral epitaxy when there is a finite density of graphene defects ($L << \lambda$), our results suggest that previous demonstrations of remote epitaxy can alternatively be explained by a seeded lateral epitaxy mechanism.

Our experiments demonstrate that in the presence of a high concentration of graphene defects ($L << \lambda$), the defects dominate the growth mechanism. Due to the interfacial oxides, we expect that most graphene that is transferred to a foreign substrate will lie in this high defect density regime. Characterization of the graphene quality before the pre-growth anneal (Fig. 2.3 (350 °C) and Supplementary Figure A.8a) is not a reliable representation of the surface quality

immediately prior to III-V film growth (Fig. 2.3 (450 °C) and Supplementary Figure A.8b). Additionally, the ability to exfoliate membranes from graphene is not sufficient to prove a remote epitaxy mechanism, since films grown by seeded lateral epitaxy can also be exfoliated (Fig. 2.5).

On the other hand, our results do not globally rule out the possibility of a "remote epitaxy" mechanism. The key requirement for testing a remote mechanism is to start with clean graphene that has low defect density ($L > \lambda$) immediately prior to film growth, i.e., including the pre-growth annealing. Graphene that is directly grown on the substrate of interest, rather than transferred, provides a cleaner starting point for such studies. III-nitride [74,77] and metal films [75] on epitaxial graphene/SiC, and III-arsenide films on CVD graphene/Ge (Fig. 2.7) are promising options. Our microscopic measurements set a higher experimental bar for proof of remote epitaxy.

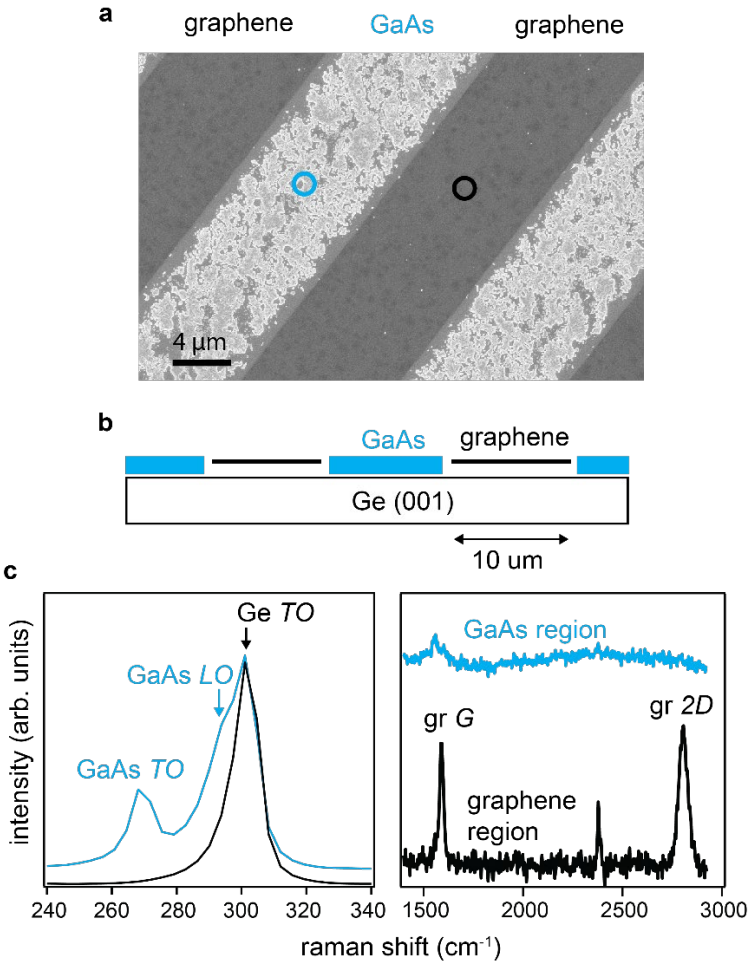

Figure 2.7 – GaAs selectivity on patterned graphene/Ge. The graphene was grown directly on the Ge (001) by CVD, thus avoiding the damage and interfacial oxides typically present for graphene layer transfers. We use photolithography and an oxygen plasma etch to define 10 micron wide stripes of alternating graphene and exposed Ge substrate. GaAs films were then grown on the patterned graphene substrate by MBE. (a) SEM image of GaAs nucleation on patterned graphene on a Ge (001) substrate. We observe selective nucleation of GaAs (light color) on the exposed Ge regions of the substrate, and no GaAs nucleation on the graphene. (b) Cartoon of the sample. (c) Raman spectra on the graphene masked region (black curves) and on the GaAs nucleation region (blue). Representative areas for these spectra are marked by the circles in the SEM image (a).

2.4 Discussion

Our in-situ experiments provide a fundamental understanding of the atomic scale growth mechanisms on graphene, which are crucial for controlling the structure, properties, and scalability of the resultant films and membranes. In addition, seeded lateral epitaxy on graphene offers several advantages over both conventional ELO and remote epitaxy.

Compared to conventional ELO, which uses thick dielectric masks, graphene is the atomically thin limit for a mask material. This thinness is attractive for applications where an electronically transparent interface is desired, e.g. a tunnel barrier [57,58]. Graphene masks also enable the etch-free synthesis and exfoliation of crystalline membranes, for applications in flexible electronics and for inducing novel properties via strain [44].

Compared to remote epitaxy, which is expected to only produce epitaxial films on substrates with polar bonding [1], seeded lateral epitaxy can produce single-crystalline films on nonpolar substrates [53]. Seeded lateral epitaxy is also tolerant to an imperfect graphene/substrate interface. Despite the oxides present at the graphene/substrate interface after graphene transfer, epitaxial growth can still be achieved by desorbing the native oxide to create pinholes. This tolerance is crucial

for translating epitaxy on graphene-terminated surfaces to wafer scale, since it is difficult to perform native oxide-free graphene layer transfers at wafer scale.

Our work suggests that the controlled patterning of nanoscale openings in graphene (Fig. 2.7) provides a route to precisely engineer the size, location, and spatial distribution of nucleation sites, and resulting properties of coalesced films and membranes. Recently, patterned openings in a graphene mask have been used for the selective area epitaxy of 2D hexagonal-BN [59], and point defects in h-BN have been used to seed 2D MoS_2 films with controlled orientations [60]. Our results show that openings in a graphene mask are also promising for the growth of three-dimensional materials like III-V semiconductors, by enabling their exfoliation into free-standing quasi-2D membranes.

2.5 Experimental methods

Graphene synthesis and transfer. Our graphene synthesis and transfer procedure is a modified polymer-assisted wet transfer of CVD-grown graphene [78], similar to the transfer recipe from previous demonstrations of remote epitaxy [1,2]. Graphene was grown by thermal chemical vapor deposition (CVD) of ultra-high purity CH_4 at 1050 °C on Cu foil, as described in Refs. [44,79]. The graphene/Cu foils were then cut and flattened using clean glass slides to match the dimensions of the semiconductor substrate. Approximately 200 nm of 950K C2

PMMA (Chlorobenzene base solvent, 2% by wt., Kayaku Advanced Materials, Inc.) was spin coated on the graphene/Cu foil at 2000 RPM for 2 minutes and left to cure at room temperature for 24 hours. Graphene on the backside of the Cu foil was removed via reactive ion etching using 90 W O_2 plasma at a pressure of 100 mTorr for 30 s. The Cu foil was then etched by placing the PMMA/graphene/Cu foil stack on the surface of an etch solution containing 1-part ammonium persulfate (APS-100, Transene) and 3-parts H_2O. After 16 hours of etching at room temperature, the floating PMMA/graphene membrane was scooped up with a clean glass slide and sequentially transferred onto five 5-minute water baths to rinse any etch residuals.

GaSb (001) substrates were etched in 38% HCl solution for 5 minutes followed by a 2-propanol rinse to remove some of the native oxides. We then used the etched GaSb substrate to scoop the PMMA/graphene stack from the final water bath. To remove water at the graphene/substrate interface, the samples were baked in air at 50 °C for 15 minutes, then at 150 °C for another 15 minutes. The PMMA was dissolved by submerging the sample in an acetone bath at 80 °C for 3 hours. This is followed by an IPA rinse and nitrogen drying. The sample is indium bonded onto a molybdenum puck and outgassed at 150 °C for 2 hours in a loadlock at a pressure $p < 5 \times 10^{-7}$ Torr before introduction to the MBE growth chamber. Finally,

the sample is annealed at ~ 350 °C for 1 hour in the MBE chamber to desorb organic residuals.

MBE growth of GaSb. GaSb films were grown in a custom molecular beam epitaxy chamber (Mantis Deposition) using an effusion cell for Ga and a thermal cracker cell for Sb (MBE Komponenten). Temperatures were measured using a pyrometer that is calibrated to the native oxide desorption temperature of GaAs. *In-situ* reflection high energy electron diffraction (RHEED) measurements were performed using a Staib RHEED gun at 15 keV.

In-situ XPS. X-ray photoemission spectroscopy (XPS) measurements were performed in an XPS chamber that is connected to the MBE via an ultrahigh vacuum ($p < 5 \times 10^{-10}$ Torr) transfer chamber, such that samples are transferred in vacuum and are not exposed to air. We use a non-monochromated Al K_α x-ray source (1486.6 eV) and an Omicron EA125 hemispherical analyzer with an energy resolution of 1.08 eV. Samples were annealed in the MBE and measured in the XPS at room temperature.

AFM, SEM, and Raman spectroscopy. Field emission scanning electron microscopy (SEM) was performed using a Zeiss GeminiSEM 450. Raman spectroscopy was performed using a 532 nm wavelength laser (Thermo Scientific DXR Raman Microscope). The laser power is kept below 5 mW in order to prevent

damage to the graphene. In order to acquire representative Raman spectra, 2600 spectra were captured and averaged over a 2500 μm^2 area. Atomic force microscopy (AFM) measurements were performed using a Bruker Dimension Icon in tapping mode.

X-ray diffraction. X-ray diffraction measurements were performed using a four-circle Malvern Panalytical Empyrean diffractometer, using Cu K_α radiation. Symmetric ω-2θ measurements (ω is the sample tilt in the scattering plane and 2θ is the Bragg angle) and azimuthal pole figure (φ) scans were performed using a 4-bounce Ge 220 monochromator on the incident radiation. Rocking curve measurements were performed using an additional 3-bounce Ge 220 analyzer crystal.

GaSb exfoliation. To exfoliate the GaSb epilayer, a 100 nm Ni stressor layer was deposited on the GaSb / graphene / GaSb (001) heterostructure at room temperature using a metal evaporator (Angstrom Engineering Inc.) in high-vacuum ($p < 2 \times 10^{-6}$ Torr). The film was then exfoliated with two methods. Crystalbond 509 adhesive, with a flow point of 120 °C, was gently smeared on glass slide on a hot plate at 150°C. The sample is then placed film-side down on the adhesive and allowed to cool. The membrane can be easily exfoliated by gently dropping the glass slide from a height of approximately one foot onto a clean surface. The force from the drop is enough to release the substrate from the membrane, leaving the

membrane adhered on the glass slide. Thermal release tape (Revalpha 3195H, Semiconductor Equipment Corp.) was also used to exfoliate by stamping onto the sample, and then carefully peeling the tape away from the substrate.

Photoluminescence measurements. Steady-state photoluminescence (PL) measurements were performed at 300 K with a CW Ar-ion pump laser at a wavelength of 514.5 nm, using a 1500 nm (600 gr/mm) grating and a liquid-nitrogen cooled Ge detector. The power density was approximately 6.96 watts/cm^2.

3 Nucleation and growth on clean graphene interfaces

The last two sections of this chapter are adapted from the following articles, while the first section is based on ongoing work I have performed:

- D. Du, T. Jung, **S. Manzo**, Z. LaDuca, X. Zheng, K. Su, V. Saraswat, J. McChesney, M. S. Arnold, and J. K. Kawasaki, *Controlling the Balance between Remote, Pinhole, and van Der Waals Epitaxy of Heusler Films on Graphene/Sapphire*, Nano Lett. **22**, 8647 (2022).

  Author contribution: I performed graphene transfers to sapphire and assisted in the characterization of the graphene (Raman, AFM).

- Z. LaDuca, K. Su, **S. Manzo**, M. S. Arnold, and J. K. Kawasaki, *Control of Ternary Alloy Composition during Remote Epitaxy on Graphene*, Phys Rev Materials. **7**, 083401 (2023).

  Author contribution: I performed some of the graphene transfers to MgO and assisted in the morphological characterization (SEM).

3.1 Nucleation of GaAs on epitaxial graphene on germanium

We have shown that transferred graphene on semiconductor substrates leads to defect formation due to thermal desorption of the native oxide [80]. Moreover, metallic and organic contaminants associated with dry and wet graphene transfers are difficult to avoid [81,82]. The impact is that on these surfaces, extrinsic growth mechanisms such as pinhole seeded epitaxy dominate, rather than "remote" epitaxy which requires clean starting graphene. Most studies of "remote" epitaxy cannot clearly distinguish between these two scenarios [1,35,45,83]. We understand the relative importance of these two mechanisms by comparing their characteristic length scales. In a dirty or defective interface, the surface diffusion length of adatoms (λ) on graphene will be much larger than the distance between defects/contaminants (L), which are chemically reactive nucleation sites. Only if $\lambda < L$, can we study the effect of remote interactions. Therefore, directly grown graphene on a substrate in which L is very large, would be a more suitable platform to investigate remote epitaxy. Here, we deposit GaAs on epitaxial graphene directly grown on Ge (111) substrates to elucidate where nucleation occurs on a clean system. Our hypothesis is that the step edges in gr / Ge (111) provide a much larger potential fluctuation, and that these step edges may provide sites with sufficiently large transmitted lattice potential fluctuation to seed epitaxy to the substrate.

Figure 3.1 compares the starting graphene quality of epitaxial gr/Ge (111) and transferred gr/GaSb after thermal desorption of the native oxide at 540 °C [80]. We see a dramatic difference in the defect density between the two samples. In the case of gr/Ge (111), our atomic force microscopy measurements do no detect any pinholes down to a minimum diameter of 5 nm (Fig. 3.1 a, b). Conversely, for annealed gr/GaSb we observe a pinhole density of ~ 400 μm^{-2}. Raman spectroscopy tells us the graphene on Ge (111) is highly ordered, with a negligible defect-activated D-mode and narrow 2D and G peaks [84–87]. In contrast, the Raman spectrum of the transferred Graphene on GaSb after oxide desorption has a high D:G intensity ratio, indicative of a high defect density [86,87] (Fig. 3.1d). Clearly, the terraced gr/Ge (111) surface is the better choice to study remote epitaxy. This system gives us a much better chance to meet the important $\lambda < L$ requirement mentioned earlier. It is important to note that the pinhole defects we are referring to are those that can be resolved by AFM (5 nm diameter and above). As a result, we cannot rule out the presence of smaller point defects such as vacancies and Stone-Wales defects in the graphene lattice [49,50,88].

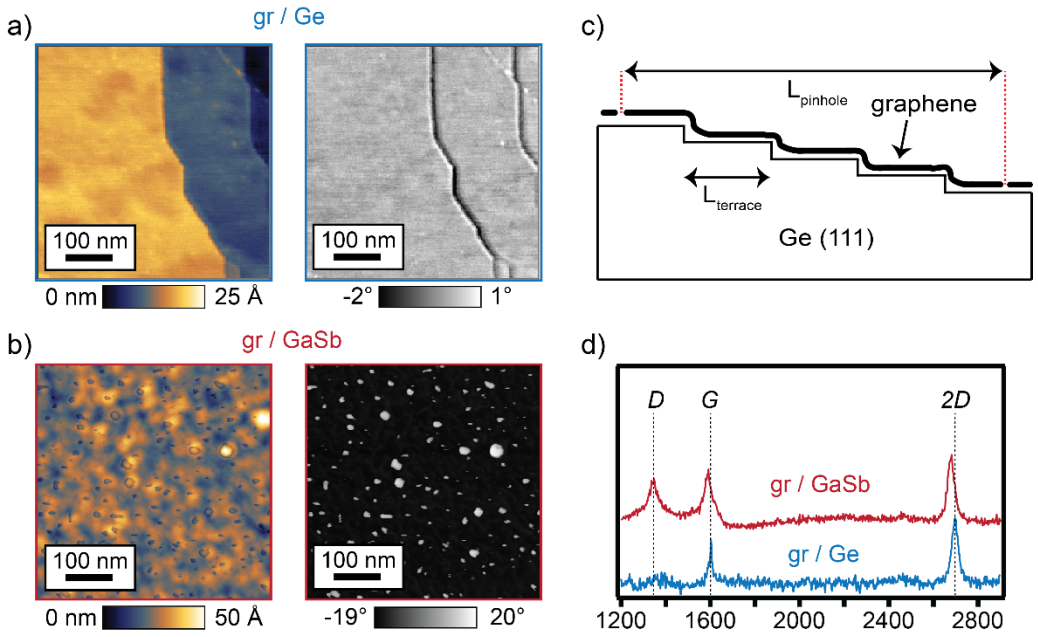

Figure 3.1 –Comparison of a clean gr/Ge (111) interface vs a defective gr/GaSb (001) interface. (a) AFM height and phase image of gr/Ge (111). (b) AFM height and phase image of transferred gr/GaSb after deoxidation. (c) Cartoon illustrating the clean, terraced gr/Ge (111) surface. The distance between pinholes $L_{pinhole}$ is smaller than the terrace spacing $L_{terrace}$. (d) Representative Raman spectrum of gr/Ge (111) and gr/GaSb after annealing up to 540 °C to remove the native oxides.

Our characterization of gr/Ge (111) prior to growth suggests we have a starting surface where the average terrace length is smaller ($L_{terrace}$ ~ 0.5 - 1 μm) than the distance between defects ($L_{pinhole}$) (Fig. 3.1c). Moreover, the adatom surface diffusion length of metals on graphene is likely larger than $L_{pinhole}$ at GaAs growth temperatures (~ 600 °C) and on the order of 10s of microns [89–91]. Therefore, an adatom will encounter a step edge before it encounters a pinhole, which means step-flow-like growth on the draped graphene could be possible.

We grew GaAs on gr/Ge (111) at 580 °C, which is a high enough temperature to avoid any polycrystalline or stochastic nucleation on the graphene. Reflection-high energy diffraction (RHEED) patterns of samples grown at this temperature appear streaky and are indicative of a surface with long-range ordering (Fig. 3.2a, inset). Further details on the growth of GaAs on gr/Ge (111) at different temperatures can be found in Appendix B. The deposition time was 46 minutes, resulting in an integrated flux of 8.9×10^{16} atoms/cm^2 which corresponds to a nominal thickness of 40 nm for a unity sticking coefficient of Ga. The growth rate was 52 nm/h and estimated using homoepitaxial GaAs RHEED oscillations. The As/Ga flux ratio (~ 21) was approximated by reaching the lower bound of the GaAs growth window with a fixed growth temperature while observing RHEED oscillations.

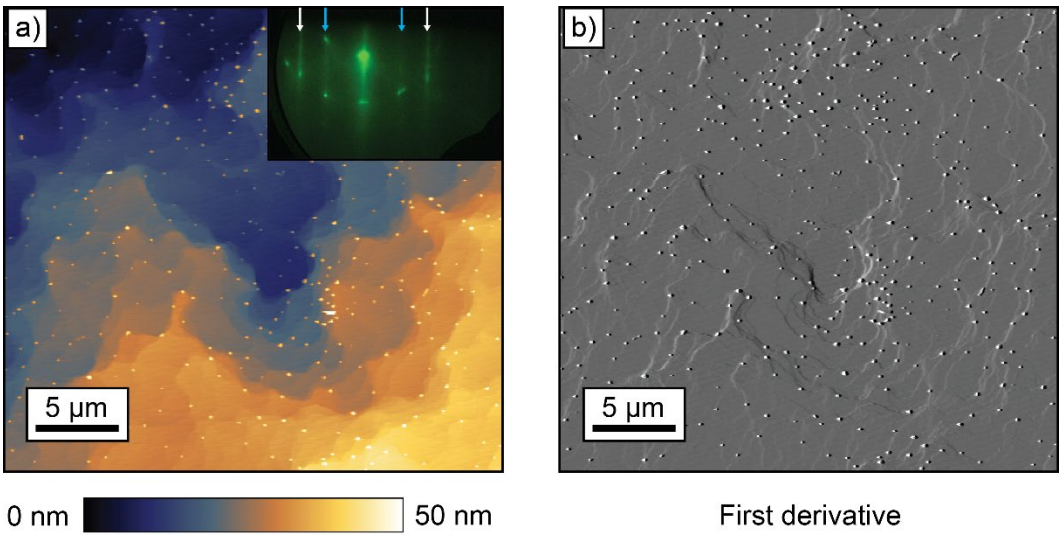

Figure 3.2 – Nucleation of GaAs islands at gr / Ge step edges. (a) AFM height image of GaAs / gr / Ge (111) (inset: RHEED pattern of the sample along a <11$\bar{2}$> azimuth. White arrows denote the first-order reflections of graphene, blue arrows denote the first order reflections of GaAs). (b) First derivative of (a), emphasizing step-edge nucleation.

Figure 3.2 (a, b) shows an *ex-situ* AFM height image of a sample grown at 580 °C and its first derivative, which emphasizes where GaAs islands are nucleating. Both images clearly show that tall, circular islands are nucleating at the top surface of step edges. The islands are taller than the nominal thickness of 40 nm (60-80 nm step heights), indicating that adatoms are diffusing and clustering together at these nucleation sites. Raman scans of these tall circular islands exhibit the *LO* and *TO* modes of GaAs (Fig. 3.3 (f), green curve). The top of step-edges is not a typical nucleation site during conventional epitaxy. If one considers the Terrace-step-kink (TSK) model, the top surface of a terrace would not be the most

energetically favorable nucleation site, since it provides fewer nearest neighbors than the bottom of step edges [92]. This simple picture does not take the graphene into account, however. It seems reasonable to assume that the graphene drapes over the terraced Ge surface conformally; however, the structure of graphene at Ge step edges has not been extensively studied. In the gr/SiC system, step edges have been demonstrated to have a negative effect on graphene's electronic transport properties, being scattering sites for charged carriers [93,94]. High defect densities have been observed at the step edge regions, which show inferior mobilities compared to the flat terrace regions [94,95]. If the graphene is also defective at the Ge step edges, then this could explain the nucleation of islands that we observe in our samples. Another possibility is the graphene strain field around the step edges could be enhancing the reactivity of these regions and lead to nucleation [96,97]. Atomic-resolution, cross-sectional and plan-view imaging of the graphene at Ge step terraces is needed to further understand this morphology. This result seems to align with our hypothesis of nucleation at terrace steps on clean graphene systems. This morphology could represent a growth mechanism on graphene that is not dictated by pinholes. In other words, nucleation on clean graphene seems to begin at step edges.

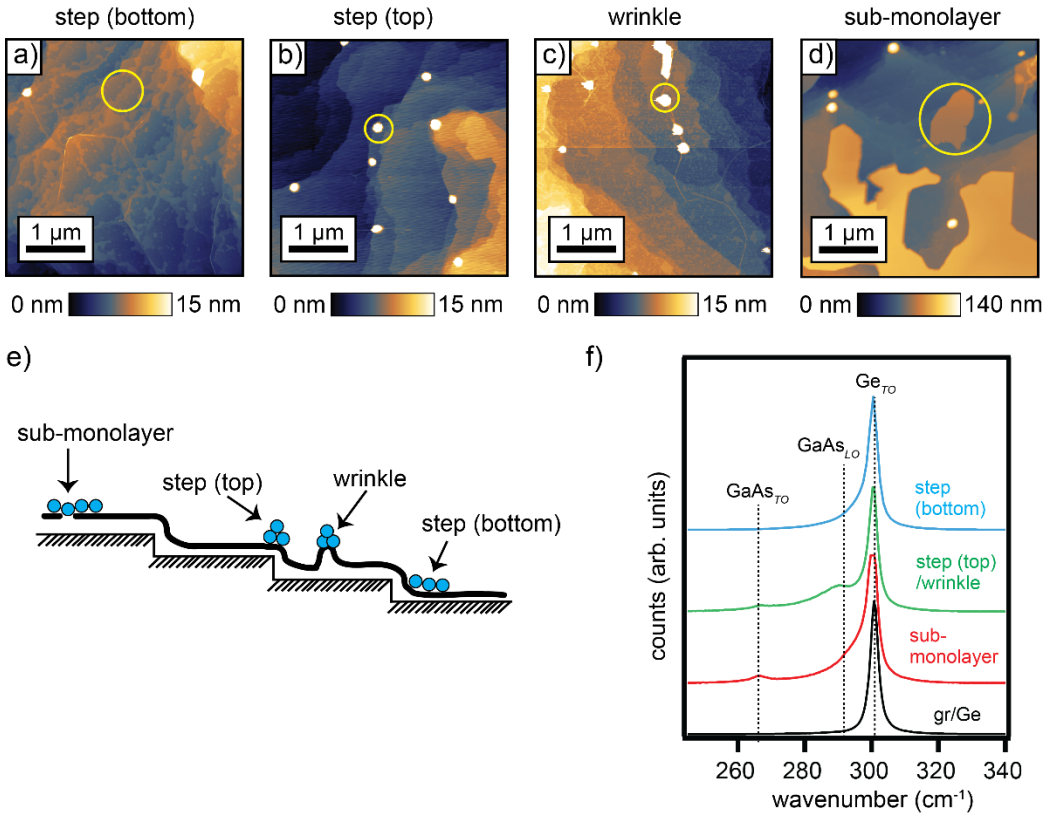

Figure 3.3 – Different forms of nucleation of GaAs on gr/Ge (111). (a) AFM of sample showing smooth, GaAs islands that nucleate at the bottom of step-edges. (b) AFM showing tall, spherical islands nucleating at the top of step-edges. (c) AFM of islands nucleating at graphene wrinkles (d) AFM image of smooth plate morphology of GaAs on sub-monolayer gr/Ge (111). (e) Cartoon of the four GaAs nucleation phenomena observed on gr/Ge (111). (f) Representative Raman spectra of the different types of GaAs nucleation.

In addition to nucleation at the top of step edges, we also observe nucleation at the bottom of step edges, at wrinkles, and in some cases at unintentional graphene-openings (Fig. 3.3e). The AFM images in Figure 3.3 (a-d) correspond to

four different samples. The growth conditions for these samples are the same (T_{growth} = 580 C°, V_{As}:III_{Ga} ~ 21, nominal th = 40-60 nm, growth rate = 52 nm/h); however, the gr/Ge "batch" is different, meaning that the gr/Ge substrates were not grown at the same time.

Figure 3.3 (a) shows GaAs nucleation at the bottom of step edges. AFM linecuts reveal that the islands that emerge from step-edges are flat and approximately ~1 nm thick. (Supplementary figure B.3). AFM phase contrast strongly tracks with the flat GaAs islands, which have a markedly different phase than the gr/Ge substrate (Supplementary figure B.3). This morphology seems to suggest a step-flow-like growth that would be more consistent with the TSK model. This is difficult to prove without doing *in-situ* surface-sensitive measurements such as scanning tunneling microscopy (STM) or photoemission electron microscopy (PEEM) at the early stages of nucleation. *Ex-situ* Raman spectroscopy of these features show that the Ge *TO* mode, located at ~ 300 cm^{-1}, is asymmetric and broader when compared to gr/Ge prior to growth (Fig. 3.3e, blue curve). This suggests that there is GaAs in this region, since the GaAs *LO* mode is located at around ~290 cm^{-1}. The islands are ultrathin (~1 nm) so the intensity of the GaAs modes would be very weak, which is probably why the GaAs *TO* is missing from the spectra. The discovery of a step-flow-like growth mode on gr/Ge would throw a wrench into the accepted understanding of "remote epitaxy" since Ge is a non-

polar substrate. It is currently believed that the substrate below graphene has to be polar for remote epitaxy to occur, since the polarity of the substrate governs the potential fluctuations that penetrate the graphene and template the overlayer [1]. Our results suggest that epitaxy on graphene might not require a polar substrate if sites with enhanced lattice potential fluctuation, like step-edges, are available on the surface. Through step edge engineering, we can provide a high density of nucleation sites that could transmit the substrate lattice potential. Although further investigation is required, the proposed step-flow-like mechanism seems like the most reasonable explanation for the observed morphology.

Wrinkles are defective regions in the graphene lattice, and are therefore more chemically reactive than flat, pristine graphene [98]. We suspect this reactivity is responsible for the observed selective nucleation of spherical islands at the wrinkles (Figure 3.3c, yellow circle). The low wettability of the surrounding low surface energy graphene explains why these islands “bead” up and adopt a spherical morphology, although this could also be due to oxidation. Since these islands are roughly the same diameter as the ones that nucleate on the top of step-edges, it is impossible to differentiate them in the optical microscope of the Raman system. As a result, scans were taken of 6 different spherical islands, which showed virtually identical spectra. Therefore, the spectrum shown in Fig. 3.3 (f, green curve) is representative of both the wrinkle and step-edge islands. The presence of

wrinkles and grain boundaries mean that our idealized picture of gr / Ge (111) in Fig. 3.1 (b) is not entirely accurate. These reactive sites will compete with the step-edges for nucleation.

Finally, on some samples we observe smooth plate morphology that is not fully coalesced (Fig. 3.3d, circled yellow). Based on comparison with samples that are known to have sub monolayer coverage, it is likely that this growth is direct epitaxy at pinholes. Raman spectroscopy of the "plates" confirms that they are GaAs, as evidenced by the presence of the GaAs *TO* and *LO* phonon modes (Figure 3.3 (f), red curve). The *LO* mode is very close to the Ge substrate's *TO* mode, which is why the Ge *TO* mode is asymmetric. Furthermore, X-ray diffraction and RHEED confirm this sample is single-crystalline and aligned with the underlying substrate (Supplemental Fig. B.2). The most compelling evidence of sub-monolayer coverage prior to growth is the fact that we could not exfoliate the GaAs plates with tape or with strongly bonded wax (Crystalbond). SEM images after exfoliation show that the plate morphology is largely unchanged, indicating that they are likely clamped by direct epitaxy with the substrate (Supplementary Fig. B.2).

In conclusion, we have studied the nucleation dynamics of GaAs on gr/Ge (111) and have found some preliminary evidence for a step-flow like growth mechanism at the graphene-draped terrace steps. Yet, the gr/Ge (111) system is not perfect and the $\lambda < L_{pinhole}$ condition might not be met in this system if the graphene

growth conditions are not optimized. In such a scenario, pinhole-seeded epitaxy will occur just like in the transferred gr/GaSb case. Moreover, we have shown that wrinkles, which are present in virtually all graphene-terminated surfaces, will also act as nucleation sites that are completely unrelated to a remote mechanism. Therefore, the wrinkle density is another factor that needs to be considered and minimized. Growing graphene on substrates with a low thermal expansion mismatch such as twin-boundary-free single-crystal Cu (111) films on sapphire is a promising approach to achieve ultra-flat graphene [99]. Our results also show that graphene wrinkles, graphene grain boundaries, and unintentional openings can also serve as nucleation sites, that are generally distinguishable in AFM from the step edge nucleation. Further optimization in the starting graphene quality will help our understanding of a possible "remote" mechanism.

3.2 Controlling the balance between remote, pinhole and van der Waals epitaxy

The exfoliation of films grown on graphene, which are in epitaxial registry with the underlying substrate, has been used as proof that "remote interactions" dictate the growth [1,51,83]. However, we have demonstrated that pinhole-seeded lateral epitaxy can produce single-crystalline, exfoliatable films on graphene-terminated surfaces [80], thereby replicating all of the features of remote epitaxy via an alternate mechanism. Van der Waals epitaxy (vdWE) can also produce similar results, such as the growth and exfoliation of single-crystalline GaN films on graphene/SiC (0001) [100] and GaN on h-BN/Al_2O_3 (0001) [101]. This has led to terms like "quasi-vdWE" and "remote epitaxy" being used interchangeably, yet the mechanism is fundamentally different, since in vdWE the film is templated by the 2-dimensional material and not by the substrate. As a result, more conclusive experimental evidence is required to determine whether remote interactions play a role when growing films on graphene-terminated substrates.

Here we show how the growth temperature, graphene annealing conditions, and relative film/substrate versus film/graphene lattice mismatch can tune the competing mechanisms of remote epitaxy, pinhole epitaxy, and van der Waals epitaxy, across a series of cubic and hexagonal Heusler compounds with varying

lattice parameter: GdPtSb (cubic $F\bar{4}3m$), LaPtSb (hexagonal $P6_3mc$), and GdAuGe (hexagonal $P6_3mc$). We find that GdPtSb grown on graphene/c-Al2O3 exhibits a 30° rotated ($R30$) epitaxial superstructure that cannot be the result of pinhole-seeded lateral epitaxy or vdwE. By process of elimination, this result is suggestive of remote epitaxy.

The films were grown via molecular beam epitaxy (MBE) on wet-transferred graphene on pre-annealed sapphire substrates (see Ref. [102] for further details on the graphene transfer and MBE growth). We find it is critical to anneal the graphene prior to growing our films. If the graphene is not annealed up to 700 °C, interfacial contaminants will remain trapped at the graphene-substrate interface. This causes films to be fiber-textured, with random in-plane orientations and primarily $[111]_c$ – oriented out of plane, which is an indication of vdwE. After annealing at 700 °C, the growth surface is clean and the underlying atomic step terraces of sapphire, draped by graphene, can be seen in AFM images. Importantly, Raman spectroscopy as well as the morphological characterization suggest that the graphene pinhole density is ~ 10/μm^2. This is a factor of 20 lower than the pinhole density for graphene/GaSb after native oxide desorption [80].

Heusler films grown on graphene/ c-Al2O3 are epitaxial and exfoliatable, with a single-orientation out of plane ([111]c and [0001]h). We use the same

mechanical exfoliation technique as in Ref. [44]. X-ray diffraction azimuthal φ scans reveal that the in-plane orientation is dependent on the lattice constants of

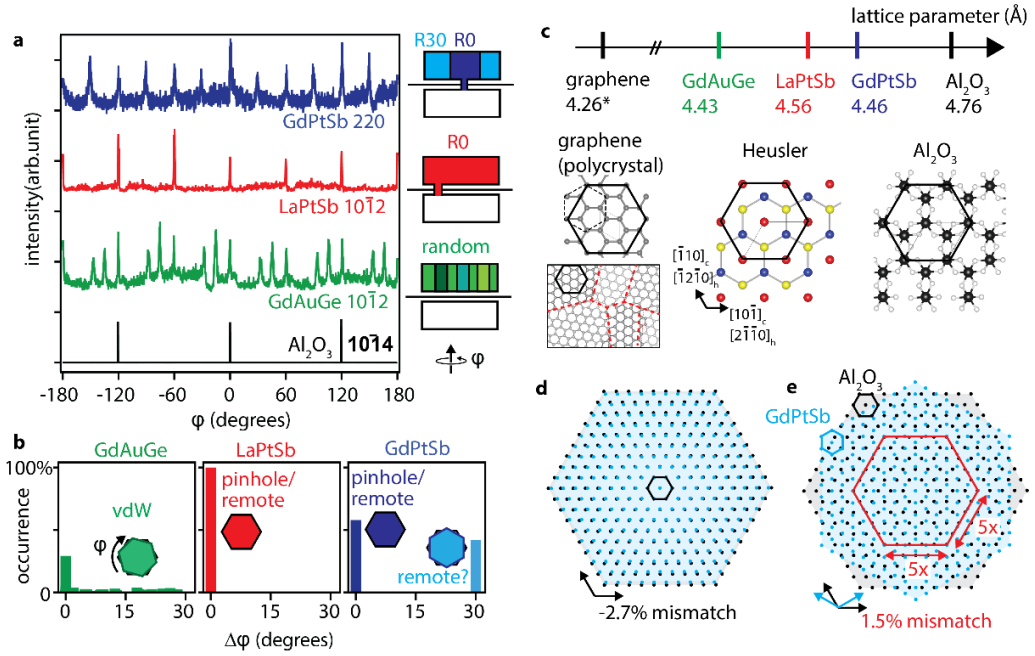

Figure 3.4 – In-plane orientations (Figure and caption adapted from Ref. [102]). (a) ϕ scans of the GdPtSb 220, LaPtSb 101$\bar{2}$, and GdAuGe 101$\bar{2}$ film reflections, referenced to the sapphire 101$\bar{4}$. (b) Distribution of in-plane orientations. Each distribution represents statistics on at least 20 samples. (c) In-plane hexagonal lattice parameters and crystal structures. For cubic GdPtSb, the hexagonal lattice parameter a_h is defined as $a_h = \frac{1}{2}d_{110}$. For graphene, the lattice parameter of 4.26 Å corresponds to a $(\sqrt{3} \times \sqrt{3})$R30° supercell (solid black line), with respect to the conventional unit cell (dotted black line). Note the graphene is polycrystalline, so epitaxy to graphene results in a polycrystalline Heusler film. (d) *R0* hexagon-on-hexagon orientation. The GdPtSb lattice is shown in blue and the sapphire lattice in black. The mismatch is 2.7% tensile. (e) *R30* orientation. The corresponding (5 × 5) supercell (red) with $5\times a_{\text{sapphire}} \approx 3\times (\frac{1}{2}d_{210,\text{ GdPtSb}})$ has a smaller lattice mismatch of 1.5% compressive.

the Heusler films (Figure 3.4a). GdAuGe has the highest lattice mismatch with the sapphire substrate (7.3% tensile) and the smallest mismatch to the graphene lattice (4.0% compressive, rotated 30° with respect to the graphene) (Fig. 3.4c). For this compound we see a distribution of in-plane orientations in the pole figure, which is an indication of vdWE, since the polycrystalline graphene is templating the growth (Figure 3.4a-c, green).

For the hexagonal Heusler LaPtSb on the other hand, which has a moderate mismatch with sapphire (4.2% tensile) and a large mismatch to graphene (7% compressive), we observe six $10\bar{1}2$ reflections in the φ scan which are aligned with the sapphire $10\bar{1}4$ reflections (Figure 3.4a). This is indicative of six-fold symmetry. Additionally, we see no other in-plane orientations across other samples (Figure 3.4b). These results confirm that the LaPtSb film is epitaxial to the sapphire despite the presence of a graphene interlayer. We believe this is due to pinhole-seeded epitaxy or remote epitaxy. Without a surface sensitive experiment during the early stages of nucleation it is difficult to rule out either mechanism.

Interestingly, GdPtSb, which has the lowest mismatch to sapphire (2.7% tensile), exhibits two epitaxial domain orientations: *R0* (aligned to substrate) and *R30* (30° rotated). In the φ-scan, we see that one set of GdPtSb 220 reflections is aligned with the sapphire, while another set of reflections is shifted by 30° (Figure 3.4a). Like for LaPtSb, the *R0* orientation is the expected hexagon-on-hexagon

epitaxial relationship with the substrate (Figure 3.4d), which is suggestive of a remote or pinhole mechanism. The *R30* domain cannot be explained by vdWE, since the graphene is polycrystalline. Pinhole-seeded epitaxy would only result in the *R0* orientation, since this mechanism involves direct epitaxy with the substrate at the defects, followed by lateral coalescence over graphene. Therefore, the *R30* domain could be the fingerprint of a “remote” mechanism.

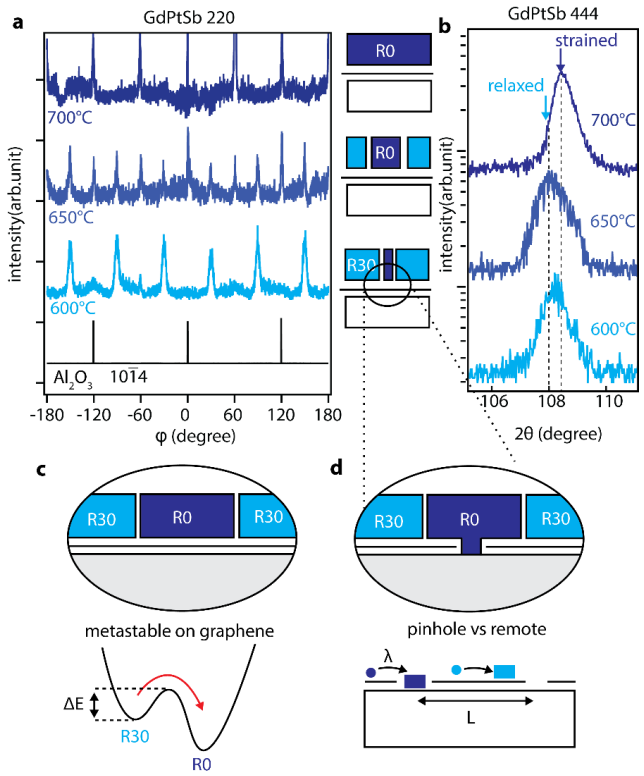

Figure 3.5 – Controlling in-plane rotations (Figure and caption taken from Ref. [102]). (a) Azimuthal ϕ scan of the GdPtSb 220 reflections for three films grown at 600, 650, and 700 °C (blue), on graphene/sapphire that had been annealed to 700 °C. All curves are referenced to the 101$\bar{4}$ reflections of the sapphire substrate (black). (b) Out-of-plane 444 reflection tracking changes in lattice parameter. (c, d) Possible mechanisms to explain the temperature dependence. (c) Metastability of the 30° domain on graphene. In this picture, both *R0* and *R30* domains appear for growth on graphene. Increasing the growth temperature enables the system to surmount a kinetic barrier between the two domains. (d) Pinhole versus remote mechanism. Higher growth temperatures favor growth at pinholes, because of the increased surface diffusion length λ. Growth from pinholes results in the *R0* domain.

To elucidate the origins of the *R30* domain, we investigate the dependence of the growth temperature on the *R30:R0* ratio. We find that higher growth temperatures favor the *R*0, while lower growth temperatures favor the *R30* domain.

We are able to grow singly oriented *R0* films at 700 °C and almost purely *R30* films at 600 °C, while intermediate growth temperatures result in a mix of both (Figure 3.5a). High-resolution 2θ-ω scans of the out-of-plane 444 reflection indicate that the high growth-temperature *R0* films are strained, which is suggestive of direct epitaxy at pinholes. The sample grown at lower temperatures is relaxed, indicating nucleation on clean graphene. We speculate that this temperature dependence can be understood in terms of adatom diffusion lengths on graphene. At high growth temperatures, the diffusion length for Gd, Pt and Sb is larger than the distance graphene pinholes ($\lambda > L$). As a result, an adatom that lands on graphene will diffuse across the surface until it finds and nucleates at the reactive defect site (Figure 3.5d). At low temperatures, the diffusion length is not large enough for an adatom to find the pinhole, so it will randomly nucleate on the bare graphene, leading to the *R30* domain. An alternate explanation could be that both low and high temperature growths are a result of remote epitaxy. The *R30* domain could be a metastable phase, while high temperature can overcome a kinetic energy barrier that results in the stable *R0* domain. More experiments and theory are needed to elucidate the energetics and kinetics of the domain formation on graphene.

We have established that the *R30* domain cannot arise from vdWE or pinhole-seeded epitaxy; next, we address other possible explanations. Intercalation of metals [75] and binary metal oxides [103] and nitrides [74] under graphene has

been experimentally realized, but we rule this mechanism out since we do not see any spallation marks after exfoliating our films on the bare substrate. Another possible explanation is the formation of an epitaxial rare-earth carbide. Gadolinium carbides (Gd_2C_3 and GdC_2) have been synthesized by annealing Gd films on HOPG at 1000 K, which is close to our Heusler growth temperatures [104]. However, XPS experiments of an ultrathin GdPtSb film (2 monolayers) on graphene/c-Al_2O_3 did not detect any Gd_xC_y (further details on the photoemission data can be found in Ref. [102]), indicating that interfacial carbides are likely not responsible for the *R30* domain. It is too early to completely rule out this possibility, and more surface sensitive experiments are needed to determine if a carbide can form at the Heusler-graphene interface. I will explore this possibility further in chapter 5.

We hypothesize that the *R30* domain is stabilized by graphene due to the relaxed lattice matching requirements associated with the weakly interacting van der Waals surface. No strong covalent bonds should exist between the graphene and the film, so the weakened bonding interactions can allow the film to adopt an orientation that lowers the strain energy via lattice rotation. Previous work has shown that rotational ordering is possible for weakly coupled systems [105–108]. In the case of GdPtSb, the *R*30 domain corresponds to a (5 x 5) superstructure that has a reduced compressive mismatch of 1.5% with sapphire (Fig 3.4e). The relaxed film grown at 600 °C supports this idea. Interestingly, we don't see the *R*30 domain

on the other Heusler films grown on graphene (LaPtSb, GdAuGe). We believe that the formation of these rotated domains is dependent on the unique film/graphene/substrate combinations (i.e., lattice mismatch, surface diffusion length and possible interfacial phase formation). Controlling the rotation angle of these domains could enable the creation of exotic Moiré heterostructures, which have been shown to exhibit remarkable electronic properties [17,109].

We have discovered a 30° degree-rotated domain in GdPtSb films grown on clean graphene/sapphire that cannot be explained by van der Waals epitaxy or pinhole-seeded epitaxy. At this time, the most logical explanation for the *R30* domain is remote epitaxy. The *R0* domain, which is aligned to sapphire, is favored at high growth temperatures, while the *R30* domain is favored at low temperatures. We speculate this is due to an increase in the surface diffusion length at high temperatures, which is larger than the average distance between defects, thus resulting in pinhole epitaxy. Due to the weak van der Waals interactions between film and graphene, we believe that a rotated domain is allowed to form which decreases the strain energy of the system. We are hesitant to rule out other mechanisms such as interfacial carbide formation without further surface sensitive spectroscopy and microscopy experiments. Our work represents an important step in realizing an experimental demonstration of remote epitaxy.

3.3 Low sticking coefficients on graphene – an important consideration when controlling film composition

Most demonstrations of epitaxy on graphene have focused on compound semiconductors such as III-Vs [1,83,110] and II-VIs [111–113], which are characterized by self-limited stoichiometries within an adsorption-controlled growth window. As a result, precise control over elemental flux ratios during the growth of these compounds is not as critical. However, this is not the case for more complex materials such as ternary transition metal oxides or Heusler alloys, which only demonstrate adsorption-controlled growth windows in specific cases. Both of these materials systems exhibit remarkable magnetic, electronic and topological properties [36–40,114–116], so the production of crystalline membranes of these materials enabled by epitaxy on graphene area of research ripe with potential. Unfortunately, the effect of non-unity sticking coefficients on graphene-terminated substrates has not been extensively studied. In order to grow stoichiometric Heusler or complex oxide films via remote, pinhole or van der Waals epitaxy, a thorough understanding of nucleation and desorption on graphene is required. Here we grow Ni_2MnGa films on graphene / MgO (001) and perform energy dispersive x-ray spectroscopy (EDX) and ion backscattering spectrometry (IBS) to quantify the element-dependent sticking on graphene-terminated surfaces.

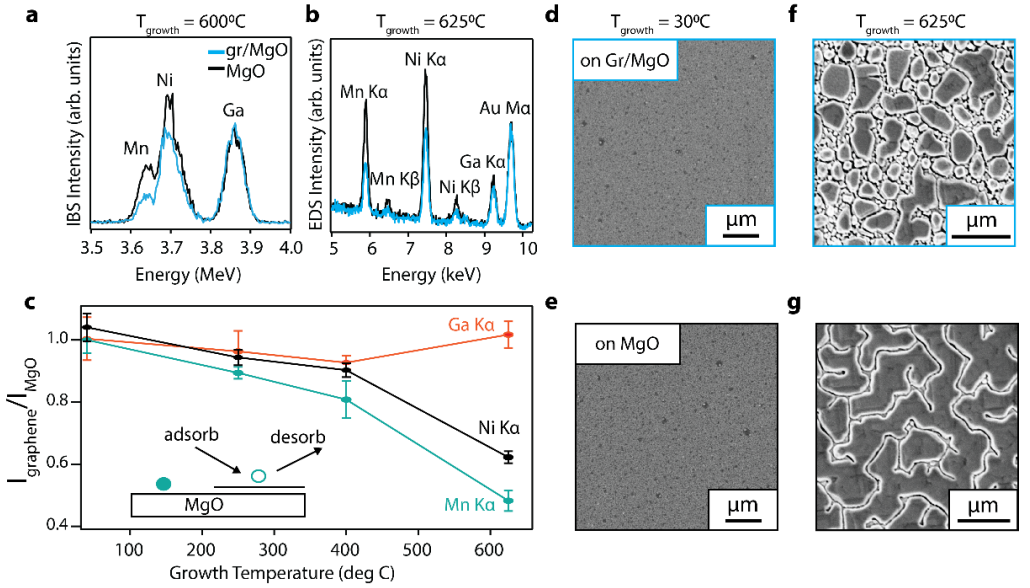

Figure 3.6 – Element and temperature specific sticking on the graphene surface (Figure and caption taken from Ref. [117]). (a) Ion beam scattering (IBS) of nominally 20 nm thick Ni_2MnGa films grown on graphene/MgO and MgO at 600 °C, showing reduced sticking for Ni and Mn on graphene. (b) Energy dispersive X-ray spectroscopy (EDS) measurements for Ni2MnGa films with nominal thickness 80 nm on gr/MgO and on MgO. Both IBS and EDS sample were capped with a protective layer of Au. (c) EDS intensity ratios $I_{graphene}/I_{MgO}$, tracking temperature and element dependent changes in the cumulative sticking coefficient for Ni2MnGa on graphene covered MgO. Error bars are standard deviations on multiple regions of a given sample. (d,e) SEM images of the nominally 80 nm thick films grown at room temperature on graphene/MgO and MgO and capped with Au. (f,g) SEM images of the nominally 80 nm thick films grown at 625°C on graphene/MgO and MgO and capped with Au.

We grow films with nominal thickness of 20-80 nm on transferred graphene/MgO (001) via molecular beam epitaxy (MBE) using elemental effusion cell sources, with typical fluxes of 2.2×10^{13} atoms / ($cm^2\cdot s$) for Ni and 1.1×10^{13} atoms / ($cm^2\cdot s$) each for Mn and Ga. All samples were capped with ~ 20 nm of Au

at room temperature to prevent oxidation. The nominal Ni_2MnGa composition is based on quartz-crystal microbalance flux measurements that are calibrated to absolute fluxes via *ex-situ* IBS. This "nominal composition" is based on the assumption that the sticking-coefficient is 1 for every element on graphene; however, our EDX (EHT = 20 keV) and IBS experiments suggest that this assumption is not valid. Both of these techniques offer large sampling depths, which allow us to sum over all species that stick on the graphene, thus enabling us to extract the upper bound for sticking coefficients on gr / MgO.

IBS measurements (He^+, 4.9 MeV, $\theta = 8°$) of a nominally 20 nm thick Ni_2MnGa sample on graphene shows a significant reduction in sticking for Ni and Mn when compared to films directly grown on MgO (Fig. 3.6a). The growth was performed at 600 °C and the sample was half-covered with graphene such that both sides are exposed to the same incident atomic fluxes. Interestingly, the areal density of Ga on graphene is nearly the same as that for bare MgO (Fig 3.6a). EDX supports the IBS results, with Ga showing similar sticking on graphene vs on bare MgO while Ni and Mn experience a 50% decrease of sticking on graphene (Fig. 3.6b). Note the EDX sample was grown at 625 °C.

To further understand the observed stoichiometry differences on graphene we utilize scanning electron microscopy (SEM) imaging to assess the film morphology. Films on bare MgO appear relatively smooth regardless of the growth

temperature (Fig. 3.6e, g), while films grown on graphene have a disconnected island morphology at 625° C (Fig. 3.6f). We attribute the island growth mode to poor wetting on the low surface energy graphene. Three-dimensional island growth has been observed on other graphene systems, such as GaAs / gr / Si [21] and Mn / gr / Ge [118]. Metals on graphene have low adsorption energies compared to their cohesive energies, which explains their poor wettability [119]. We see a drastic change in the morphology of Ni_2MnGa films grown at low temperatures (Fig 3.6d). In fact, at a growth temperature of 30 °C, the morphology on graphene is the same as on bare MgO. This is due to improved sticking of Ni and Mn at lower temperatures. Figure 3.6 (c) shows EDX intensity ratios (filled circles), $I_{graphene}/I_{MgO}$, for every element as a function of temperature. This ratio is approximately equal to the sticking coefficient on gr / MgO. We normalize to the bare MgO since the sticking coefficient of metals on MgO is unity. Below 100 °C we see that the cumulative sticking coefficient for Ni, Mn and Ga is 1. As the growth temperature increases, the sticking of Ni and Mn decreases down to ~ 0.6 and ~ 0.5, respectively. We speculate this temperature dependence is due to decreased desorption rates and smoother morphology with less exposed graphene at lower temperature.

We attribute the lower sticking coefficient on graphene compared to MgO to the inert van der Waals surface of graphene, which lacks dangling bonds. Despite

having a higher vapor pressure than Ni and Mn, Ga has a nearly temperature-independent unity sticking coefficient on graphene. This could be due to Ga intercalation beneath the graphene, which is a phenomenon that has been demonstrated on gr / SiC interfaces [75]. To conclude, we have demonstrated that the growth of Ni_2MnGa on gr / MgO requires compensated Ni and Mn fluxes in order to achieve a stoichiometric film due low sticking coefficients on graphene. We speculate similar growth challenges with other Heusler alloys or transition metal oxides.

4 Nucleation selectivity and lateral coalescence of GaAs over graphene on Ge

This chapter is adapted from the following article:

S. Manzo, K. Su, M. S. Arnold, and J. K. Kawasaki, *Nucleation selectivity and lateral coalescence of GaAs over graphene on Ge (111)*, Manuscript submitted for publication (2023).

Author contribution: I performed graphene characterization prior to growth, which included Raman spectroscopy, AFM and SEM to determine the graphene coverage. I also conducted the GaAs film growth and characterization of structure and morphology (AFM, SEM, Raman, XRD, RHEED) along with the associated data analysis.

4.1 Abstract

Epitaxial lateral overgrowth (ELO) using patterned graphene-masks is a promising method to grow exfoliateable heteroepitaxial films with reduced dislocation densities. Previous works have highlighted the advantages of monolayer graphene as a mask material, but a clear understanding of the related kinetic factors that control nucleation selectivity and lateral coalescence is missing. Here, we investigate the influence of various growth conditions such as temperature, atomic

flux ratio and growth rate on the molecular beam epitaxial (MBE) growth of GaAs on partial coverage graphene masks on Ge (111). Microscopy, in-situ electron diffraction and photoemission demonstrate that elevated growth temperatures (T > 600 °C), low As/Ga flux ratios (~ 28) and moderate growth rates (~ 56 nm/h) improve surface diffusion and desorption rates, promoting excellent selective nucleation and full coalescence of films within 400 nm. Our findings have significant implications for optimizing thin film growth on graphene masks.

4.2 Introduction

Epitaxial lateral overgrowth (ELO) is a longstanding strategy for minimizing the dislocation density during heteroepitaxy of lattice mismatched materials [52,53,120,121]. Here, openings in an inert mask define nucleation sites on the exposed substrate, and the mask blocks the propagation of dislocations from the substrate. Recent studies suggest that monolayer graphene is an attractive mask material [89,122] compared to conventional SiO_2 and SiN_x masks. The weak van der Waals interactions of graphene enable high nucleation selectivity [89,122], new relaxation pathways including slip and bending to reduce the dislocations density [122], and the ability to exfoliate films and re-use substrates [122].

Open questions remain regarding the kinetics of selective growth and coalescence over patterned graphene. To what extent is selectivity driven by fast

surface diffusion on graphene versus desorption from graphene? What kinetic factors control the lateral coalescence?

Here we evaluate the growth conditions and underlying mechanisms that enhance nucleation selectivity, lateral overgrowth, and coalescence on graphene masks. We focus on the molecular beam epitaxial (MBE) growth of GaAs films on graphene masks on a Ge (111) substrate. The graphene is grown to 40-50% areal coverage by chemical vapor deposition, following Refs. [84,89,123]. Direct growth of graphene on Ge avoids the surface and interfacial contaminants that can result from graphene layer transfer [80]. Our use of stochastic 40-50% areal coverage, rather than top-down lithography and patterning, avoids possible contaminants and damage induced by photolithography and etching [124]. Finally, we choose (111)-oriented Ge because the (111) produces smoother graphene surfaces than Ge (001) [125] and can suppress the formation of GaAs antiphase domains when the growth is initiated with an As wetting layer [126].

We show how high growth temperatures (>600 °C), low As/Ga flux ratio, and modest growth rates combine to enhance the surface diffusion and desorption rates of GaAs on graphene, leading to selective nucleation and films that fully coalesce within 400 nm.

4.3 Results and discussion

Fig. 4.1 (a, top) shows an exemplary scanning electron microscopy (SEM) image of 40-50% coverage graphene on Ge (111). The graphene appears as dark hexagons in the secondary electron image, with hexagons ranging in size from ~ 100 nanometers to several microns and a typical spacing of L ~ 1μm between exposed Ge regions. The existence of a strong graphene *2D* mode in Raman point spectra confirms the identification of graphene hexagons.

Prior to GaAs film growth, the graphene on Ge(111) samples are outgassed in a high vacuum ($p < 5 \times 10^{-8}$ Torr) load-lock at 150 °C for at least two hours to desorb water on the surface. They are then transferred to an ultra-high vacuum MBE chamber ($p < 5 \times 10^{-10}$ Torr) and annealed up to 750 °C to desorb Ge-oxides at the graphene openings. Temperatures were measured using a pyrometer that was calibrated to the native oxide desorption temperature of a GaAs substrate. Fig. 4.1 (a, middle) shows a reflection high energy electron diffraction (RHEED) pattern of the surface after deoxidation, which is indicated by the appearance of well-defined streaks and a bright specular reflection (yellow arrow). In the RHEED we observe streaks corresponding to the reciprocal lattice spacings of Ge (black arrows) and of graphene (white arrows).

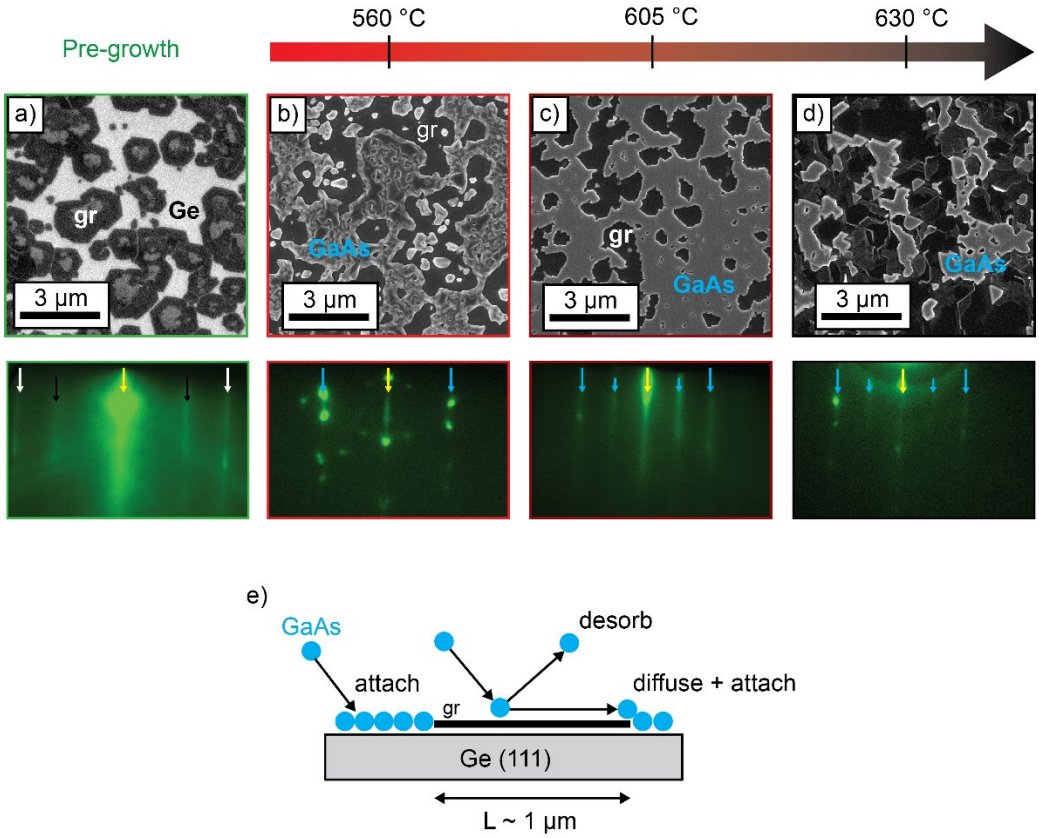

Figure 4.1 – Growth temperature dependence of nucleation selectivity on graphene / Ge (111). (a) CVD grown graphene on Ge (111) with 40-50% areal coverage, before GaAs film growth. The top panel is a secondary electron SEM image, middle is the reflection-high energy electron diffraction pattern after Ge-oxide desorption ([11$\bar{2}$] azimuth). (b) Growth of GaAs at 560 °C, showing parasitic nucleation on the graphene mask. (c) Growth at 605 °C, showing nucleation selectivity at the exposed Ge and not on the graphene mask. (d) growth at 630 °C, showing surface degradation. All films in this series were grown using a V/III atomic flux ratio of 28, Ga flux of 3.4×10^{13} atoms/cm^{2}s, and total time of 53 minutes. (e) Schematic of Ga and As adsorption, diffusion, attachment, and desorption on the partial graphene covered Ge (111) surface.

We first test the GaAs nucleation selectivity on graphene/Ge (111) as a function of growth temperature. Figs. 4.1 (b-d) show SEM images and RHEED patterns of GaAs films grown at temperatures from 560 to 630 °C. Growth temperatures were measured by a pyrometer and calibrated to the thermal deoxidation temperature of GaAs (001). The film was grown using an elemental Ga cell at a flux of 3.5×10^{13} atoms/cm^{2}s, and a mixture of As_2/As_4 from a thermal cracker cell with a cracker zone operated at 1200 °C. Growth rates are calibrated by RHEED oscillations for GaAs homoepitaxy. We use an As/Ga atomic flux ratio of 28. The As flux is estimated from the lower bound of the V/III growth window at a fixed temperature based on RHEED oscillations. The total growth time for each sample was 53 minutes for a total integrated flux ~1.1×10^{17} atoms/cm^2. This corresponds to a nominal thickness of 50 nm if the Ga sticking coefficient is 1, although we note that the GaAs sticking coefficient on graphene may be less than 1 [90]. We use the term *nominal thickness* when quoting thicknesses throughout this work to highlight our assumption of a unity sticking coefficient for GaAs on graphene.

For GaAs growth at 560 °C we observe poor nucleation selectivity (Fig. 4.1b). In the SEM image we observe GaAs growth on both the exposed Ge regions and on the graphene mask. The RHEED pattern displays polycrystalline spots, which we attribute to polycrystalline island growth on the graphene regions.

For growth at 605 °C we observe excellent selectivity (Fig. 4.1c). SEM images reveal a smooth GaAs morphology on the Ge regions and no obvious parasitic nucleation on the graphene regions. The corresponding RHEED patterns are streaky and show a 2 × 2 surface reconstruction, indicating a relatively smooth and crystalline GaAs surface with long-range ordering. This 2 × 2 reconstruction is consistent with previous reports [127–129].

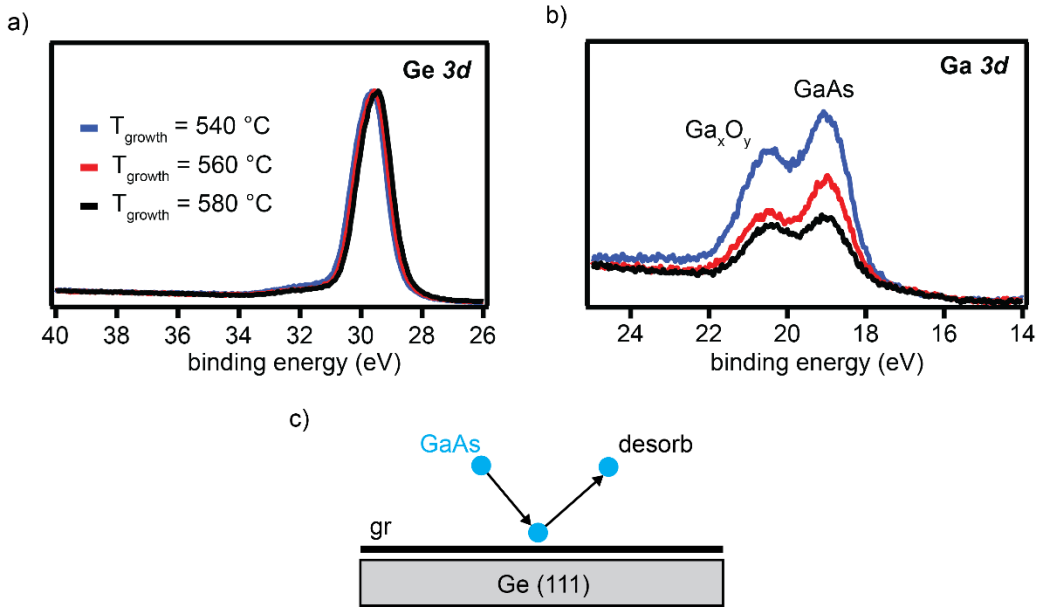

Figure 4.2 – Effect of growth temperature on GaAs desorption. (a,b) Ex-situ photoemission spectra (Al Kα hν = 1486.6 eV) of the Ge and Ga *3d* core levels after GaAs growth on full-coverage graphene / Ge (111) (nominal thickness 40 nm) grown at various temperatures. The Ga-oxide component is due to air exposure. (c) Schematic of the adsorption and desorption process of GaAs on full-coverage gr / Ge (111).

For growth at 630 °C we observe a significant decrease of the RHEED intensity and a disconnected islands morphology in the SEM image (Fig. 4.1d), which we attribute to thermal decomposition of GaAs and possible reactions with the graphene.

We attribute the strong temperature dependence of nucleation selectivity to two factors, desorption and diffusion on graphene, as illustrated in Fig. 4.1 (e). First, due to the weak van der Waals interactions of graphene, adatoms that land on the graphene are anticipated to have a high probability of desorption, that is, the sticking coefficient on graphene is expected to be low [90,91,130]. This desorption rate from graphene should increase with temperature, whereas desorption from the covalent Ge surface or growing GaAs surface is nearly temperature independent for growth temperatures below 600 °C. Second, adatom diffusion on graphene is expected to be large and increase with temperature [89]. With increasing temperature, adatoms that land on graphene are more likely to diffuse and then attach to exposed Ge regions [80]. This crossover is expected to occur when the diffusion length λ becomes larger than the characteristic spacing $L \sim 1$ μm between exposed Ge regions.

To understand the relative importance of desorption versus surface diffusion on our partial coverage graphene/Ge surfaces, we perform *ex-situ* x-ray photoemission spectroscopy (XPS) measurements on a series of GaAs samples

grown on full coverage graphene on Ge (111), grown to a nominal thickness of 40 nm. Since the graphene covers the entire surface, this tests the relative importance of desorption, independent of the diffusion length (Fig. 4.2c). With increasing growth temperature from 540 to 560 °C, we observe a ~ 50% reduction in the integrated Ga 3d core level intensity (normalized to Ge 3d from the substrate), suggesting a significant increase in the desorption rate at higher temperature. This suggests that temperature dependent desorption from graphene plays a strong role in the selectivity. Further experiments are required to quantify the diffusion length on graphene, independently from desorption.

In addition to the growth temperature, the key synthesis parameters of growth rate and As/Ga flux ratio are also expected to tune the desorption rate and diffusion, and ultimately the nucleation selectivity. Fig. 4.3 summarizes the impacts of these growth parameters. We find that increasing the growth rate from 56 nm/h (3.5×10^{13} Ga atoms/cm^{2}s) to 186 nm/h (1.2×10^{14} Ga atoms/cm^{2}s) decreases the nucleation selectivity, as the SEM images reveal GaAs islands on the graphene regions (Fig. 4.3 (a)). We attribute the decreased selectivity to the combination of decreased effective diffusion time and desorption time at higher growth rates. Increasing the As/Ga atomic flux ratio from 28 to 58 also decreases the nucleation selectivity, as we observe an increase in parasitic GaAs islands on graphene for

growth at a flux ratio of 58 (Fig. 4.3b). We attribute this to a decrease in the Ga diffusion length at high As/Ga flux ratios [131].

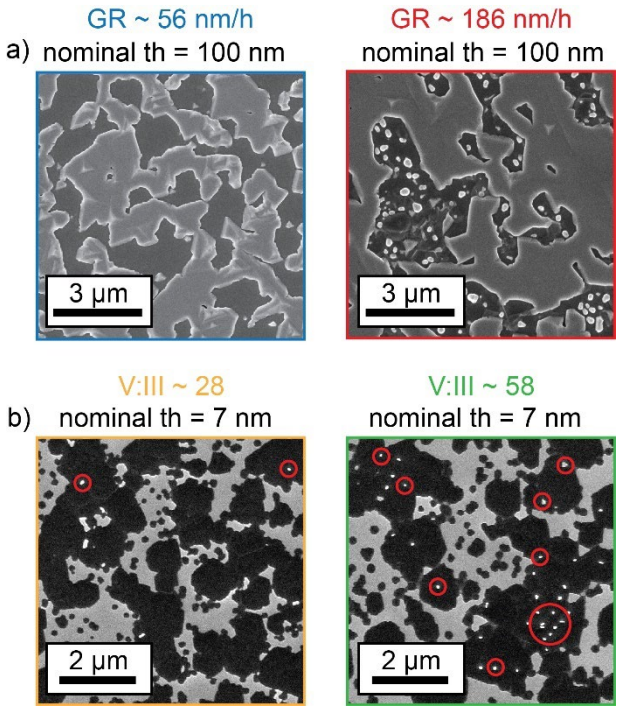

Figure 4.3 - Effect of atomic flux ratio and growth rate on nucleation selectivity. (a) SEM images of samples grown using a Ga fluxes of 3.5×10^{13} Ga atoms/cm^{2}s and 1.2×10^{14} Ga atoms/cm^{2}s, corresponding to nominal growth rates (GR) of 56 nm/h and 186 nm/h for a Ga sticking coefficient of 1. (b) SEM images of samples grown using a As/Ga atomic flux ratio of 28 and 58. The red circles highlight parasitic GaAs nucleation on the graphene.

Figure 4.4 tracks the thickness evolution of GaAs growth on graphene/Ge (111) at 605 °C and As/Ga flux ratio 28, from selective nucleation to complete lateral coalescence. SEM and AFM measurements show that the first few

nanometers of GaAs nucleate at the exposed germanium regions (Fig. 4.4a), with minimal lateral overgrowth. After 30 nm of nominal growth, GaAs completely covers the ~ 100 nm diameter graphene islands while the larger ~ 1 μm graphene hexagons remain exposed. Lateral overgrowth on the larger 1 μm graphene islands starts to occur after 50 nm of deposition, as evidenced by the smoothening of the previously faceted graphene hexagon edges. The lateral growth is fastest from 30 nm to 50 nm of nominal growth (Fig. 4.4b). AFM images reveal that a pyramidal GaAs morphology begins to emerge around 50 nm nominal thickness. With increasing thickness, the areal coverage of GaAs slowly increases, until the entire surface is covered after about 420 nm of growth (Fig. 4.4b). The pyramidal morphology is more pronounced after complete coalescence. Using AFM height profiles and cross-sectional SEM, we extract the vertical heights of the films at each nominal thickness (Fig. 4.4c). It is clear that the GaAs sticking coefficient is less than unity since the measured step heights are lower than the nominal thicknesses. We expect the sticking coefficient to approach 1 after the entire sample surface is covered by GaAs (> 420 nm nominal thickness).

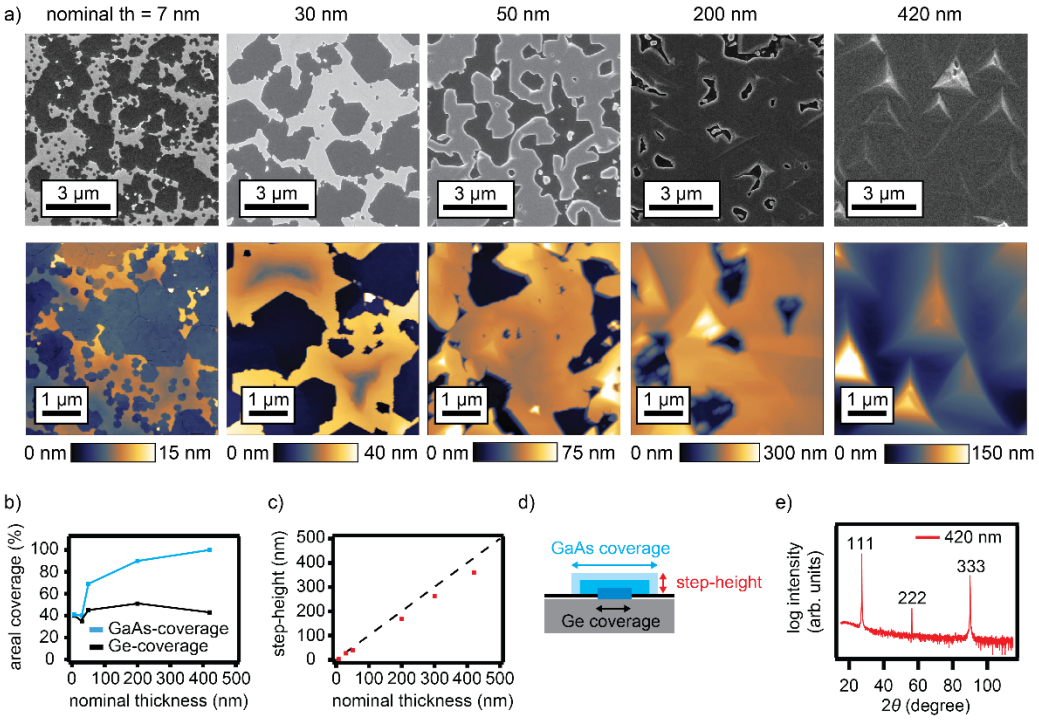

Figure 4.4 – Complete lateral coalescence of GaAs film grown at 605 °C over graphene. (a) SEM and AFM images tracking the nucleation of GaAs on exposed Ge openings (7 nm), the overgrowth over graphene islands (30 - 200 nm), and the complete coalescence across the entire sample surface (420 nm). (b) Areal coverage percent as a function of nominal thickness (extracted from QCM-calibrated Ga fluxes). (c) Step-heights of GaAs extracted from AFM measurements as a function of nominal thickness. A line of equality (y = x) is included to illustrate any deviations from purely vertical growth. (d) Illustration depicting the lateral and vertical growth of GaAs at exposed Ge regions. (e) X-ray diffraction pattern of the coalesced 420 nm GaAs film.

It should be noted that the pyramid morphology which onsets at a nominal thickness of 50 nm is not unique to growth on graphene masks. Pyramidal hillocks with {110} facets are commonly observed for (111) oriented GaAs growth [132,133]. We find that increasing the growth temperature can improve the

morphology of coalesced films and produce flatter surfaces. In Fig. 4.5 we show a series of films grown to a nominal thickness of 50 nm. We find that with increasing growth temperature the morphology changes from pyramidal at 590 °C to flat at 615 °C. Other strategies to improve the morphology may include growth on vicinal substrates or employing chemical pre-treatments or wetting layers [134].

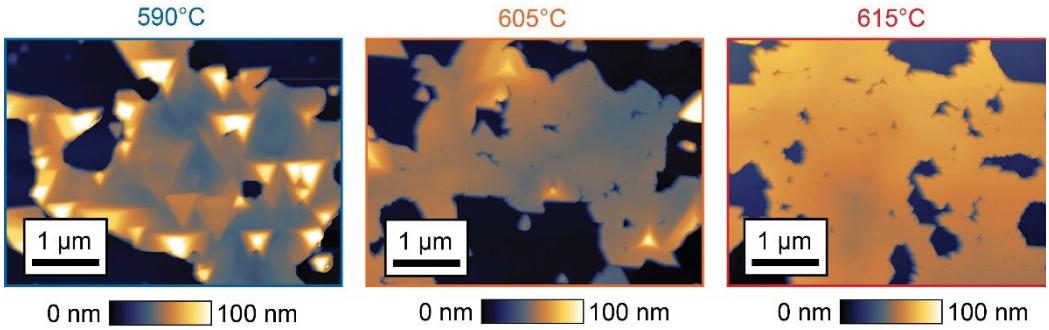

Figure 4.5 – Temperature effect on GaAs morphology. AFM height images of three samples grown at similar temperatures, between 590 °C and 615 °C, and nominal thickness of 50 nm. The pyramidal morphology is favored at the lower bound of this temperature range and a smoother film is obtained at 615 °C.

4.4 Conclusion

In summary, we showed that temperature dependent desorption plays a significant role in the nucleation selectivity of GaAs films on partial coverage graphene / Ge(111). Slower growth rates and low As/Ga flux ratios also enhance the selectivity. Further experiments and theory are needed to fully quantify the

relative importance of surface diffusion on graphene and to optimize the graphene feature size to match the characteristic diffusion length.

Under the conditions optimized for nucleation selectivity, we find that GaAs coalescence over the graphene occurs at a nominal thickness near 400 nm. Further improvements are possible by employing two step growth methods: a first step that optimizes nucleation selectivity, followed by a second step that optimizes lateral growth rates and minimizes the formation of pyramidal hillocks.

5 Alternate growth mechanisms on graphene: intercalation & carbide formation

5.1 Gallium intercalation at the graphene/Ge interface

The controlled insertion of atoms or molecules between graphene and the substrate, known as intercalation, is a novel method to synthesize epitaxial quantum materials. Due to quantum confinement and a mixed-bonding environment (van der Waals bonding with the graphene overlayer and covalent bonding with the underlying substrate), 2D intercalated materials have shown unusual properties not shared by their bulk counterparts. For example, intercalated 2D Ag is a large bandgap (>1 eV) semiconductor [135] and 2D Ga exhibits an enhanced superconducting transition temperature compared to the bulk [136]. Large-area 2-dimensional nitrides [74], oxides [103], metals [75] have been successfully intercalated at the graphene /SiC interface. An additional benefit of this synthesis technique is the passivation of the intercalated material by the graphene, which has been shown to undergo “healing” after the intercalation process [75]. This allows materials that typically degrade upon exposure to oxygen to be environmentally stable [137].

Intercalation is typically done by depositing films on defective graphene/substrate interfaces followed by annealing to drive the adatoms under the graphene through defects. Although remote epitaxial growth on graphene is typically done at elevated temperatures, the growth process is remarkably similar. We know that graphene will always have some defects to different extents depending on the system. Keeping this in mind, unintentional intercalation could be taking place during growth on graphene.

Intercalation has been largely limited to gr / SiC substrates, while the potential of graphene intercalation on other systems has remained unexplored. Graphene on germanium offers unique advantages, including cost-effectiveness and commercial relevance. Additionally, the synthesis of graphene on germanium substrates is a relatively simple process that requires significantly lower growth temperatures in comparison to graphene growth on SiC [84,95]. Exploring intercalation in gr/Ge heterostructures could unlock novel electronic properties and lead to technologically significant advancements in diverse applications, making this research area highly promising and deserving of further investigation.

Here we study the intercalation of Ga at the graphene / Ge interface via molecular beam epitaxy through *in-situ* reflection high electron diffraction (RHEED) and *ex-situ* spectroscopy and imaging techniques. We have discovered promising signs of intercalation that seem to be mediated by defective graphene

wrinkles and graphene edges. This is based on distinct changes in atomic force microscopy (AFM) phase imaging and secondary electron contrast in scanning electron microscopy (SEM) after growth. Additionally, photoemission and Raman spectroscopy confirm doping of the graphene sheet, while RHEED suggests long-range ordering of the surface after growth.

Figure 5.1 (a, left) shows an exemplary AFM height and phase image, along with a corresponding RHEED pattern, of gr/Ge (111) before growth. The graphene is grown via atmospheric chemical vapor deposition following Refs [84,123]. Several micron-wide terraces can be seen in the height image, which are typical for gr/Ge (111) [85]. Additionally, a large wrinkle can be seen running vertically across the sample with a height of > 5 nm (Fig. 5.1a, top-left). The wrinkle appears bright in the AFM phase contrast. Grain boundaries are clearly visible as well and exhibit a darker contrast in the phase image (Fig. 5.1a, bottom-left). The RHEED pattern, along a $<11\bar{2}>$ azimuth, is streaky with two distinct spacings corresponding to the Ge (yellow arrows) and the graphene (white arrow) first-order reflections.

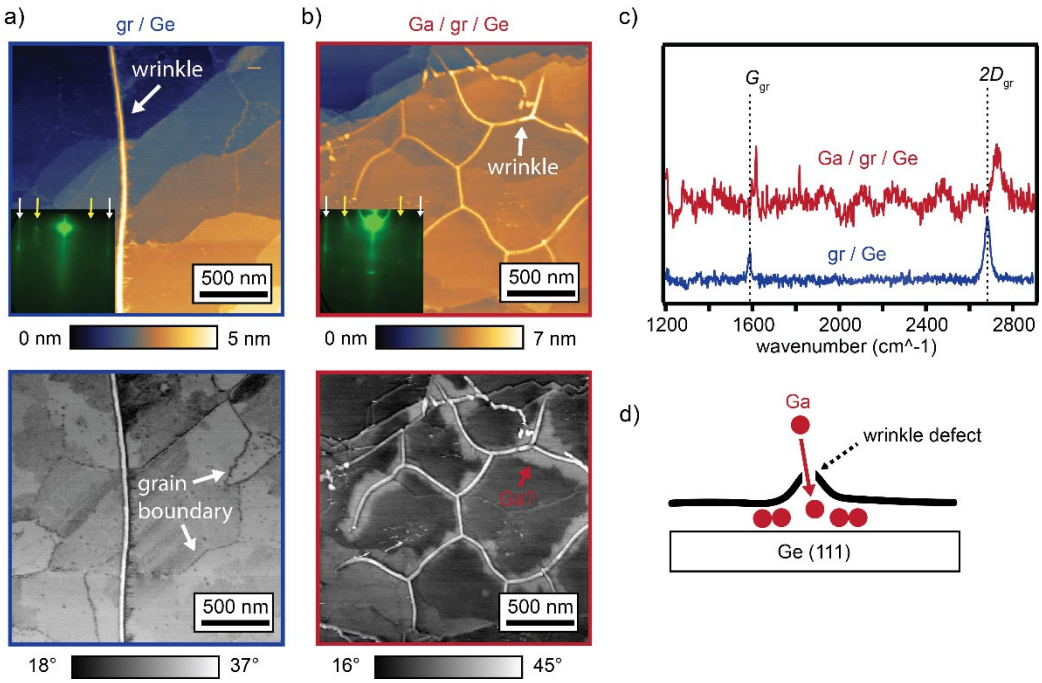

Figure 5.1 – Characterization of gallium growth on graphene/Ge (111). (a-b) AFM height and phase images of a sample before (a) and after (b) gallium growth, showing distinct changes in phase around graphene wrinkles. Insert: RHEED patterns along a [11$\bar{2}$] azimuth of the gr/Ge before and after Ga deposition. (b) Representative Raman spectra of graphene/Ge (111) before and after growth. (c) Illustration depicting possible gallium intercalation mechanism.

Gallium is then grown at 600 °C, a relatively high growth temperature, to drive intercalation. After 4 nm of Ga deposition, the RHEED pattern no longer looks streaky, and there are faint arcs at a Q-spacing that aligns with the Ge first-order reflections (Figure 5.1b, inset). Raman spectroscopy after gallium synthesis shows that the G and 2D phonon modes of graphene are blueshifted by 29 cm-1 and 45 cm-1, respectively (Figure 5.1c), indicative of changes in strain or doping

of the graphene [138]. AFM height images show an increase in the graphene wrinkle density, which likely occurs during sample cooling due to the thermal expansion mismatch between graphene and the germanium substrate [139]. The most intriguing phenomenon, however, is the AFM phase contrast that is localized around the graphene wrinkles (Figure 5.1b, bottom-right). We attribute this light-gray contrast to intercalated Ga. In the first demonstrations of metal intercalation on gr/SiC, graphene defects formed by oxygen plasma acted as "doors" that allowed the incoming metal atoms to intercalate through [75]. Graphene wrinkles could serve a similar purpose, since they are known to be defective and chemically reactive sites (Fig. 5.1d) [98]. Additionally, AFM phase contrast has been shown to be an effective technique in distinguishing graphene layer thicknesses [140] and differences in elastic moduli across a surface [141]. Therefore, it is not unreasonable for regions of intercalated Ga to exhibit a markedly different phase in the AFM images.

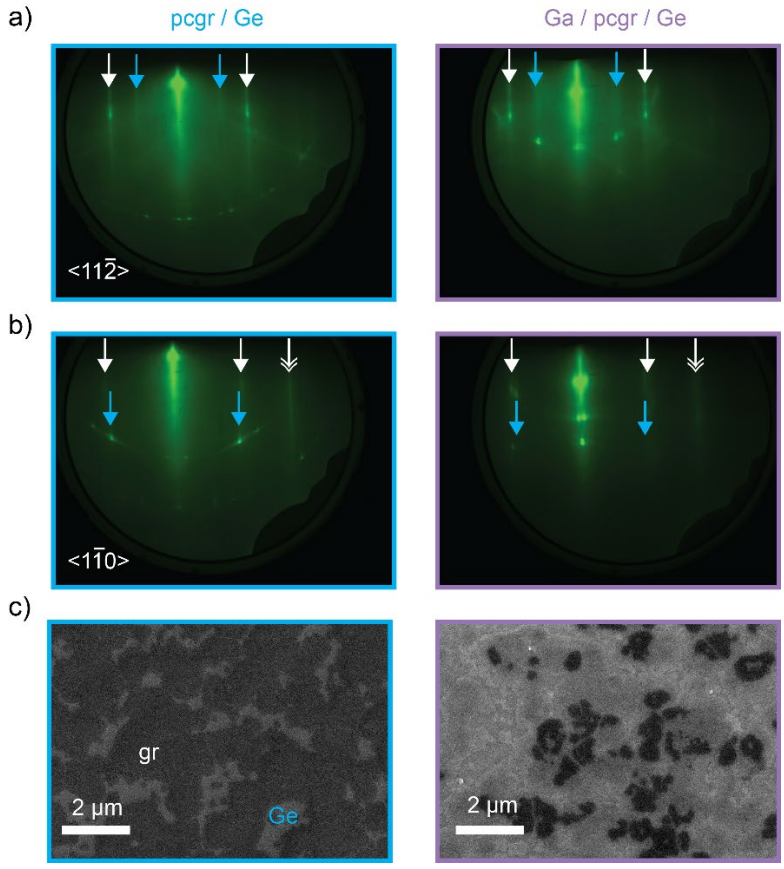

Figure 5.2 – Ga growth on partial-coverage gr / Ge (111). a) RHEED images along a <11$\bar{2}$> azimuth before (blue) and after (purple) Ga growth. The white arrows denote the graphene reflections (single - 0° degree rotated, double - 30° rotated). b) RHEED images along a <1$\bar{1}$0> azimuth before (blue) and after (purple) Ga growth. c) Secondary electron SEM images of the sample before and after Ga deposition.

Instead of producing stochastic openings in the graphene through oxygen plasma etching, we utilize partial-coverage graphene/Ge (111) to promote increased Ga intercalation. The edges of the partially coalesced graphene hexagons are highly reactive sites that could act as pathways for the incoming Ga atoms.

These samples have a graphene coverage of approximately 80%. We use the same Ga growth conditions as the full-coverage case and do ex-situ AFM and SEM to study the post-growth morphology. The RHEED pattern after growth depicts an atomically smooth surface with long-range order (Figure 5.2a, b). The SEM images reveal a remarkable change in secondary electron contrast after growth. Before growth, the graphene appears as dark, interconnected hexagons in the secondary electron image while the germanium regions display a lighter contrast (Fig. 5.2c). After growth, the dark graphene hexagons exhibit a lighter contrast, which is similar to the bare Ge regions. Faint outlines of the graphene edges can still be observed in the images. The similarity in contrast between the bare Ge and graphene covered regions seems to suggest that intercalation is taking place. It is worth pointing out the dark "splotches" near the center of the large graphene regions. These "splotches" have the same secondary electron contrast as the graphene before growth. We attribute these dark regions to those that have no intercalated Ga underneath. Secondary electron contrast is an established way to tell if intercalation is taking place underneath gr/SiC [142].

Photoemission reveals that Ga is present after growth for both the full-coverage and partial coverage graphene substrates, which supports our interpretation of the morphological characterization. There are some notable

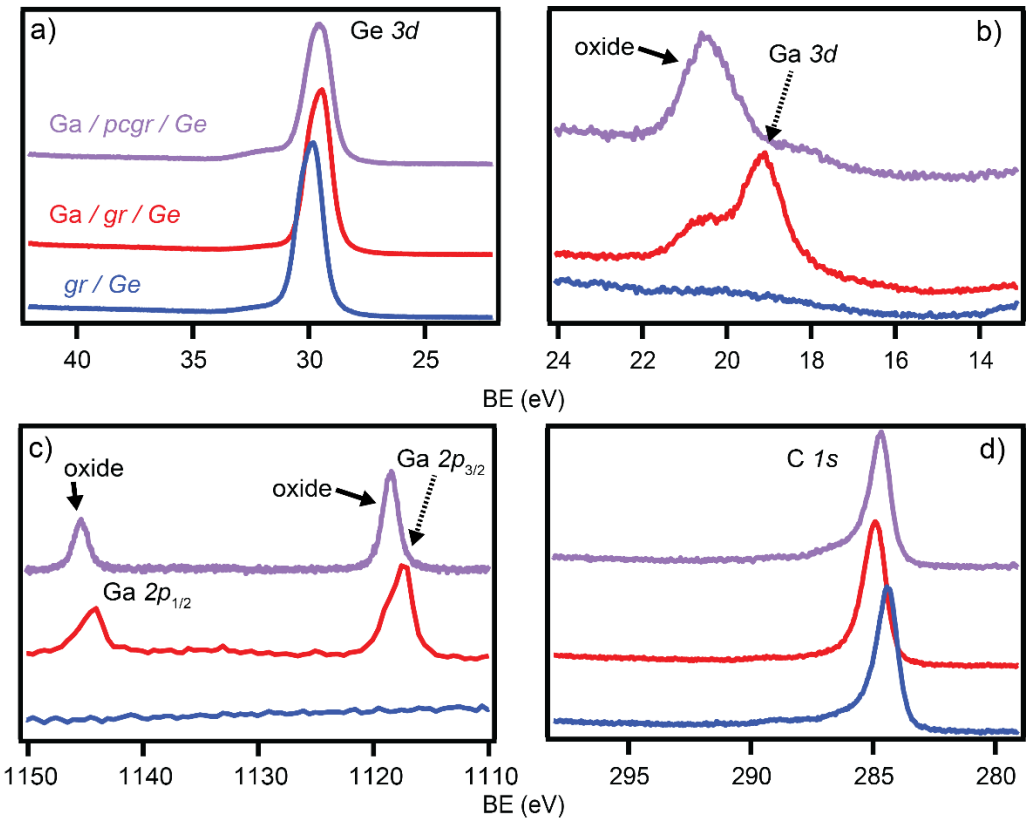

Figure 5.3 – Ex-situ XPS (Al Kα hν =1486.6 eV) spectra measured before and after Ga deposition on gr/Ge (111) and pcgr/Ge (111). (a) Ga $2p_{3/2}$ & $2p_{1/2}$ (b) Ga *3d* (c) Ge *3d* (d) C *1s*.

differences between the samples, however. While both samples exhibit a Ga-oxide component ~1.5 eV higher than the Ga *2p* and *3d* core levels, the Ga / pcgr / Ge sample has much more Ga-oxide relative to pure Ga (Fig. 5.3b, c). This is not entirely surprising, since there is more exposed Ge-regions where nucleated Ga is not being passivated by the graphene. It is also possible that the graphene edges enable lateral oxidation of intercalated Ga, which would mean that the partial-

coverage sample could promote the formation of 2D-Ga oxide. *In-situ* photoemission, high-resolution cross-sectional TEM and theoretical calculations are required to say which specific oxidation state and crystal structure the Ga-oxide adopts at the graphene/Ge interface. The C *1s* is shifted for both the full- and partial-coverage samples after growth, by 0.5 and 0.3 eV respectively (Fig. 5.3d). This is likely due to electron/hole doping of the graphene by Ga [75,143]. Although SEM and AFM images suggest that there are not many Ga islands/particles above the surface of graphene after growth, we cannot discount the possibility that some of the Ga photoemission intensity is originating from Ga above the graphene. Future depth dependent *in-situ* XPS experiments could reveal if this is the case.

To conclude, we have done some preliminary characterization of Ga grown on full- and partial-coverage graphene / Ge (111) to investigate the possibility of intercalation in this system. AFM phase imaging and SEM secondary electron contrast show distinct changes after Ga growth, which are suggestive of Ga intercalation. Despite not seeing many Ga islands above the graphene by SEM and AFM, *ex-situ* XPS reveals that there is Ga and Ga-oxide on the sample. Intercalated Ga-oxide at the gr/Ge interface would be equally as exciting as pure Ga. Recently, crystalline monolayer GaO_2 and bilayer Ga_2O_3 were intercalated at the gr / SiC interface via confined heteroepitaxy [112]. Due to quantum confinement effects, the intercalated 2D-Ga2O3 (ferroelectric-wurtzite structure) had a band gap of 6.6

"±" 0.6 eV, which is even larger than bulk Ga2O3 (4.8 eV [113]). Our results motivate further study of intercalation of metals at the graphene / Ge interface.

5.2 Gadolinium carbide formation on graphitic surfaces

Despite graphene being an incredibly inert material, it has been known to react with several transition and rare-earth metals at elevated temperatures to form interfacial carbides [144–147]. These carbides could allow for novel epitaxial relationships during thin film growth on graphene. For example, interfacial Ni-carbides formed during the CVD growth of graphene on Ni (111) result in rotated graphene grains that are not aligned to the Ni substrate [145]. In addition, several interfacial Gd-carbides have been produced by annealing Gd grown on highly-oriented pyrolytic graphite (800 – 1400 K) [104]. These annealing temperatures are close to the growth temperature of many Heusler films, including GdPtSb, which exhibited a unique *R*30 domain on gr/sapphire that could not be explained by pinhole or van der Waals epitaxy [102]. We attributed this 30°-degree rotated domain to remote interactions, but we couldn't completely rule out interfacial Gd-carbide formation. The possibility of interfacial carbide formation and its implications on epitaxy on graphene has been largely unexplored. Here we investigate Gd growth and annealing on HOPG and gr / sapphire to determine if Gd-carbides can form at graphitic interfaces during MBE growth of Heuslers. X-ray diffraction results show we have likely synthesized Gd_2C on HOPG. Additionally, AFM and SEM images of annealed Gd / gr / sapphire exhibit an unusual morphology which might be suggestive of carbide formation.

Although several Gd-carbides can form on HOPG [104], Gd_2C (trigonal, $R\bar{3}m$) is of particular interest. Gd_2C is a layered 2D-electride, a class of material in which excess electrons behave like anions that are trapped at interstitial positions in the crystal structure [148–151]. These interstitial anionic electrons (IAEs) do not participate in bonding, and in the case of the layered $[Gd_2C]^{2+} \cdot 2e^-$ structure, the electrons are localized in a 2D-plane, effectively behaving like a 2-dimensional electron gas (2DEG) [152,153]. This special electronic configuration results in remarkable properties. Due to the "loose" IAEs, Gd_2C has a very low work function which makes it useful for vacuum emitters [154]. Additionally, the IAEs have their own quasi-atomic magnetic moments which trigger ferromagnetic spin alignments within the antiferromagnetic $[Gd_2C]^{2+}$ lattice [153]. Weyl semi-metallic states are predicted due to these unusual magnetic properties that break time-reversal symmetry, thus making Gd_2C a candidate for a topological electride [155]. Some of these intriguing properties have not been experimentally demonstrated, since Gd_2C has not been synthesized in thin-film form.

We first focus on growing Gd on HOPG by MBE. This is a simpler starting point since HOPG has more available carbon that can interact with the deposited Gd film. HOPG substrates are cleaved prior to growth to obtain a clean growth surface. The substrate is mounted using a diluted high-performance Ag paste on a molybdenum puck. The paste is cured in a high-vacuum ($p < 5 \times 10^{-6}$ Torr)

outgassing prep-chamber at ~ 150 °C for at least two hours. Prior to growth the sample is additionally outgassed up to 600 °C inside our MBE growth chamber ($p < 5 \times 10^{-10}$ Torr).

Figure 5.4 (a) shows our approach for synthesizing Gd-carbide films on HOPG, which consists of three steps: 1) deposition of ~ 15 nm of Gd at room temperature 2) annealing up to 750 °C induce carbide formation 3) capping the sample with amorphous Ge at room temperature. The RHEED pattern of HOPG is isotropic due to no long-range order in-plane (Fig. 5.4b). The solid arrows correspond to the first-order reflections of HOPG (white) and Gd (yellow). The double arrows correspond to the first order reflections of the 30° rotated domains of HOPG and Gd (Figure 5.4 b-c). These reflections were converted from pixels to reciprocal space units by using a homoepitaxial GaAs film as a calibration sample.

After annealing the sample up to 500 °C, the RHEED pattern becomes streakier, indicating the surface is becoming smoother (Figure 5.4d). According to previous photoemission studies of Gd_xC_y formation on HOPG, Gd_2C_3 and GdC_2 form above 800 K (527 °C) and above 1000 K (727 °C), respectively (Figure 5.4f) [104]. After gradually increasing the annealing temperature up to 750 °C, we see a substantial increase in amorphous diffuse scattering, as evidenced by the hazy RHEED pattern (Figure 5.4e). This could be due to a chemical reaction taking place at the surface. Additionally, the Gd streaks are significantly dimmer. This is

accompanied by a large increase in the MBE pressure, which rises from ~ 9×10^{-10} Torr at 500 °C, up to 1×10^{-8} Torr at 750 °C. We attribute this increase to the low sticking coefficient of metals on graphitic surfaces, which can lead to desorption of the metal species at elevated temperatures [90]. It is worth noting that no additional streaks at other Q-spacings were observed as a function of annealing, which would indicate that no crystalline carbides are forming at the surface. The Gd films are fairly thick in comparison to the penetration depth of the grazing-incidence electrons [156]; therefore, it is unlikely that any carbide formation that occurs at the buried Gd / HOPG interface would be visible in RHEED.

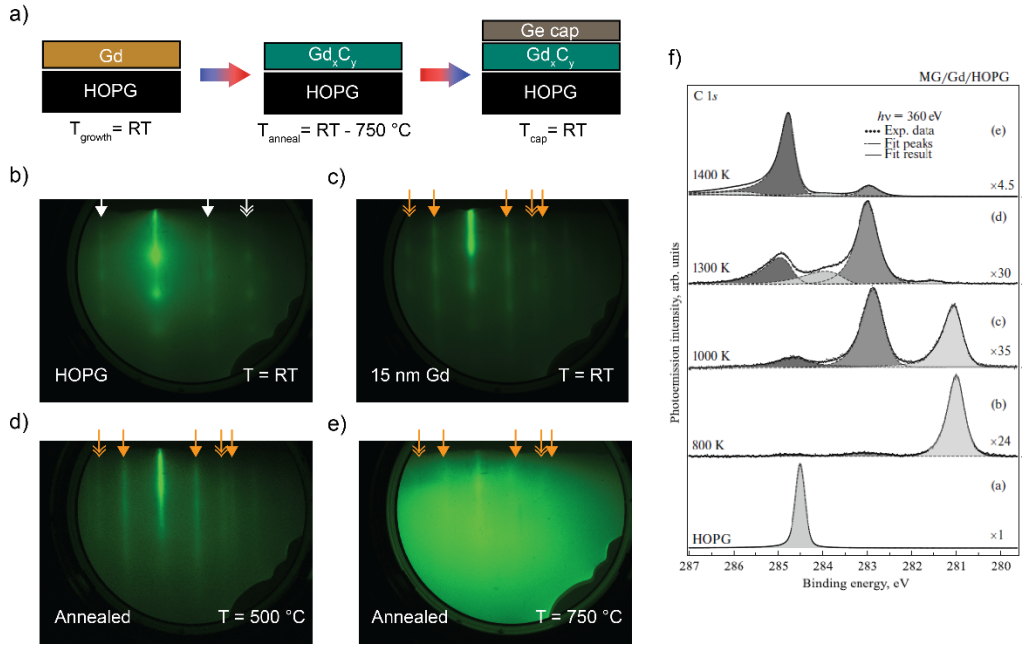

Figure 5.4 – Gd growth on HOPG. (a) Illustration depicting the heterostructure and the growth process flow. (b) RHEED pattern of HOPG prior to growth. The solid white arrows correspond to the Q-spacing of the primitive unit cell, while the double arrow marks the Q-spacing of the 30°- rotated HOPG domains. (c) RHEED pattern of 15 nm of Gd / HOPG. The solid gold arrows mark the Q-spacing associated with the primitive Gd unit cell, while the double arrows correspond to the 30°- rotated Gd domains. (d) RHEED pattern of the 15 nm Gd film after annealing at 500 °C. e) RHEED pattern of the 15 nm Gd film after annealing at 750 °C. (f) XPS data from [104] showing the C 1s core level after annealing Gd / HOPG.

We perform *ex-situ* X-ray diffraction in order to determine if any crystalline gadolinium carbides have formed after annealing. Figure 5.5 (a) shows a the XRD patterns of three 15 nm Gd / HOPG samples that have been annealed up to different temperatures. The asterisks in the patterns mark metallic contaminants in the HOPG substrates, which are unrelated to the Gd growth. The only sample that exhibits Gd

related reflections is the unannealed one (Fig. 5.5a). This result, and the diffuse scattering in RHEED at 500 °C and above, supports the idea that a chemical reaction could be taking place at elevated temperatures that is consuming the Gd.

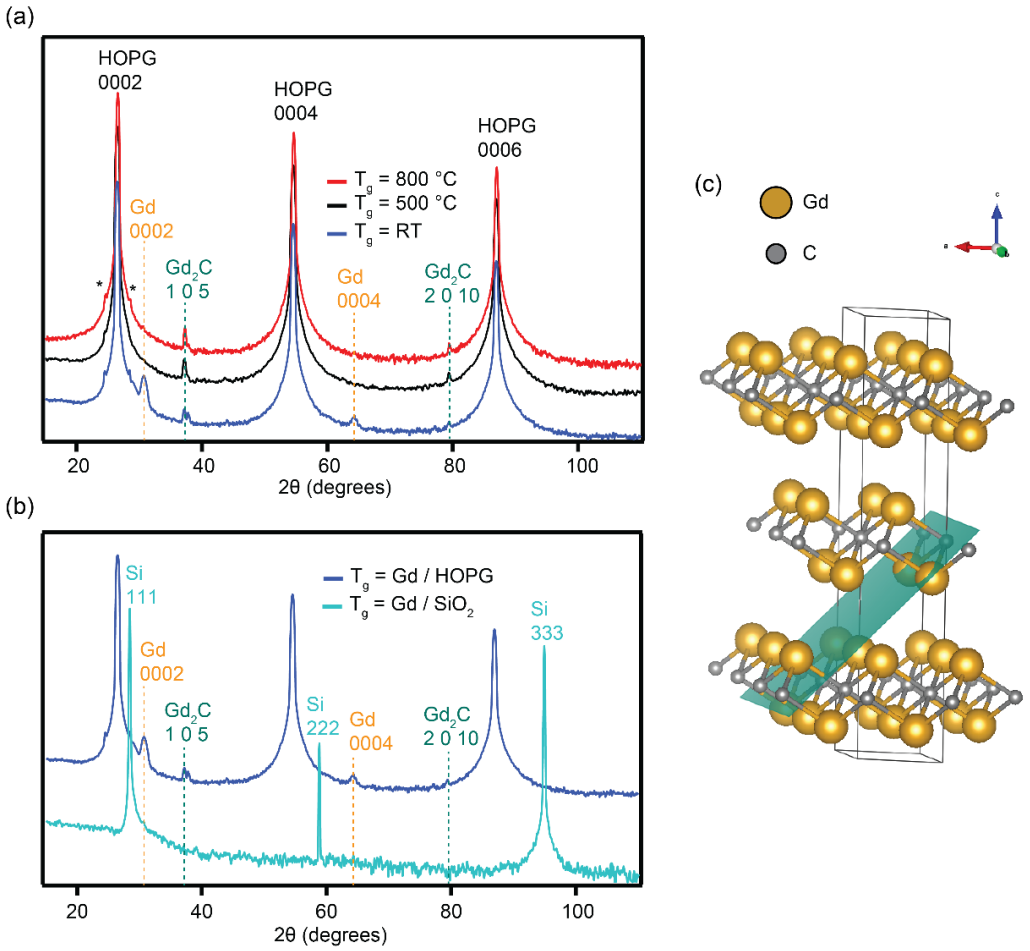

Figure 5.5 –Crystal structure of Gd / HOPG films. (a) XRD 2θ-ω scan of Gd / HOPG samples annealed at different temperatures. (b) XRD patterns of Gd grown on SiO2 and Gd grown on HOPG. (c) Illustration depicting the crystal structure of Gd_2C with the (105) plane highlighted in green.

The other significant feature in the XRD patterns is the appearance of two peaks at $2\theta = 37.20°$ (P_1) and $2\theta = 79.40°$ (P_2). These peaks are very close to the 1 0 5 and 2 0 10 reflections of Gd_2C [153]. However, Gd_2O_3 also has peaks that closely match the ones observed in the pattern corresponding to the 4 2 0 and 8 4 0 planes. Yet, the presence of crystalline Gd_2O_3 in the XRD scans is unlikely. Firstly, the structure factors ratios of the two relevant reflections of Gd_2O_3 do not match the integrated intensity ratios for the observed peaks (Table 5.1). In addition, a control sample was created by growing 15 nm of Gd on an amorphous SiO_2 / Si (111) substrate. The Gd was uncapped, guaranteeing that oxidization would take place upon removing from vacuum. The peaks at $2\theta = 37.20°$ and $2\theta = 79.40°$ we observed for the Gd / HOPG samples are not present in XRD scan for the control sample (Figure 5.5b, cyan curve). This result, along with the structure factors ratios of Gd_2O_3, are strong indicators that the peaks of interest are likely Gd_2C. On the other hand, it remains unclear why this particular orientation is stabilized after growth. It is particularly surprising because these sets of planes are not the brightest ones as determined by the structure factor. One would expect the film to be (00l)-oriented out of the plane. Further experiments are needed to understand the preferred orientation of Gd_2C on HOPG.

Table 5.1 – Comparison of observed peak intensity ratios (P_1/P_2) and structure factor ratios for the relevant reflections of Gd_2C and Gd_2O_3.

$I_{P1} / _{P2}$	Gd_2C: $I_{1\,0\,5} / I_{2\,0\,10}$	Gd_2O_3: $I_{4\,2\,0} / I_{8\,4\,0}$
2.7	3.2	0.12

We also grow Gd on gr / c-sapphire to test the possibility of Gd reacting with graphene to form a carbide (Figure 5.6a). The graphene is transferred to sapphire from copper foil using an adapted wet transfer technique as described in the methods section of Ref [44]. Like the growths on HOPG, we deposit Gd at room temperature and then anneal in ultra-high vacuum. However, since there is only a one-atom-thick sheet of carbon in this case, we only deposit two monolayers of Gd. This thickness should result in the formation of the Gd_2C electride, if we do produce a carbide. Figure 5.6 (b) and (c) show RHEED patterns before and during the growth process along the $<11\bar{2}0>$ and $<11\bar{1}0>$ azimuthal directions, respectively. Despite the presence of a graphene overlayer, the first-order diffracted spots from the sapphire substrates can be seen in either direction (grey arrows). After the deposition of 2ML of Gd, we see streaks associated with the first-order reflections of Gd (solid yellow arrows) and 30° rotated domains (yellow double arrows). The RHEED pattern is largely isotropic as evidenced by streaks with the same Q-

spacings being present in either crystallographic direction of the sapphire substrate. No well-defined in-plane orientation is expected, because the CVD graphene grown on copper foil that was transferred to sapphire is polycrystalline [157]. The RHEED patterns do indicate that there is a weak a directional dependence of the streak intensities associated with the 0° and 30° rotated Gd domains. Along the $<11\bar{2}0>$ azimuth, the 30° rotated domains appear brighter than the 0°. The opposite effect can be seen along the $<10\bar{1}0>$ azimuth.

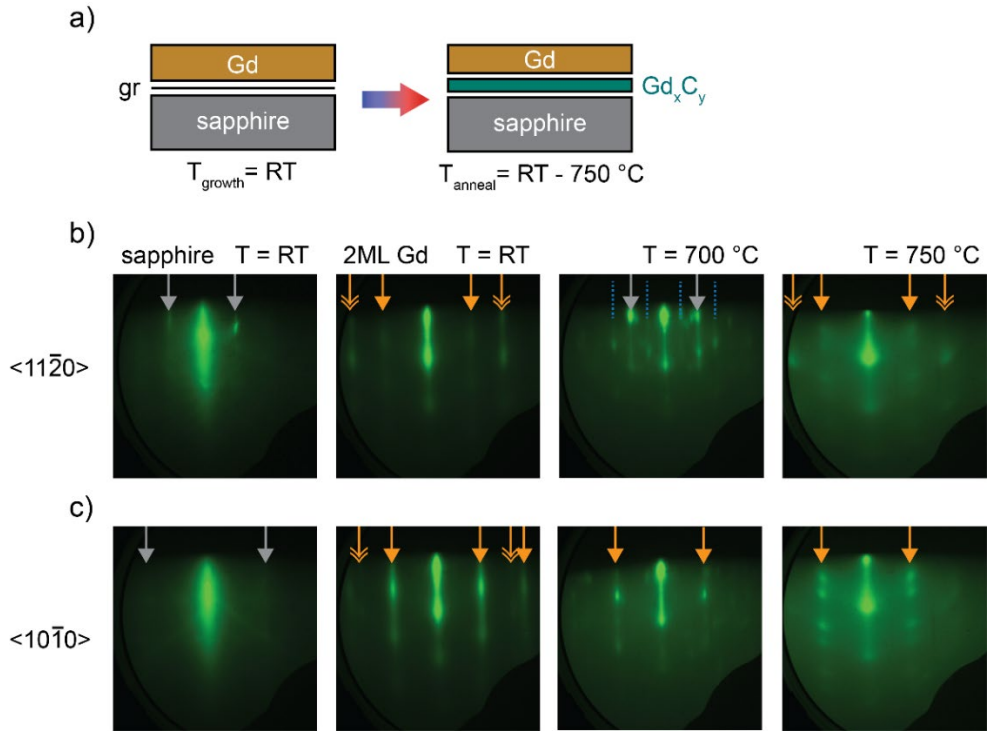

Figure 5.6 – Gadolinium growth on gr/sapphire. (a) Gd-carbide growth approach on gr/sapphire. (b-c) RHEED patterns along a <11$\bar{2}$0> (b) and <10$\bar{1}$0> (c) azimuth of gr/sapphire and 2ML Gd/gr/sapphire at room temperature and after annealing (gray arrows – sapphire, yellow arrows – Gd, yellow double arrow – 30° rotated Gd domain.

After annealing the samples at elevated temperatures (> 700 °C), we see distinct changes in the RHEED patterns. At 700 °C, we see a slight increase in diffuse scattering and an increase in the MBE chamber pressure like in the Gd/HOPG case. Additionally, we see the sapphire reflections appear once again, especially in the along the sapphire <11$\bar{2}$0> azimuthal direction (Figure 5.6b). This indicates that the continuous Gd film is de-wetting and Gd is desorbing from the

surface. Interestingly, additional half-order-like peaks (blue dashed lines) appear in this RHEED pattern which could be the result of an additional crystal phase appearing (Figure 5.6b). Additional spots at other Q-spacings can be observed in either direction, which is further evidence of de-wetting. After annealing up to 750 °C, we see the half-order features disappear. The patterns are no longer streaky and exhibit a more pronounced diffuse background (Fig. 5.6b). The presence of disconnected spots in either direction would suggest an island morphology due to the de-wetting of the film. The RHEED patterns indicate that the surface is clearly changing as a function of annealing, but it is difficult to say if any Gd_2C is forming. The main challenge is that Gd and Gd_2C have similar in-plane lattice parameters (3.635 Å and 3.639 Å, respectively), so it would not be possible to distinguish their reciprocal lattices in RHEED unless a unique surface reconstruction were to form.

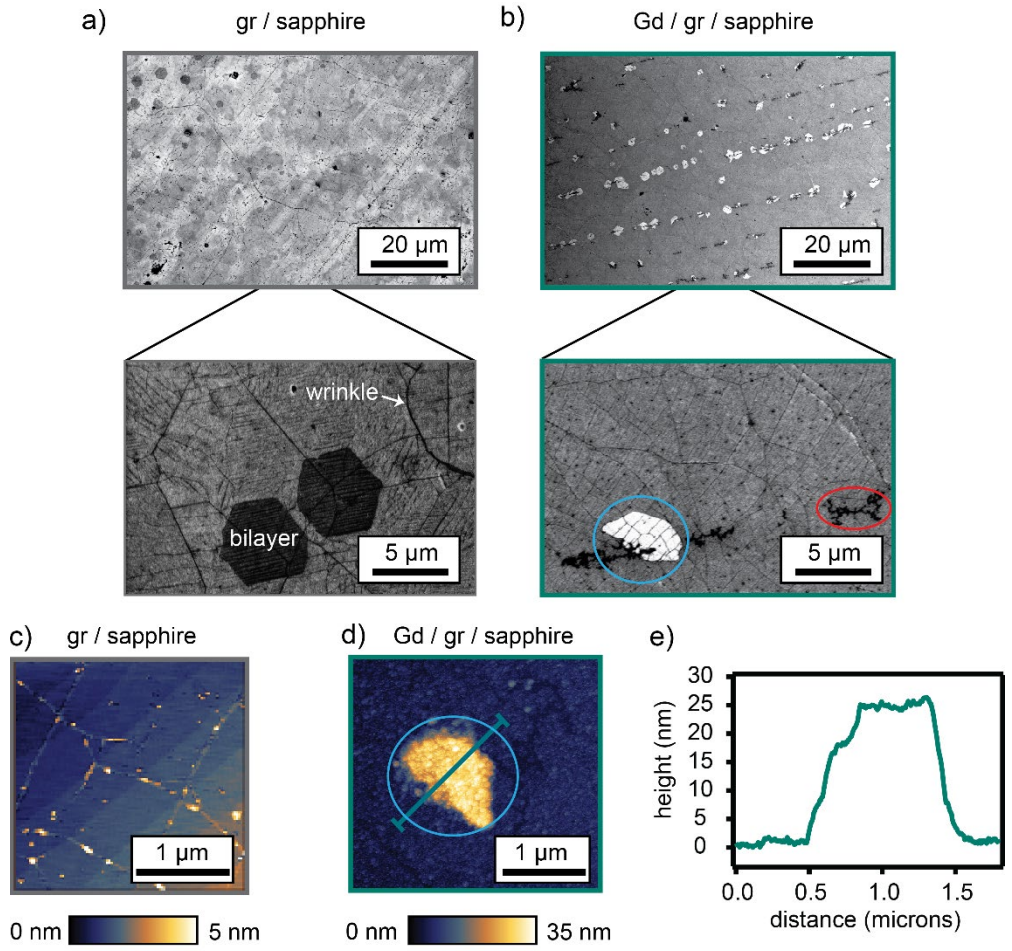

Figure 5.7 – (a) SEM images of transferred gr / sapphire after annealing at 600 °C in UHV. The zoomed-in image (bottom) shows graphene wrinkles and bilayers as well as faint outlines of the sapphire step terraces. (b) SEM images of Gd / gr / sapphire. Two distinct features can be seen after Gd growth, bright hexagons (blue circle) and dark, patchy lines (red circle). (c) AFM of clean, annealed gr / sapphire. (d) AFM of Gd / gr / sapphire. (e) Height profile (green line in (d) of a hexagon feature (blue circle).

The morphology of the film hints at the possibility of carbide formation. SEM images were taken of the gr/sapphire sample before growth (Figure 5.7a),

which show clean graphene with minimal tears. The dark hexagons that appear in the SEM images prior to growth are graphene bilayers. Some wrinkles and grain boundaries can also be seen (Fig. 5.7a). After Gd growth and annealing on the gr/sapphire substrate, we see disconnected "lines" that appear dark in the secondary electron SEM images (Fig 5.7b, circled red). The lines seem to be parallel to each other and aligned in the same direction. Another interesting feature is the bright hexagons in the images. These hexagons seem to resemble the graphene bilayers that displayed dark contrast prior to growth (Fig. 5.7a, circled blue). It is interesting, however, that the secondary electron contrast has changed dramatically. AFM images and height profiles of these hexagonal islands after growth reveal that they are approximately 25 nm thick (Fig 5.7d, e). This is surprising given that only 2ML of Gd was deposited. The native oxide of Gd upon exposure to oxygen is only a few nm thick, so this could only be explained by the de-wetting, adatom migration, and clustering at elevated annealing temperatures. Another possibility is a reaction between Gd and carbon. It is worth emphasizing that the disconnected dark "lines" and the tall hexagonal islands are not present on the gr/sapphire prior to growth, as seen by the SEM and AFM images (Fig. 5.7a, c).

We have presented here the characterization of Gd films grown on graphitic substrates and investigated via *in-situ* and *ex-situ* techniques the possibility of Gd_2C formation. X-ray diffraction suggests we have synthesized (105)-oriented Gd_2C on

HOPG; however, further work is required to understand why this orientation is favored. We have also established that due to the large surface diffusion lengths of metal atoms on graphene [90,91], annealing causes island formation. The islands observed after Gd synthesis and annealing on graphene appear faceted and are thicker than expected. *In-situ* XPS in addition to surface-sensitive chemical mapping such as Auger spectroscopy or photoemission electron microscopy would be ideal techniques to determine if Gd_2C has formed on graphene or on HOPG.

6 Applications of epitaxy on graphene-terminated substrates

This chapter is adapted from the following articles and ongoing work in the Kawasaki research group:

- P. J. Strohbeen, **S. Manzo**, V. Saraswat, K. Su, M. S. Arnold, and J. K. Kawasaki, *Quantifying Mn Diffusion through Transferred versus Directly Grown Graphene Barriers*, ACS Appl. Mater. Interfaces **13**, 42146 (2021).

  Author contribution: I conducted the graphene transfers and graphene characterization (SEM, Raman, AFM) and participated in discussions related to this work.

- D. Du, **S. Manzo**, C. Zhang, V. Saraswat, K. T. Genser, K. M. Rabe, P. M. Voyles, M. S. Arnold, and J. K. Kawasaki, *Epitaxy, Exfoliation, and Strain-Induced Magnetism in Rippled Heusler Membranes*, Nat. Commun. **12**, 1 (2021).

  Author contribution: I conducted the graphene transfers and graphene characterization (SEM, Raman, AFM). I also participated in discussions about different film exfoliation methods and ways to strain membranes.

6.1 Graphene as a solid-state diffusion barrier

Graphene has emerged as a highly promising material for solid-state diffusion barriers, exhibiting great potential for a wide range of applications. Due to the small "pore size" of graphene, it can successfully block diffusion for most gases [158,159]. Additionally, it has shown promise in metal-semiconductor contact structures despite its extreme thinness. On the other hand, conventional diffusion barriers are typically required to be tens of nanometers thick [160–163]. A single sheet of graphene can also passivate air-sensitive semiconductor and metallic surfaces for long periods of time [164–166]. One of the most significant advantages of graphene as a barrier material lies in its ability to support crystalline films above it. These films can be epitaxial to the underlying substrate, either through epitaxial lateral overgrowth at graphene pinholes [80,167,168] or via the phenomenon known as "remote epitaxy" [45,46,110,169,170]. It has been proposed that remote interactions originating from the substrate's lattice potential can permeate through graphene, effectively templating the growth of epitaxial films [1]. This intrinsic electronic transparency of graphene is highly valuable for spintronic applications, particularly for facilitating spin injection via tunneling [171].

Despite these remarkable properties, graphene cannot be synthesized on arbitrary substrates, meaning that it has to be transferred from its growth substrate

to the substrate of interest. Although there have been many advances in graphene transfer processes, they still represent a significant hurdle in the utility and applicability of graphene. Wet and dry graphene transfers require a polymer or metal handling layer that needs to be etched away. This step can leave interfacial metal contaminants and organic residues on the graphene [69,172–174]. Additionally, the transfer process itself can cause the fragile graphene layer to tear or wrinkle. With this reality in mind, it is important to understand how these defects and contaminants affect its barrier performance. In addition, it is highly desirable to know how transferred graphene compares to its pristine counterpart. Previous studies have qualitatively established that defects such as pinholes, grain boundaries and wrinkles negatively impact graphene's barrier performance [175–177]. However, a quantitative study that explores the effects of transfer-induced defects and elevated thin film growth temperatures is missing from the literature. Here we elucidate these effects by assessing the diffusivity of Mn grown on transferred and epitaxial graphene on semiconductor substrates via in-situ photoemission. Mn was chosen as the deposited material because of its relevance in spintronic applications, such as Mn-containing half-metallic ferromagnets NiMnSb and Co_2MnSi for spin injection into GaAs [178,179].

We perform this study with three graphene-substrate interfaces: 1) epitaxial graphene grown on Ge (001) 2) transferred graphene on Ge (001) 3) transferred

graphene on GaAs (001). The epitaxial graphene is grown on Ge substrates (AXT Inc.) via atmospheric-pressure CVD of CH_4, similar to the procedure described in Refs. [84,123] while the graphene used for transfers is grown on copper foil via CVD [44]. The graphene transfer is an adapted PMMA-assisted wet transfer method, similar to the one described in Ref. [80]. Prior to transferring the graphene, GaAs substrates are etched in 10% HCl and Ge substrates are etched in boiling water, to remove some of the native oxides. The samples were degreased in acetone and isopropanol baths and In-mounted onto molybdenum pucks. They were outgassed at 150 °C in a high-vacuum load lock ($p < 5 \times 10^{-8}$) and annealed up to 300 °C prior to Mn deposition to remove organic contaminants (labelled "pre-anneal"). The graphene-coated samples were then annealed up to 600 °C (labelled "post-anneal) to desorb native oxides underneath the graphene.

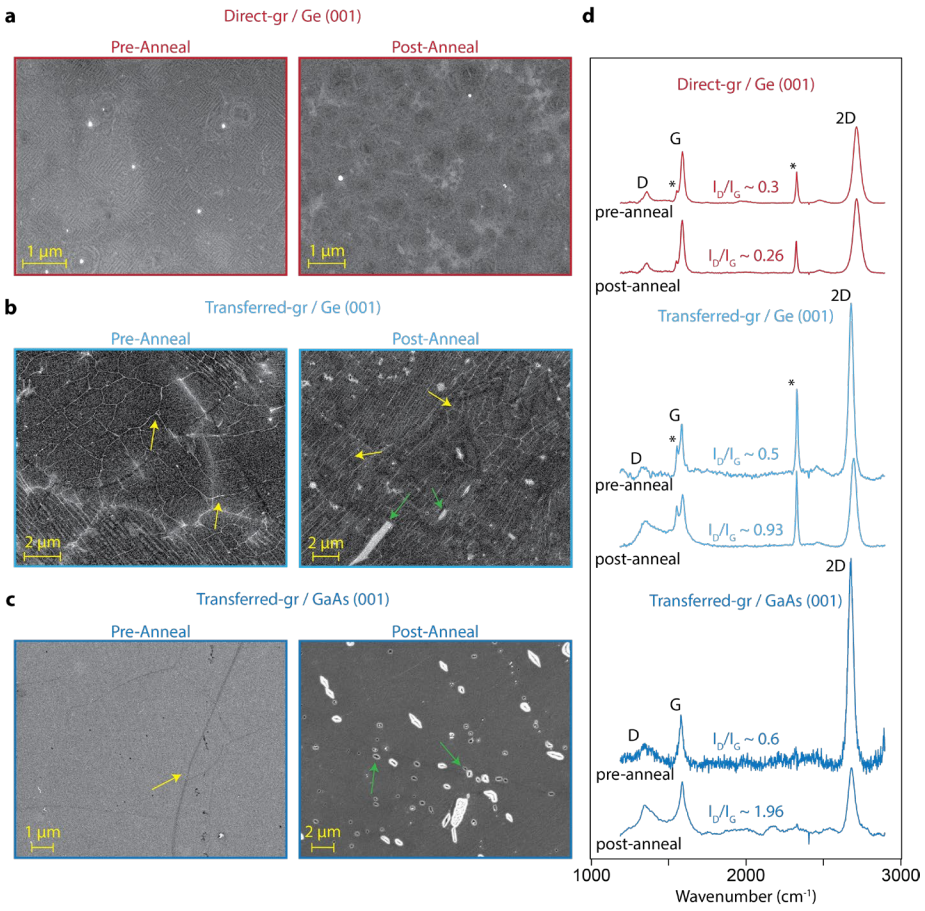

Figure 6.1 - Defects in directly grown vs layer-transferred graphene (figure and caption taken from Ref. [118]). “Preanneal” refers to samples lightly outgassed at 300 °C to remove adsorbates. “Postanneal” refers to samples annealed at 600 °C in ultrahigh vacuum to remove substrate native oxides. (a) SEM images for the directly grown graphene (gr) on Ge (001) substrates before and after annealing. (b) SEM images for the layer-transferred graphene on Ge (001). (c) SEM images for the layer-transferred graphene on GaAs (001). Yellow arrows indicate wrinkles and grain boundaries, and green arrows denote tears and holes in the graphene layer. (d) Raman spectra before and after annealing. The peaks marked by * are from the Ge substrate.

Annealing graphene introduces defects as seen by SEM and Raman spectroscopy, particularly for transferred graphene (Figure 6.1). The defect activated *D* band of graphene appears for all of the samples, even before the 600 °C anneal. This is not surprising for the transferred graphene, since small tears and wrinkles are inevitable consequences of the transfer process. After graphene growth, the Ge (001) surface experiences significant faceting (Figure 6.1a), which is a phenomenon that has been reported previously [125]. This faceting, along with native pinholes and grain boundaries can lead to the presence of a weak *D* peak in the Raman spectra [86,87]. The relatively broad *2D* band and lower *2D*:*G* intensity ratio (< 2) is also caused by the strong interaction between the graphene and the faceted Ge surface. The *D*:*G* integrated intensity ratios are also a good indicator of disorder in the graphene lattice [180]. The epitaxial graphene shows little change after annealing up to 600 °C. On the other hand, the transferred graphene on GaAs and Ge exhibit a stark increase of the *D:G* intensity ratio and a decrease of the *2D*:*G* ratio. Additionally, SEM images after annealing reveal a substantial increase in tears and other defects in the transferred graphene. In our previous work, we demonstrated that these annealing-induced defects arise from the trapped native semiconductor oxide desorbing through the graphene [80]. This does not occur for the graphene directly grown on Ge, because the graphene acts as an oxidation barrier after it nucleates and coalesces on the Ge surface [164].

After establishing the effects of transferring and annealing the graphene, we study the diffusion of Mn on graphene via in-situ photoemission. After the pre-growth anneal, ~ 24 Å (1.64×10^{16} atoms/cm^2) of Mn were deposited at room temperature. The samples were then transferred from our MBE growth chamber to the XPS analysis chamber ($p < 3\times 10^{-10}$ Torr) through an ultra-high vacuum manifold. XPS measurements were conducted using a nonmonochromatic Omicron DAR-400 dual-anode X-ray source (Al Kα, hν = 1486.6 eV) and an Omicron EA125 hemispherical analyzer. The total energy resolution of the analyzer in the experimental configuration was measured to be 1.08 eV using an Au standard. To promote Mn diffusion into the substrate, each sample was annealed from room temperature up to 500 °C in 100 °C increments. The anneal temperature was measured using a thermocouple attached to the sample manipulator and calibrated to the In melting point and As desorption temperature of As-capped GaAs.

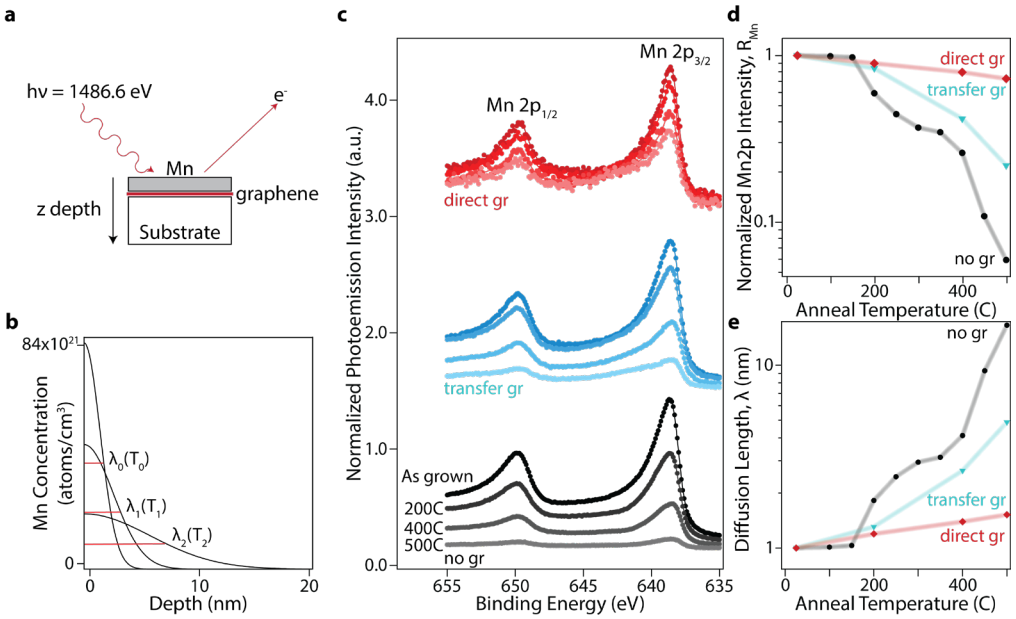

Figure 6.2 – In situ photoemission measurements of Mn on graphene(gr)/Ge (figure and caption taken from Ref. [118]). (a) Schematic layer structure and measurement geometry. (b) Half Gaussian composition profiles as a function of depth from the surface. We use this model to extract diffusion length λ. (c) Mn 2p core-level spectra for Mn thin films grown directly on bare Ge (black), transferred graphene/Ge (blue), and directly grown graphene on Ge (red) at increasing annealing temperatures using an Al Kα source (hν = 1486.6 eV). Samples were rapidly heated to the anneal temperature, held for 5 min, rapidly cooled, and measured at room temperature. Symbols are experimental data and curves are fits to a Doniach–Sunjic lineshape. (d) Normalized Mn intensity ratio, tracking the relative change in the Mn surface composition as a function of anneal temperature T. For substrate normalization, we use sub = Ge 3p. (e) Calculated Mn diffusion lengths λ at each anneal temperature.

Figure 6.2 (c) shows the evolution of the Mn *2p1/2* and *2p3/2* core levels for Ge substrates, with and without graphene, as a function of annealing. All spectra have been normalized to the Ge *3p* core level to remove the effect of experimental

variations. We fit the Mn *2p* and Ge *3p* core levels to Doniach–Sunjic [181] and Voight lineshapes, respectively, and plot the normalized Mn *2p* intensity ($R_{Mn} = \frac{(I_{Mn}/I_{Ge})_T}{(I_{Mn}/I_{Ge})_0}$) as a function of temperature (Figure 6.2d). This normalization procedure removes the effects of instrumental sensitivity, alignment, and photoemission cross section. For the Mn grown on bare Ge, we see a sharp decrease in the surface Mn concentration starting at 150 °C and a further decrease at higher temperatures (R_{Mn} ~ 0.05 at 500 °C). This is due to Mn reacting and diffusing into the substrate. On the other hand, the decay in the Mn surface concentration is suppressed by both transferred and directly grown graphene. The directly grown graphene acts as an excellent diffusion barrier, with R_{Mn} decreasing only to 0.7. As expected from the Raman spectroscopy and SEM images, the more defective transferred graphene exhibits worse barrier performance, with an R_{Mn} ~ 0.2.

We can then extract the temperature-dependent diffusion length based on the normalized Mn *2p* intensity (R_{Mn}) and Mn composition profiles. For a thin Mn film on a semi-infinite substrate, the solution to the diffusion equation is a half-gaussian composition profile. Using the known initial conditions and areal density of Mn we can calculate the initial diffusion length. Then, by rewriting the composition profiles in terms of areal density, we can use the known expression for the intensity of a core level to calculate the expected intensity ratios for Mn *2p* and Ge *3p* as a function of the diffusion length. We can then compute R_{Mn}, which will

be uniquely defined by the diffusion length. Lastly, we can use the experimentally derived R_{Mn} values to extract a diffusion length for each annealing step. More details on the calculation of the diffusion length are found in Ref [118]. Figure 6.2 (b) clearly shows that the diffusion length of Mn is much higher than on graphene, with the directly grown graphene suppressing the diffusion length by a factor of 11 and the transferred graphene by a factor of 3.5 at 500 °C. We also performed a photoemission study on GaAs (001), which showed that transferred graphene suppresses diffusion into GaAs. The graphene barrier performance on GaAs is slightly better than on Ge ($R_{mn} \sim 0.7$ vs $R_{mn} \sim 0.2$ at 500 °C), which we attribute to unintended, stochastic differences in the graphene quality after transferring.

Using the extracted diffusion lengths, we can calculate the diffusivity as a function of temperature. An Arrhenius fit allows us to calculate the activation energies and diffusivity prefactors for each sample. Further details on how this was done can be found in Ref. Remarkably, we find that at 500 °C the diffusivity of Mn is 1000 times lower on directly grown gr/Ge than on bare Ge. The decrease in diffusivity is not as large for transferred graphene/Ge, being smaller by a factor of 10 compared to bare Ge. The experimentally determined activation energy for Mn diffusing into bare Ge and GaAs substrates (E_a = 0.8 eV) agrees well with previously reported experiments and DFT simulations for Mn interstitial diffusion into GaAs (E_a = 0.7-0.8 eV) [182]. Conversely, the activation energy for the

graphene-coated substrates is significantly lower: 0.1 eV for directly grown graphene on Ge and 0.2–0.5 eV for transferred graphene on GaAs and Ge. Since the pore size of graphene is so small (0.7 Å compared to Mn atomic radius of 16.1 Å), we rule out transverse diffusion, which has a very high activation energy of E_a ~ 12 eV [183]. Therefore, it is likely that diffusion through graphene is mediated by defects. At high temperatures (> 200 °C), we speculate that the activation energy is lower on graphene-terminated substrates because diffusion is catalyzed by the defects, which are known to be highly reactive sites [98]. It is unclear why the activation energy is lower at lower temperatures, but a possible reason could be a convolution of lateral diffusion of Mn adatoms to the defective sites followed by diffusion into the substrate. More experiments with lateral and depth resolution are needed to explore this result.

Despite the low activation energy barrier for diffusion on graphene, we see a suppressed diffusivity because of the reduced diffusivity prefactor D_o. We interpret this factor as an "attempt rate" for diffusion. For Mn on bare substrates, the attempt rate is high (10^{-11} – 10^{-12} cm^2/s) because there are many sites available for interstitial diffusion. On the other hand, the graphene-terminated surfaces are mostly inert, except for the defects. In other words, the graphene defect density should correlate with the attempt rate, which is what our results indicate. The layer-transferred graphene on Ge has a higher defect density as quantified by our Raman

and SEM and the attempt rate is higher (10–13 cm2/s) than that for directly grown graphene (10–17 cm2/s).

Our results show that transferred and directly grown graphene successfully block Mn diffusion on semiconductor substrates. The directly grown graphene exhibits superior performance due to lower defect density, evidenced by the SEM and Raman spectroscopy. Although transferred graphene does suppress diffusion, it will be crucial to develop methods to synthesize graphene on functional semiconductor substrates. Several promising approaches are currently under investigation like plasma-enhanced CVD [184–186] and the use of liquid precursors [187,188] to reduce the graphene synthesis temperature. These low-temperature growth approaches could pave the way for graphene growth directly on GaAs and other important III-V semiconductors.

6.2 Strain-induced magnetism and superconductivity in rippled Heusler membranes enabled by a graphene interlayer

Thin crystalline membranes have emerged as powerful platforms for flexible devices and have the unique capability of modulating their materials properties through strain and strain gradients [189–195]. Strain engineering of epitaxial films, which is determined by lattice mismatch, is uniform and can only accommodate up to 3% strain before plastic deformation. On the other hand, membranes can tolerate much higher strains and the strain can be applied dynamically, anisotropically and in gradient form (Figure 6.3a). Recent demonstrations have shown that ultra-thin oxide membranes can be strained continuously and in arbitrary directions, while being able to access extreme strains of up to 8% [192]. Furthermore, crystalline membranes supported on flexible polymers can be deformed in various geometries and be easily bent, twisted, and rippled. This would be impossible to do on a clamped epitaxial thin film.

Strained membranes are particularly promising for tuning ferroic properties in materials. The coupling of magnetism and strain is well known (i.e., piezomagnetism and magnetostriction) and has been studied previously for bulk and thin film samples [196–199]. Additionally, novel phenomena have also been discovered, such as the continuous tuning of antiferromagnetic spins in $BiFeO_3$ via

strain due to a competition between Dzyaloshinskii–Moriya interactions and single-ion magnetic anisotropy [200]. On the other hand, the effect of strain gradients on magnetism (i.e., flexomagnetism) has not been demonstrated due to the difficulty in engineering and synthesizing strain gradients in epitaxial heterostructures. Crystalline membranes are also challenging to make, and most methods rely on the selective-etch chemistries of sacrificial layers [192,193,201]. This approach presents several constraints. The film must be chemically resistant to the selective etchant, and more importantly, the sacrificial layer must be a substrate that is compatible with epitaxy. Here, we utilize a different approach that involves growing films grown on graphene-terminated substrates. The weak van der Waals interface enables easy exfoliation, while growth mechanisms on graphene such as pinhole-seeded epitaxy [80], remote epitaxy [83] or van der Waals epitaxy, ensure that the resulting film is crystalline. We focus on the exfoliation and characterization of two Heusler membranes, namely GdPtSb and GdAuGe.

Our results indicate that rippled GdPtSb membranes are flexomagnetic, with strong strain gradient-dependent magnetization dictated by the aspect ratio of the ripples. The GdPtSb films are grown via MBE on graphene-terminated c-sapphire substrates. The graphene is grown via CVD on copper foils and transferred using an adapted PMMA-assisted wet transfer technique described in Ref [44]. Prior to GdPtSb growth, the graphene/sapphire substrates are outgassed (150 °C)

to remove water and annealed up to 700 °C in UHV ($p < 5 \times 10^{-9}$ Torr) to desorb organic contaminants. Further details on the growth and structural characterization, which includes RHEED and X-ray diffraction, can be found in Ref [44]. The film is decoupled from the graphene-interlayer by placing it film-side down onto melted wax (Crystalbond) on a glass slide. The Crystalbond is then cooled below its glass-transition temperature and the whole film/glass slide stack is gently dropped from about 4ft onto a clean surface. The impact of the fall results in the detachment of the graphene/sapphire substrate, leaving the film behind (Figure 6.3c). X-ray diffraction after exfoliation confirms that the membrane is crystalline and undamaged at the macroscopic scale (Fig. 6.3b). We impart strain and strain gradients by first stamping tape on the membrane/Crystalbond/glass slide stack while it is being heated on a hot plate. When the Crystalbond melts, the membrane is released from the glass slide and is adhered to the tape. As the tape and residual Crystalbond on the surface cool, the tape relaxes and contracts which creates a sinusoidal ripple structure on the membrane. We can tune the ripple aspect ratio (height/width) by selecting tapes with different thermal expansion coefficients (Fig. 6.3f-h).

We then characterize the magnetic properties of our membranes and compare them to a clamped GdPtSb film. We find that the strain and/or strain gradients caused by the ripples induce magnetic ordering, transforming

antiferromagnetic GdPtSb films into ferro- (or ferri-) magnetic rippled membranes at room temperature. Figure 6.3 (d) shows the magnetization M versus applied magnetic field H for a relaxed GdPtSb film on sapphire (green), a membrane on stiff polyimide (blue) and a membrane on stretchy polyurethane (red). At room temperature, the unstrained, relaxed film shows a weak linear magnetization dependence with applied field. Magnetic susceptibility measurements show that GdPtSb films become antiferromagnetic at a Néel temperature of 12 K (details found in Ref. [44]). Remarkably, the rippled membranes show spontaneous magnetization and hysteresis loops which are a sign of ferro- or ferrimagnetism (Fig 6.3d). Moreover, there is a strong dependence between the saturation magnetization and the ripple aspect ratio (height/width), as seen in Figure 6.3e). The polyurethane tape, which has a larger thermal expansion coefficient than polyimide (polyimide $\alpha = 34 \times 10^{-6}$ K^{-1}, polyurethane $\alpha = 57 \times 10^{-6}$ K^{-1}), exhibits the largest magnetization and has the largest aspect ratio. These results suggest that the magnetic ordering is ripple-induced, which we attribute to increased strain and/or strain gradients for large aspect ratios.

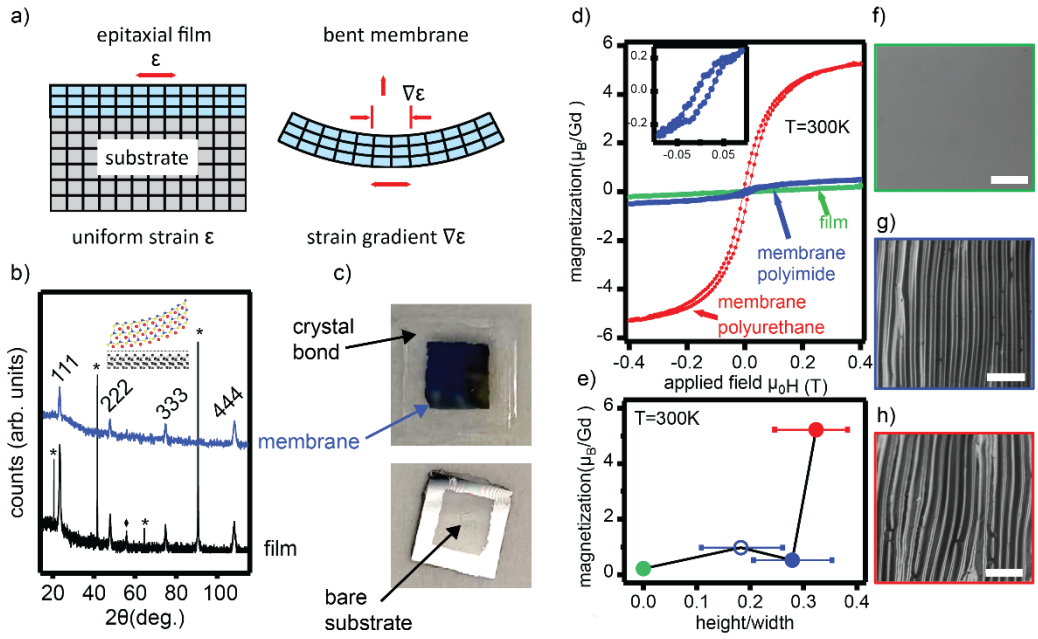

Figure 6.3 – Exfoliation and flexomagnetism of rippled GdPtSb membranes (Figure and caption adapted from Ref. [44]). a) Schematic showing the modes of strain accessible to epitaxial films vs free-standing membranes. Piezomagnetism and magnetostriction are magnetic responses to uniform strain (ε) and are accessible in thin films. Flexomagnetism is the response to strain gradients (∇ε) and is accessible in ultrathin membranes. b) XRD 2θ-ω (Cu Kα) scans before (black) and after exfoliation (blue). The sapphire substrate's reflections are marked by asterisks. In addition to the 111-type reflections, a small 004 reflection is observed and marked by a diamond. c) Photograph of the exfoliated membrane (top) and substrate (bottom) utilizing crystal bond. The regions on the substrate that are still covered by film after exfoliation are regions without graphene. d) Magnetization of GdPtSb film (green), GdPtSb membrane supported on polyimide (blue) and on polyurethane (red). e) Room-temperature magnetization at 0.4 Tesla versus ripple aspect ratio. Relaxed film (green), rippled membrane on polyimide (blue), rippled membrane on polyurethane (red). The error bar represents the distribution of aspect ratio over several regions. f-h) Optical micrographs of a relaxed film (f, green), a rippled membrane on polyimide (g, blue) and of a rippled membrane on polyurethane (h, red). The scale bar is 100 μm.

We have successfully extended the use of strained membranes to another materials system, namely GdAuGe (hexagonal $P6_3mc$). Smooth, single-crystalline GdAuGe films can be successfully synthesized on graphene directly grown on Ge (111). The gr/Ge (111) system offers a simpler platform to produce membranes since there are no transfer-induced defects or contaminants that result in poor exfoliation yields. The GdAuGe films were exfoliated onto pre-stretched polyurethane tape adhered on a glass slide. By detaching the glass slide from the tape, it is allowed to relax thus generating ripples. This method has the advantage of leaving an exposed GdAuGe surface which can be probed with surface sensitive measurements. The ripple period and amplitude are measured via optical microscopy and AFM. The radius of curvature can then be calculated by fitting the AFM ripple height profile to a sinusoidal function. This can then be used to find the strain and strain gradient along the sinusoidal path. The maximum strain gradient is localized at the peaks and throughs of the sinusoidal ripples. The magnetic ordering of GdAuGe membranes was characterized using SQUID magnetometry.

We observe several magnetic phases in GdAuGe membranes as a function of strain gradient. By tuning the ripple amplitude and period we can access four states in GdAuGe: paramagnetic, ferro/ferrimagnetic, antiferromagnetic and a

superconducting state (Fig 6.4a). Relaxed GdAuGe exhibits a single magnetic transition that corresponds to antiferromagnetic ordering at T_N = 14 K (Fig. 6.4d).

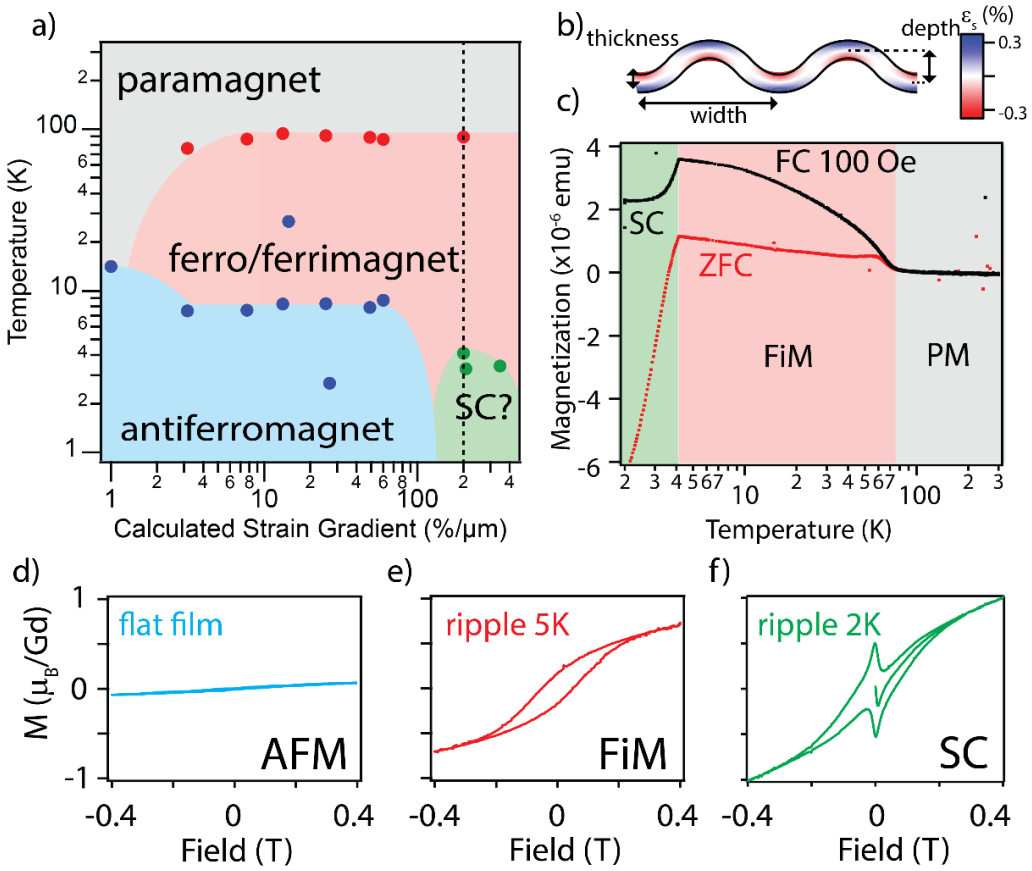

Figure 6.4 – Strain-induced magnetism and superconductivity in GdAuGe. (a) Magnetic phase diagram of rippled GdAuGe membranes depicting antiferromagnetic ordering (blue), ferro/ferrimagnetic ordering (red), and superconducting critical (green) temperatures characterized by SQUID magnetometry. (b) Cartoon of rippled GdAuGe showing local tensile (blue) and compressive (red) strains. (c) Zero field cooling (red) and 100Oe field cooling (black) magnetization v. temperature scans of a rippled GdAuGe membrane, corresponding to the dashed line in a). (d-f) Magnetization v. applied field for an unexfoliated GdAuGe film d), rippled membrane above e) and below f) superconducting T_c.

Rippled membranes subjected to strain gradients from 3 - 60 %/μm however, exhibit two magnetic transitions; at T = 75-94 K we observe a ferro/ferrimagnetic transition and below T = 7.5-8.8 K we see antiferromagnetic ordering. This remarkable result is similar to the flexomagnetic response in GdPtSb membranes [44]. At extreme strains/strain gradients (>200%/μm) we still see ferro/ferrimagnetic ordering from T = 4-8 K (Fig. 6.4e). At temperatures below 4 K we can observe the Meissner effect, a unique characteristic of superconductivity (Fig 6.4f). In total, we have been able to produce three samples with relatively homogeneous ripple aspect ratios that exhibit superconducting behavior, as determined by SQUID. The calculated maximum strain gradients for these are 200%/μm, 207%/μm, and 346%/μm and exhibit critical temperatures of 4.1K, 3.3K, and 3.4K respectively. The presence of antiferromagnetic ordering alongside superconductivity in the magnetic phase diagram of GdAuGe (Fig. 6.4a) shows a striking resemblance to that of unconventional superconductors [202–204].

In summary, we have shown that graphene enables the production of ultra-thin Heusler membranes which can be subjected to extreme strains and /or strain gradients. As a result, we can tune the magnetic ordering of Heusler membranes, which would be impossible to do via conventional heteroepitaxial mismatch strain. Further work is required to elucidate the origins of superconductivity and

magnetism in GdAuGe membranes. This represents a novel platform to study the rich physics of many Heusler alloys which can be grown on graphene.

7 Conclusions and future directions

To conclude, this dissertation encompasses my work on understanding growth on graphene-terminated surfaces. We have studied nucleation on both clean and defective graphene/substrate interfaces to determine whether an intrinsic remote mechanism is possible. We found that transferred graphene on GaAs and GaSb becomes highly defective after annealing and these chemically reactive defects act as nucleation sites that lead to overgrowth and coalescence. In addition, single-crystalline GaSb films grown on gr/GaSb (001) could be readily exfoliated, thus demonstrating that a pinhole-seeded mechanism could replicate the features of remote epitaxy.

The pinhole-seeded epitaxy mechanism motivated our nucleation studies on the cleaner gr/Ge (111) surface. We deposited GaAs, performed *ex-situ* atomic force microscopy measurements, and observed nucleation at the top and bottom of the Ge step edges, at wrinkles, and in some cases at unintentional graphene-openings. Step-edges are more likely to transmit lattice potential fluctuations from the Ge substrate than wrinkles, so we speculate that they could be a pathway to achieve epitaxy on graphene via an *intrinsic* mechanism that is not reliant on defect-seeded nucleation. Further *in*-situ surface-sensitive measurements, such as scanning tunneling microscopy and photoemission electron microscopy, at the

early stages of growth are required to determine the crystallographic orientation and chemical structure of nucleation at step edges. Furthermore, we plan on performing growths on graphene-covered vicinal substrates, which offer more control over the step-edge density. Performing these nucleation studies on other clean graphene/substrate interfaces such as gr/SiC and gr/sapphire are also of interest, to study the influence of substrate polarity on the growth mechanism.

Another promising growth approach that involves graphene is epitaxial lateral overgrowth utilizing graphene masks. We show that we can obtain excellent nucleation selectivity on partial-coverage gr/Ge (111) and full coalescence within 400 nm. We comment on the optimized growth conditions to obtain smooth GaAs films without a pyramidal hillock morphology. Future work in this area will involve experimentally measuring the diffusion length of GaAs on graphene through *in-situ* scanning tunneling microscopy. These measurements would allow us to quantify the relative importance of surface diffusion on graphene and to optimize the graphene feature size to match the characteristic diffusion length. This work could be extended to highly mismatched systems in the future, such as GaSb on patterned gr/Ge (111), to study how effective this method is at reducing misfit dislocations.

We also demonstrate some of the advantages of growing on graphene-terminated substrates. Both transferred and directly grown graphene are excellent diffusion barriers and pave the way to grow intermetallic Heusler alloys on

graphene for spintronic applications. Lastly, we show that graphene interlayers enable the exfoliation of single-crystalline membranes which can be rippled to access strain and strain gradients that give rise to novel magnetic and superconducting phase transitions. Optimization of the membrane exfoliation process and more reliable methods to impart strain are currently being developed to map out the full strain/strain-gradient dependent phase diagram for GdAuGe membranes. We are also designing processes to create lithographic metal contacts on rippled membranes using molybdenum shadow masks to perform transport measurements that will give more insights into the apparent superconducting state in strained GdAuGe.

Overall, this dissertation has shed light into the mechanisms of epitaxy on graphene-terminated surfaces and demonstrated that remote epitaxy is not so simple after all. Once more *in-situ* growth experiments are conducted, we believe we can take full advantage of the benefits of growing on graphene and extend it to study other materials systems that exhibit intriguing electronic, optical, and magnetic properties, such as the rare-earth half-Heusler bismuthides and their membranes.

A Appendix: supplementary information for chapter 3

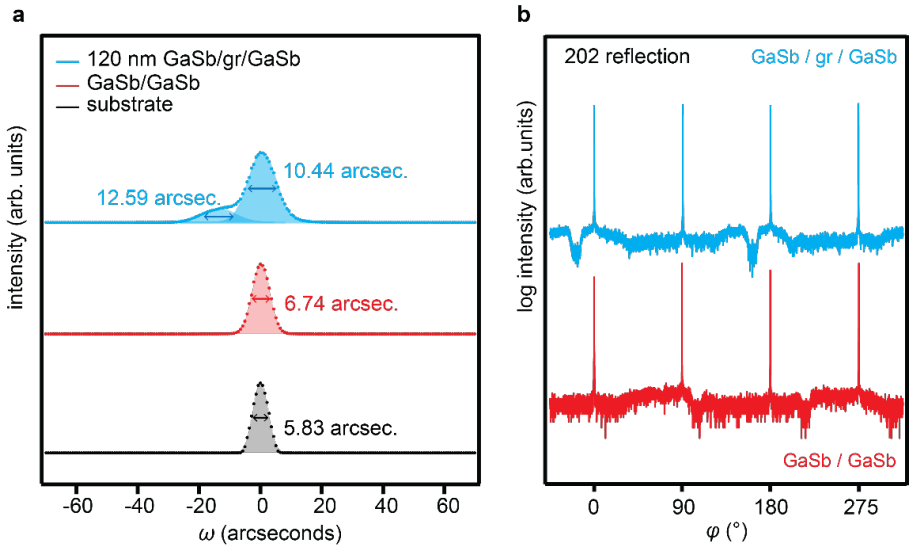

Figure A.1 - Extended x-ray diffraction of GaSb grown on graphene and on a bare GaSb substrate. (a) Rocking curve of the 004 reflection for GaSb on graphene/GaSb (001), GaSb on GaSb (001), and a bare GaSb (001) substrate. (b) Pole figure φ scans of the 202 reflection, showing the expected 4-fold symmetry of an epitaxial GaSb film.

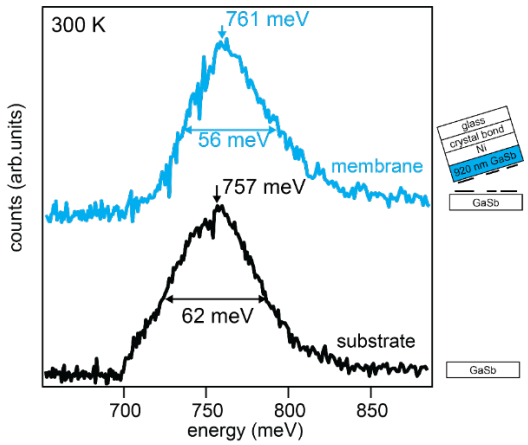

Figure A.2 – Normalized room temperature photoluminescence (PL) spectroscopy of a 920 nm thick exfoliated GaSb membrane (blue), compared to a bare GaSb (001) substrate (black).} The peaks at 761 meV (membrane) and 757 meV (substrate) correspond to the direct bandgap transition of GaSb. The membrane is slightly redshifted compared to a substrate, which we attribute to strain imparted by the Ni stressor layer. Both membrane and substrate peaks exhibit similar full width at half maximum of ~ 60 meV.

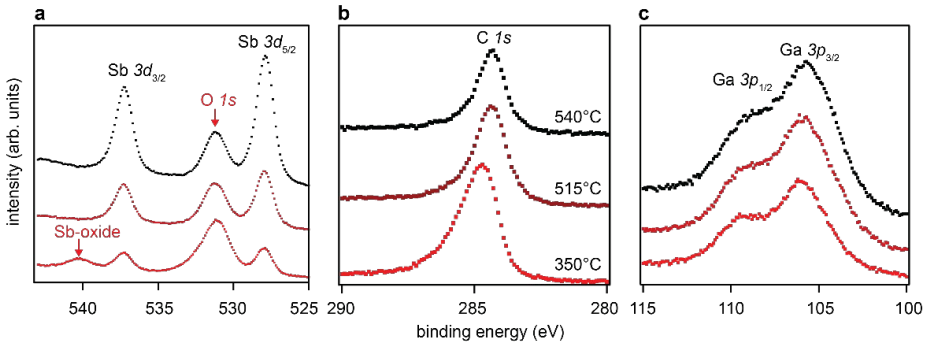

Figure A.3 – Extended in-situ photoemission spectra of graphene on GaSb (001) tracking the native oxide desorption as a function of annealing. (a) Sb 3d and O 1s core levels. The Sb-oxide intensity goes to zero after the 515 °C anneal, but residual atomic O 1s remains. (b) C 1s. After the 515 °C anneal we observe a shift in the C 1s core level towards lower binding energy, which we attribute to de-oxidation. (c) Ga 3p. Ga-oxide components are not resolved in these spectra.

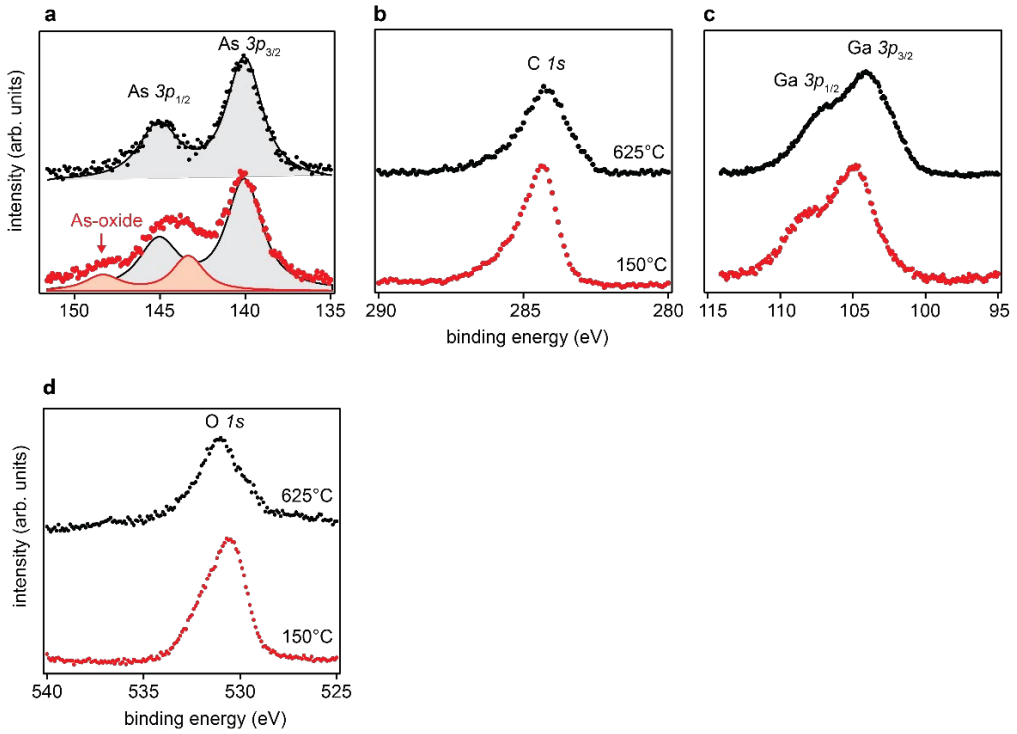

Figure A.4 – Native oxide desorption from a graphene/GaAs (001) sample. The CVD-grown graphene was wet transferred to GaAs (001) after an HCl etch to remove some of the GaAs native oxides. (a) Photoemission spectra of the As 3p core level. Arsenic (As) oxides are detected after the 150 °C anneal (red curve) and are desorbed after the 625 °C anneal (black curve). (b) There is a corresponding change in the C 1s lineshape. (c) Ga 3p core level. (d) O 1s core level.

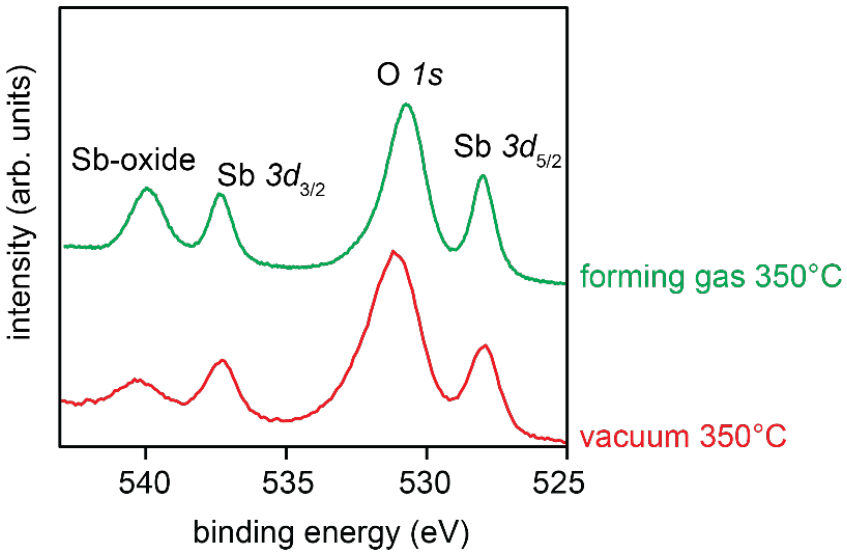

Figure A.5 – Forming gas annealing of graphene/GaSb (001). Photoemission spectra of forming gas annealed graphene/GaSb (001) (green curve) compared to vacuum annealed graphene/GaSb (001) (red curve). Both spectra show significant Sb-oxides and O 1s. The forming gas annealed sample was annealed in a tube furnace at 350 °C for two hours and then transferred through air to the XPS system. The vacuum annealed sample was annealed in ultrahigh vacuum in the XPS chamber, and thus did not get exposed to air after the anneal.

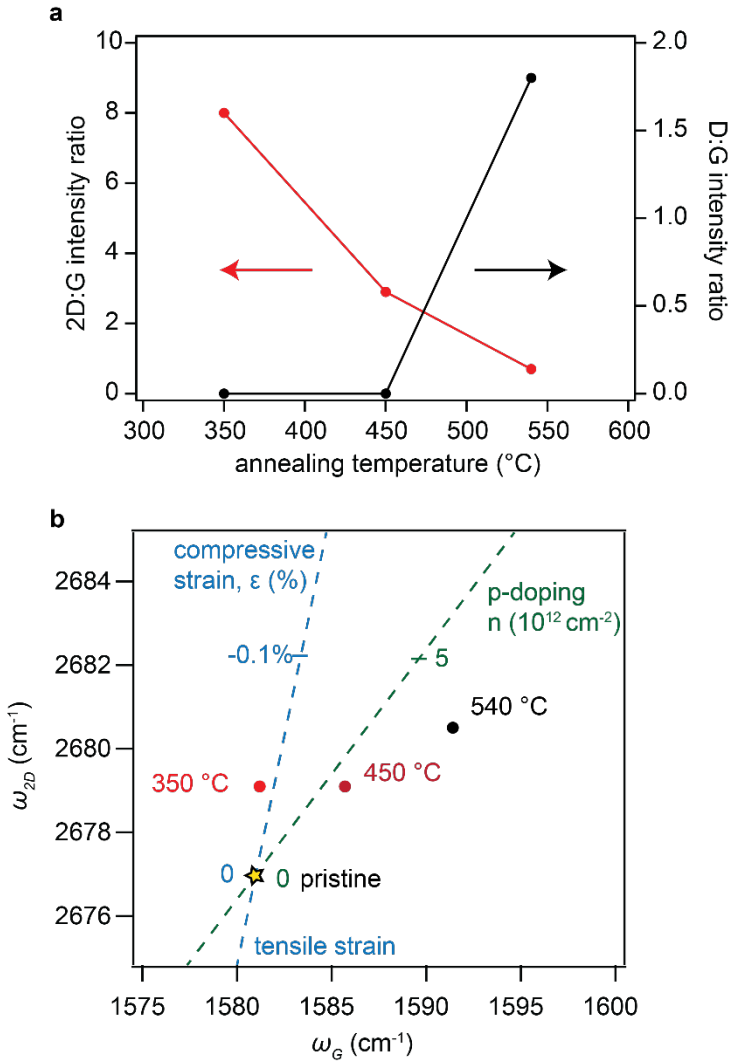

Figure A.6 – Extended Raman analysis of transferred graphene on GaSb (001), through the oxide desorption. (a) *2D:G* and *D:G* integrated intensity ratios as a function of anneal temperature. Above 450 °C, which was the onset of native oxide desorption from XPS and AFM measurements, the *D:G* ratio increases (black curve), indicative of graphene defects. The *2D:G* (red curve) decreases continuously across the range of anneal temperatures. (b) *2D* versus *G* frequency, tracking changes in strain and doping in the graphene with increasing anneal temperature. The dependence of doping and strain on *G* and *2D* frequency (dotted lines) is from Ref. [138].

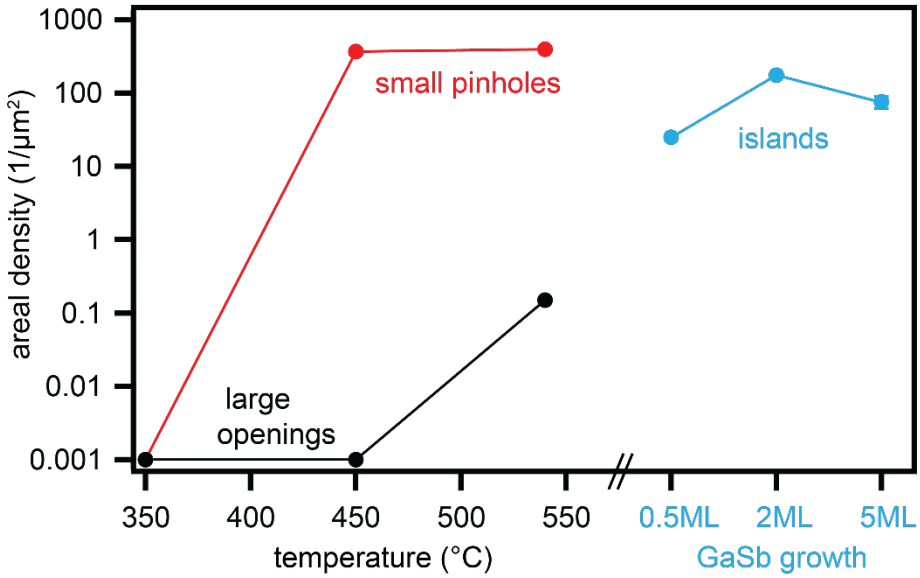

Figure A.7 – Areal density of pinholes and nucleated GaSb islands. The density of small pinholes (diameter < 300 nm) was extracted from AFM measurements. The density of larger openings (diameter > 300 nm) was extracted from SEM. The strong correspondence between density of islands and density of pinholes is consistent with GaSb nucleation at the pinholes. From 2 ML to 5 ML of GaSb growth, the island density decreases due to the beginning of coalescence.

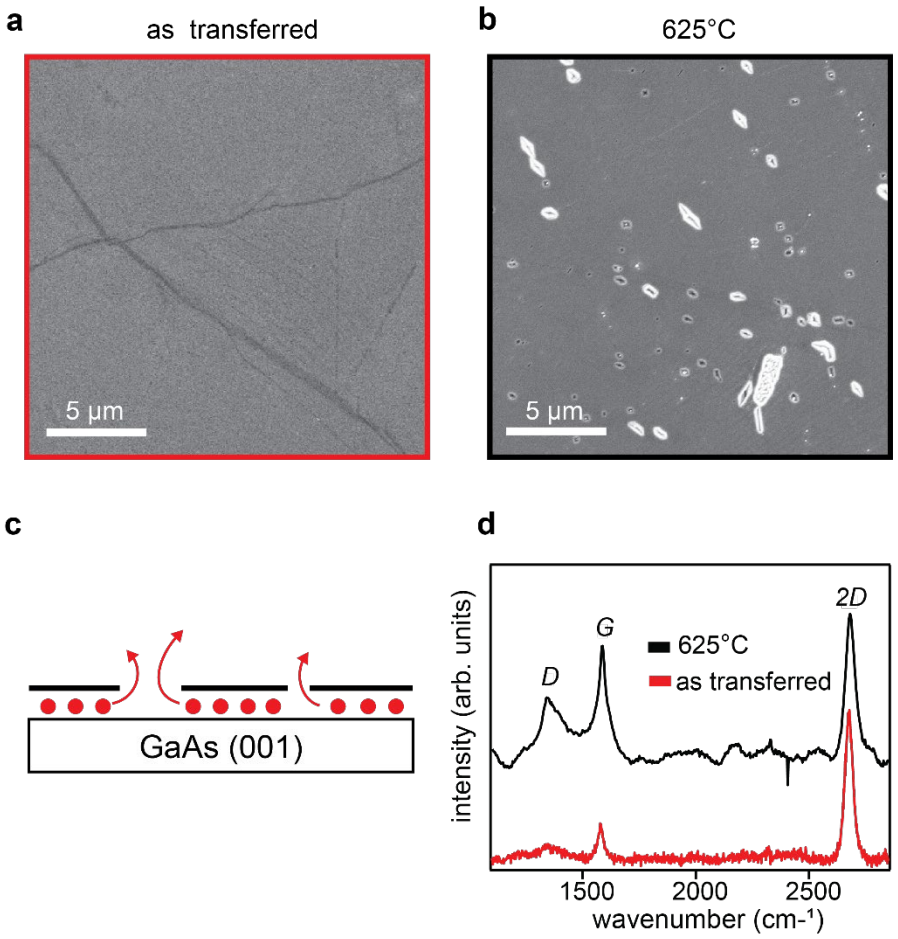

Figure A.8 – Pinholes formed in wet transferred graphene on GaAs (001). (a) SEM image of graphene transferred to GaAs (001), before annealing. No pinholes are observed. The dark lines are wrinkles. (b) SEM image after annealing above the native oxide desorption temperature (625 °C for 2 hours). Pinholes are observed. (c) Cartoon of the native oxide desorption. (d) Raman spectra before and after annealing above the native oxide desorption. We observed an increased Raman *D* peak after native oxide desorption (625 °C).

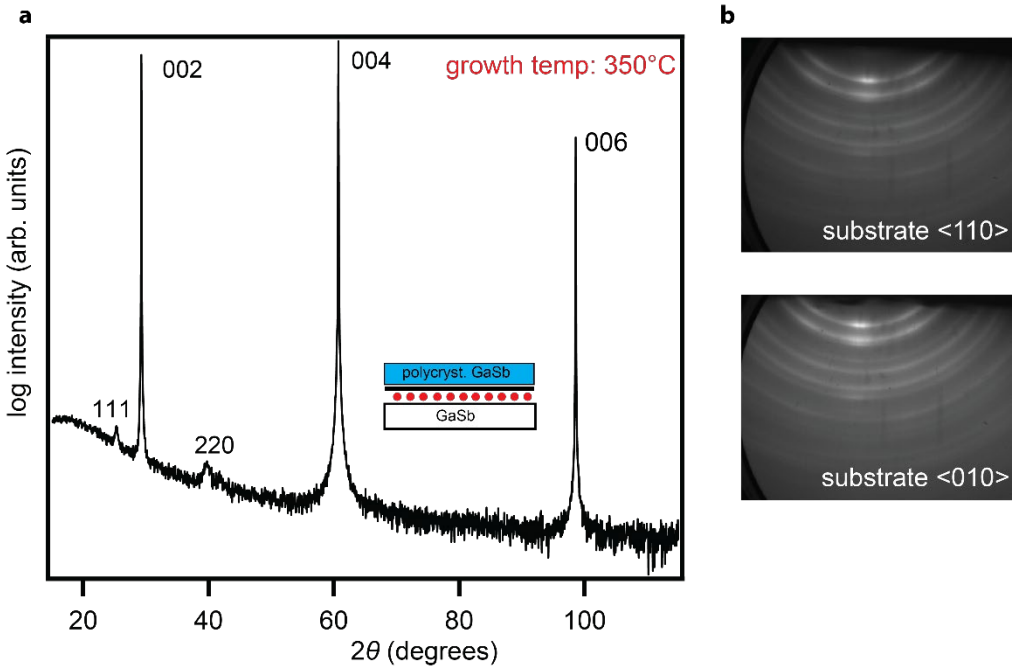

Figure A.9 – Electron and x-ray diffraction of GaSb grown on graphene-terminated GaSb below the native oxide desorption temperature. (a) At a growth temperature of 350 °C, holes in the graphene will not form, which means that pinhole-seeded epitaxy is not possible. As a result, a polycrystalline film is grown as evidenced by the presence of 111 and 220 reflections in the ω-2θ scan. (b) The rings present in the RHEED images of both <110> and <010> substrate orientations indicate that the film is polycrystalline.

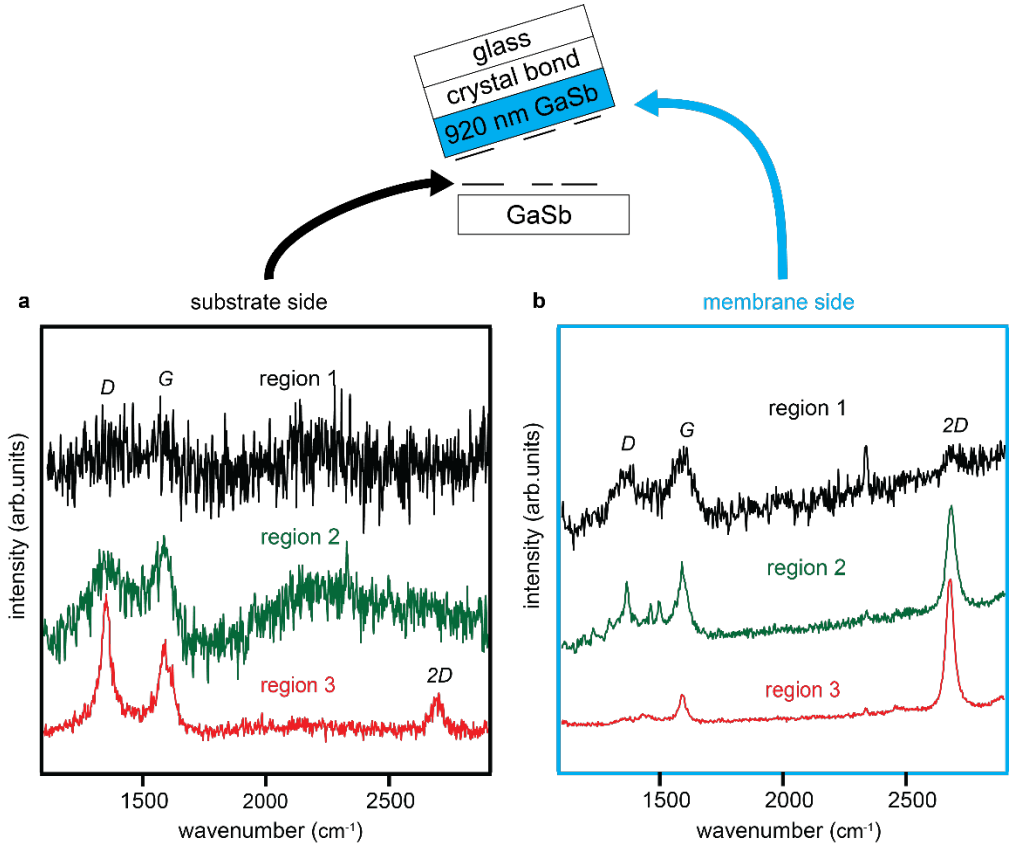

Figure A.10 – Raman spectroscopy of graphene on membrane and substrate post-exfoliation. After exfoliation, graphene can be seen on both the exfoliated substrate and the membrane, indicating that some graphene has been torn away from the substrate. Additionally, the graphene quality is in-homogeneous on both sides, as evidenced by the variation in the *D:G* peak and *2D:G* peak intensity ratios for the six representative regions being shown in (a) and (b).

B Appendix: supplementary information for chapter 4

GaAs grown on gr/Ge (111) at different temperatures.

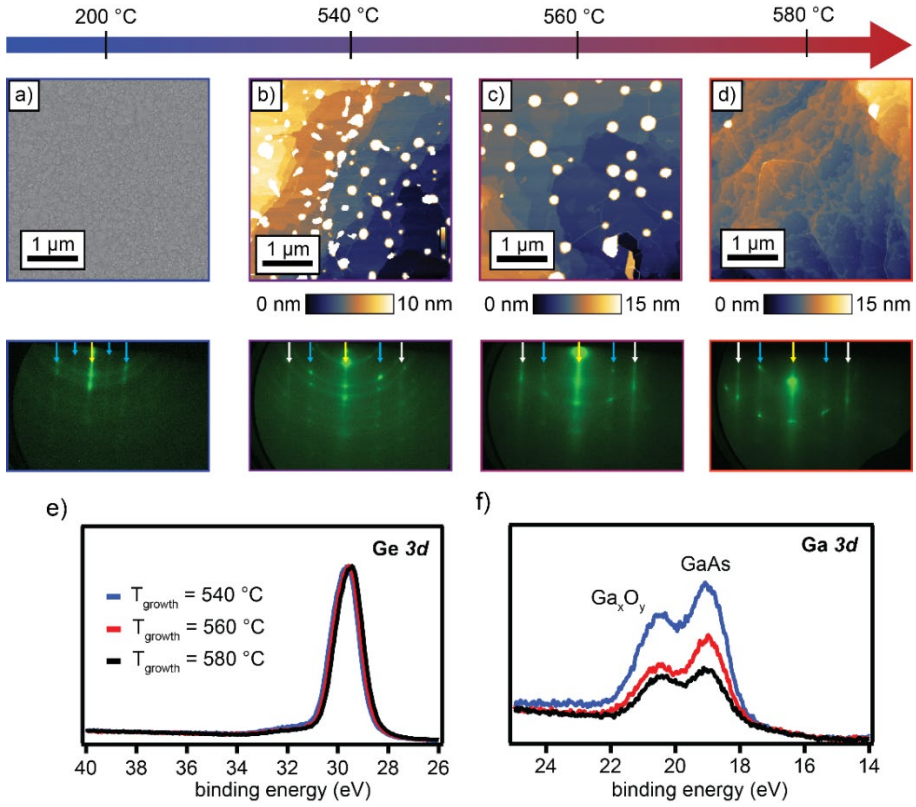

Figure B.1 – Growth of GaAs grown on gr/Ge (111) (nominal thickness = 40 nm) at different temperatures. (a) Secondary electron SEM image and corresponding RHEED pattern along a [11$\bar{2}$] azimuth (yellow arrow – specular, blue arrows – GaAs, white arrow - graphene) of a sample grown at 200 °C, showing a smooth, polycrystalline surface. (b) GaAs grown at 540 °C, showing polycrystalline island nucleation. (c) Growth of GaAs at 560 °C, showing nucleation of spherical particles (d) Growth of GaAs at 580 °C, showing a single-crystalline RHEED pattern along with sparse, spherical islands and smooth features that appear to nucleate at step edges. (e,f) *Ex-situ* photoemission spectra (Al Kα hν =1486.6 eV) of Ge and Ga 3d core levels after GaAs growth at 540, 560 and 580 °C.

We conducted MBE of GaAs on gr/Ge(111) at different temperatures to determine the optimal growth conditions for this system. The graphene was grown via CVD, as described in Ref. [123]. The deposition time was 46 minutes, resulting in an integrated flux of 8.9×10^{16} atoms/cm^2 which corresponds to a nominal thickness of 40 nm for a unity sticking coefficient of Ga. The growth rates were calculated using homoepitaxial GaAs RHEED oscillations (~ 52 nm/h) and the As/Ga flux ratio (21 for all samples) is estimated by reaching the lower bound of the GaAs growth window with a fixed growth temperature while observing RHEED oscillations. Figure B.1 (a-d) shows SEM and AFM images along with RHEED patterns of films grown at 200, 540, 560 and 580 °C. The growth temperatures were measured using a pyrometer calibrated to the GaAs thermal deoxidation temperature.

We find that the sticking of GaAs on graphene/Ge(111) is in fact highly temperature dependent. *Ex-situ* XPS measurements of the Ga 3d core level, normalized to the Ge 3d of the substrate, show that the amount of Ga stuck to the surface decreases as a function of temperature (Fig B.1f). At a growth temperature of 200 °C we see stochastic, polycrystalline nucleation of GaAs, with the graphene surface being completely covered (Fig. B.1a). Therefore, we can assume that the sticking coefficient of Ga on graphene is close to unity at this temperature. At elevated temperatures (> 500 °C), an island growth mode is favored, and AFM

images show a decrease in the island nucleation density and size as the temperature is increased. The 540 and 560 °C growths exhibit a rough surface, and polycrystalline RHEED patterns (Fig. B.1b, c). At a growth temperature of 580 °C, we observe an epitaxial RHEED pattern and nucleation on both the bottom and top of the terrace steps. This result aligns with our hypothesis of nucleation occurring at step edges in clean graphene systems.

The decrease in island nucleation on graphene at elevated temperatures can be explained by increased adatom desorption. *Ex-situ* photoemission spectroscopy (Al Kα = 1486.6 eV) shows a 2x decrease in the intensity of the Ga 3*d* core level from a growth temperature of 540 °C to 560 °C (Figure B.1f). The peaks are normalized to the Ge 3*d* core level to account for any experimental variability (Fig. B.1e). At 580 °C, the Ga 3*d* decreases even further, but only slightly. The secondary component at 20.5 eV corresponds to gallium oxides [205]. The presence of this component is not surprising, since this is an *ex-situ* experiment that involves pulling the sample from ultra-high vacuum post-growth. What is surprising, however, is that our previous EDX experiments highlighted in section 4.3 indicate that the Ga sticking coefficient is not greatly affected by temperature on graphene/MgO. It is not clear why there is a seeming discrepancy between the sticking coefficient of Ga on gr/Ge and gr/MgO, but it could be due to the dirtier, transferred graphene/substrate interface on the MgO substrate. Any contaminant on the surface

would be a highly reactive nucleation site. Another possibility is that “remote interactions” play a role. The ionic bonding of the MgO results in strong potential fluctuations that permeate through the graphene layer, which could enhance the sticking of Ga adatoms on the graphene surface [1,22]. Yet, the EDX results for Ni and Mn do support our photoemission experiments here, which show that higher temperatures result in increased desorption due to graphene’s poor wettability. Further work is needed to determine why different elements exhibit graphene substrate-dependent sticking coefficients.

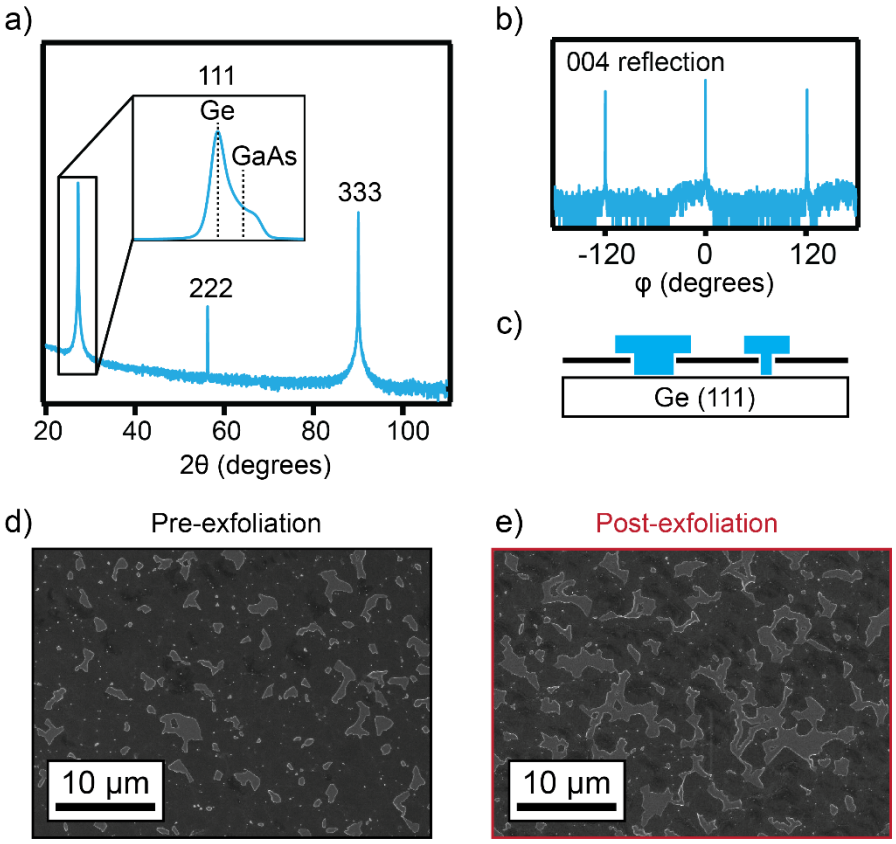

Figure B.2 – Structure and morphology of epitaxy of GaAs on sub-monolayer gr / Ge (111). (a) X-ray diffraction pattern of the film. Inset: High-resolution scan of the Ge 111 reflection. (b) Pole figure φ scans of the 004 reflection, showing the expected 3-fold symmetry of an epitaxial GaAs film. (c) Cartoon depicting epitaxy on sub-monolayer gr / Ge (111). (d) SEM image of the GaAs plate morphology before attempting exfoliation. (e) SEM image of the same GaAs / gr / Ge (111) sample after an exfoliation attempt using Crystalbond and a glass slide.

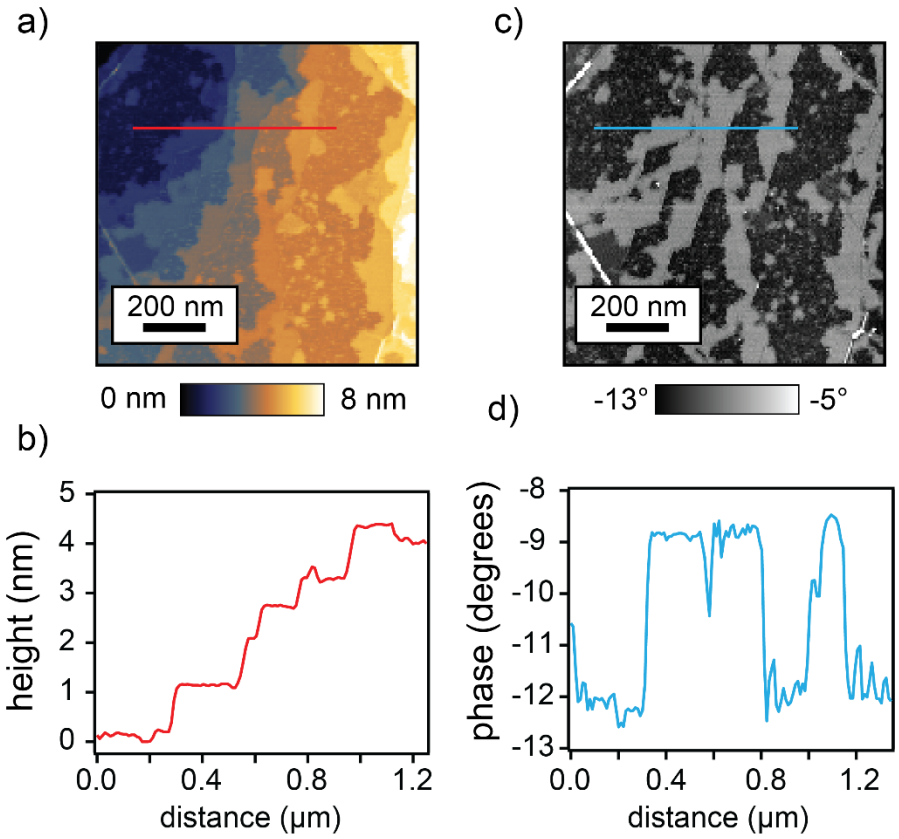

Figure B.3 – GaAs nucleation at the bottom of step edges on gr/Ge (111). (a) AFM height image showing Ge steps and GaAs nucleation. (b) Height profile (red line in (a)) showing GaAs islands are approximately 1 nm thick. (c) AFM phase image of GaAs/gr/Ge(111) growth, showing distinct phase contrast between GaAs and Ge regions. (d) Phase profile (blue line in (c)) of GaAs islands.

References

[1] W. Kong et al., *Polarity Governs Atomic Interaction through Two-Dimensional Materials*, Nat. Mater. **17**, 999 (2018).

[2] Y. Kim et al., *Remote Epitaxy through Graphene Enables Two-Dimensional Material-Based Layer Transfer*, Nature **544**, 340 (2017).

[3] M. König, S. Wiedmann, C. Brüne, A. Roth, H. Buhmann, L. W. Molenkamp, X.-L. Qi, and S.-C. Zhang, *Quantum Spin Hall Insulator State in HgTe Quantum Wells*, Science **318**, 766 (2007).

[4] A. Ohtomo and H. Y. Hwang, *A High-Mobility Electron Gas at the LaAlO3/SrTiO3 Heterointerface*, Nature **427**, 6973 (2004).

[5] R. K. Bhan and V. Dhar, *Recent Infrared Detector Technologies, Applications, Trends and Development of HgCdTe Based Cooled Infrared Focal Plane Arrays and Their Characterization*, Opto-Electron. Rev. **27**, 174 (2019).

[6] M. Yamaguchi, *III–V Compound Multi-Junction Solar Cells: Present and Future*, Sol. Energy Mater. Sol. Cells **75**, 261 (2003).

[7] J. Faist, F. Capasso, D. L. Sivco, A. L. Hutchinson, S.-N. G. Chu, and A. Y. Cho, *Short Wavelength (λ∼3.4 Mm) Quantum Cascade Laser Based on Strained Compensated InGaAs/AlInAs*, Appl. Phys. Lett. **72**, 680 (1998).

[8] A. Koma and K. Yoshimura, *Ultrasharp Interfaces Grown with Van Der Waals Epitaxy*, Surf. Sci. **174**, 556 (1986).

[9] A. K. Geim and K. S. Novoselov, *The Rise of Graphene*, Nat. Mater. **6**, 3 (2007).

[10] G. Gao et al., *Artificially Stacked Atomic Layers: Toward New van Der Waals Solids*, Nano Lett. **12**, 3518 (2012).

[11] S. Manzeli, D. Ovchinnikov, D. Pasquier, O. V. Yazyev, and A. Kis, *2D Transition Metal Dichalcogenides*, Nat. Rev. Mater. **2**, 8 (2017).

[12] K. S. Novoselov, A. Mishchenko, A. Carvalho, and A. H. Castro Neto, *2D Materials and van Der Waals Heterostructures*, Science **353**, aac9439 (2016).

[13] J. R. Schaibley, H. Yu, G. Clark, P. Rivera, J. S. Ross, K. L. Seyler, W. Yao, and X. Xu, *Valleytronics in 2D Materials*, Nat. Rev. Mater. **1**, 11 (2016).

[14] L. Dong, J. Lou, and V. B. Shenoy, *Large In-Plane and Vertical Piezoelectricity in Janus Transition Metal Dichalchogenides*, ACS Nano **11**, 8242 (2017).

[15] Y.-T. Hsu, W. S. Cole, R.-X. Zhang, and J. D. Sau, *Inversion-Protected Higher-Order Topological Superconductivity in Monolayer ${\mathrm{WTe}}_{2}$*, Phys. Rev. Lett. **125**, 097001 (2020).

[16] K. F. Mak, C. Lee, J. Hone, J. Shan, and T. F. Heinz, *Atomically Thin ${\mathrm{MoS}}_{2}$: A New Direct-Gap Semiconductor*, Phys. Rev. Lett. **105**, 136805 (2010).

[17] R. Bistritzer and A. H. MacDonald, *Moiré Bands in Twisted Double-Layer Graphene*, Proc. Natl. Acad. Sci. **108**, 12233 (2011).

[18] H. Guo, N. Lu, L. Wang, X. Wu, and X. C. Zeng, *Tuning Electronic and Magnetic Properties of Early Transition-Metal Dichalcogenides via Tensile Strain*, J. Phys. Chem. C **118**, 7242 (2014).

[19] A. Koma, K. Sunouchi, and T. Miyajima, *Summary Abstract: Fabrication of Ultrathin Heterostructures with van Der Waals Epitaxy*, J. Vac. Sci. Technol. B Microelectron. Process. Phenom. **3**, 724 (1985).

[20] A. Koma, K. Sunouchi, and T. Miyajima, *Fabrication and Characterization of Heterostructures with Subnanometer Thickness*, Microelectron. Eng. **2**, 129 (1984).

[21] Y. Alaskar, S. Arafin, D. Wickramaratne, M. A. Zurbuchen, L. He, J. McKay, Q. Lin, M. S. Goorsky, R. K. Lake, and K. L. Wang, *Towards van Der Waals Epitaxial Growth of GaAs on Si Using a Graphene Buffer Layer*, Adv. Funct. Mater. **24**, 6629 (2014).

[22] J. Yoo et al., *Enhanced Nucleation of Germanium on Graphene via Dipole Engineering*, Nanoscale **10**, 5689 (2018).

[23] X. Sun, Z. Lu, Y. Xiang, Y. Wang, J. Shi, G.-C. Wang, M. A. Washington, and T.-M. Lu, *Van Der Waals Epitaxy of Antimony Islands, Sheets, and Thin Films on Single-Crystalline Graphene*, ACS Nano **12**, 6100 (2018).

[24] P. Periwal, J. D. Thomsen, K. Reidy, G. Varnavides, D. N. Zakharov, L. Gignac, M. C. Reuter, T. J. Booth, S. Hofmann, and F. M. Ross, *Catalytically Mediated Epitaxy of 3D Semiconductors on van Der Waals Substrates*, Appl. Phys. Rev. **7**, 031402 (2020).

[25] K. Reidy, J. D. Thomsen, H. Y. Lee, V. Zarubin, Y. Yu, B. Wang, T. Pham, P. Periwal, and F. M. Ross, *Mechanisms of Quasi van Der Waals Epitaxy of Three-Dimensional Metallic Nanoislands on Suspended Two-Dimensional Materials*, Nano Lett. **22**, 5849 (2022).

[26] J. Li et al., *General Synthesis of Two-Dimensional van Der Waals Heterostructure Arrays*, Nature **579**, 7799 (2020).

[27] K. Zhang, C. Ding, B. Pan, Z. Wu, A. Marga, L. Zhang, H. Zeng, and S. Huang, *Visualizing Van Der Waals Epitaxial Growth of 2D Heterostructures*, Adv. Mater. **33**, 2105079 (2021).

[28] A. K. Geim and I. V. Grigorieva, *Van Der Waals Heterostructures*, Nature **499**, 7459 (2013).

[29] K. S. Novoselov, D. Jiang, F. Schedin, T. J. Booth, V. V. Khotkevich, S. V. Morozov, and A. K. Geim, *Two-Dimensional Atomic Crystals*, Proc. Natl. Acad. Sci. **102**, 10451 (2005).

[30] G. I. Distler, V. P. Vlasov, and V. M. Kanevsky, *Orientational and Long Range Effects in Epitaxy*, Thin Solid Films **33**, 287 (1976).

[31] G. I. Distler, A. N. Lobachev, V. P. Vlasov, O. K. Mel'Nikov, and N. S. Triodina, *Growth of Single Crystals through Interfacial Layers*, J. Cryst. Growth **26**, 21 (1974).

[32] A. V. Kovda, L. L. Aksyonova, G. I. Distler, Y. M. Gerasimov, and E. I. Kortukova, *Growth of Monocrystalline CdS Films on Mica Surfaces through Amorphous Interfacial Layers of Silicon Monoxide and Carbon by Chemical Transport Reactions*, Thin Solid Films **20**, 217 (1974).

[33] K. L. Chopra, *Epitaxial Growth of Films on Substrates Coated with Amorphous Deposits*, J. Appl. Phys. **40**, 906 (2003).

[34] W. K. Morrow, S. J. Pearton, and F. Ren, *Review of Graphene as a Solid State Diffusion Barrier*, Small **12**, 120 (2016).

[35] S. H. Bae et al., *Graphene-Assisted Spontaneous Relaxation towards Dislocation-Free Heteroepitaxy*, Nat. Nanotechnol. **15**, 272 (2020).

[36] R. A. de Groot, F. M. Mueller, P. G. van Engen, and K. H. J. Buschow, *New Class of Materials: Half-Metallic Ferromagnets*, Phys. Rev. Lett. **50**, 2024 (1983).

[37] Z. K. Liu et al., *Observation of Unusual Topological Surface States in Half-Heusler Compounds LnPtBi (Ln=Lu, Y)*, Nat. Commun. **7**, 1 (2016).

[38] J. A. Logan, S. J. Patel, S. D. Harrington, C. M. Polley, B. D. Schultz, T. Balasubramanian, A. Janotti, A. Mikkelsen, and C. J. Palmstrøm, *Observation of a Topologically Non-Trivial Surface State in Half-Heusler PtLuSb (001) Thin Films*, Nat. Commun. **7**, 1 (2016).

[39] Y. Nakajima et al., *Topological RPdBi Half-Heusler Semimetals: A New Family of Noncentrosymmetric Magnetic Superconductors*, Sci. Adv. **1**, e1500242 (2015).

[40] F. F. Tafti, T. Fujii, A. Juneau-Fecteau, S. René de Cotret, N. Doiron-Leyraud, A. Asamitsu, and L. Taillefer, *Superconductivity in the Noncentrosymmetric Half-Heusler Compound LuPtBi: A Candidate for Topological Superconductivity*, Phys. Rev. B **87**, 184504 (2013).

[41] X. Xu, T. Omori, M. Nagasako, A. Okubo, R. Y. Umetsu, T. Kanomata, K. Ishida, and R. Kainuma, *Cooling-Induced Shape Memory Effect and Inverse Temperature Dependence of Superelastic Stress in Co2Cr(Ga,Si) Ferromagnetic Heusler Alloys*, Appl. Phys. Lett. **103**, 164104 (2013).

[42] J. Jiang et al., *Carrier Lifetime Enhancement in Halide Perovskite via Remote Epitaxy*, Nat. Commun. **10**, 1 (2019).

[43] Y. Guo et al., *A Reconfigurable Remotely Epitaxial VO2 Electrical Heterostructure*, Nano Lett. **20**, 33 (2020).

[44] D. Du, S. Manzo, C. Zhang, V. Saraswat, K. T. Genser, K. M. Rabe, P. M. Voyles, M. S. Arnold, and J. K. Kawasaki, *Epitaxy, Exfoliation, and Strain-Induced Magnetism in Rippled Heusler Membranes*, Nat. Commun. **12**, 1 (2021).

[45] H. S. Kum et al., *Heterogeneous Integration of Single-Crystalline Complex-Oxide Membranes*, Nature **578**, 7793 (2020).

[46] Z. Lu, X. Sun, W. Xie, A. Littlejohn, G.-C. Wang, S. Zhang, M. A. Washington, and T.-M. Lu, *Remote Epitaxy of Copper on Sapphire through Monolayer Graphene Buffer*, Nanotechnology **29**, 445702 (2018).

[47] W. Zhu, T. Low, V. Perebeinos, A. A. Bol, Y. Zhu, H. Yan, J. Tersoff, and P. Avouris, *Structure and Electronic Transport in Graphene Wrinkles*, Nano Lett. **12**, 3431 (2012).

[48] A. J. Stone and D. J. Wales, *Theoretical Studies of Icosahedral C60 and Some Related Species*, Chem. Phys. Lett. **128**, 501 (1986).

[49] J. Ma, D. Alfè, A. Michaelides, and E. Wang, *Stone-Wales Defects in Graphene and Other Planar $s{p}^{2}$-Bonded Materials*, Phys. Rev. B **80**, 033407 (2009).

[50] F. Banhart, J. Kotakoski, and A. V. Krasheninnikov, *Structural Defects in Graphene*, ACS Nano **5**, 26 (2011).

[51] H. Kim et al., *Impact of 2D–3D Heterointerface on Remote Epitaxial Interaction through Graphene*, ACS Nano **15**, 10587 (2021).

[52] T. Nishinaga, T. Nakano, and S. Zhang, *Epitaxial Lateral Overgrowth of GaAs by LPE*, Jpn. J. Appl. Phys. **27**, L964 (1988).

[53] Y. Ujiie and T. Nishinaga, *Epitaxial Lateral Overgrowth of GaAs on a Si Substrate*, Jpn. J. Appl. Phys. **28**, L337 (1989).

[54] O.-H. Nam, M. D. Bremser, T. S. Zheleva, and R. F. Davis, *Lateral Epitaxy of Low Defect Density GaN Layers via Organometallic Vapor Phase Epitaxy*, Appl. Phys. Lett. **71**, 2638 (1997).

[55] S. S. Yi, D. M. Hansen, C. K. Inoki, D. L. Harris, T. S. Kuan, and T. F. Kuech, *Lateral Epitaxial Overgrowth of GaSb on GaSb and GaAs Substrates by Metalorganic Chemical Vapor Deposition*, Appl. Phys. Lett. **77**, 842 (2000).

[56] H. Marchand, J. P. Ibbetson, P. T. Fini, S. Keller, S. P. DenBaars, J. S. Speck, and U. K. Mishra, *Mechanisms of Lateral Epitaxial Overgrowth of Gallium Nitride by Metalorganic Chemical Vapor Deposition*, J. Cryst. Growth **195**, 328 (1998).

[57] O. M. J. van 't Erve, A. L. Friedman, E. Cobas, C. H. Li, J. T. Robinson, and B. T. Jonker, *Low-Resistance Spin Injection into Silicon Using Graphene Tunnel Barriers*, Nat. Nanotechnol. **7**, 11 (2012).

[58] W. Li, L. Xue, H. D. Abruña, and D. C. Ralph, *Magnetic Tunnel Junctions with Single-Layer-Graphene Tunnel Barriers*, Phys. Rev. B **89**, 184418 (2014).

[59] M. Heilmann, V. Deinhart, A. Tahraoui, K. Höflich, and J. M. J. Lopes, *Spatially Controlled Epitaxial Growth of 2D Heterostructures via Defect Engineering Using a Focused He Ion Beam*, Npj 2D Mater. Appl. **5**, 1 (2021).

[60] F. Zhang, Y. Wang, C. Erb, K. Wang, P. Moradifar, V. H. Crespi, and N. Alem, *Full Orientation Control of Epitaxial ${\mathrm{MoS}}_{2}$ on HBN Assisted by Substrate Defects*, Phys. Rev. B **99**, 155430 (2019).

[61] A. Hospodková, E. Hulicius, J. Pangrác, F. Dominec, M. P. Mikhailova, A. I. Veinger, and I. V. Kochman, *InAs/GaSb/AlSb Composite Quantum Well Structure Preparation with Help of Reflectance Anisotropy Spectroscopy*, J. Cryst. Growth **464**, 206 (2017).

[62] Z. Y. Liu, T. F. Kuech, and D. A. Saulys, *A Comparative Study of GaSb (100) Surface Passivation by Aqueous and Nonaqueous Solutions*, Appl. Phys. Lett. **83**, 2587 (2003).

[63] Z. Y. Liu, B. Hawkins, and T. F. Kuech, *Chemical and Structural Characterization of GaSb(100) Surfaces Treated by HCl-Based Solutions and Annealed in Vacuum*, J. Vac. Sci. Technol. B Microelectron. Nanometer Struct. Process. Meas. Phenom. **21**, 71 (2002).

[64] C. Cotirlan, R. V. Ghita, C. C. Negrila, C. Logofatu, F. Frumosu, and G. A. Lungu, *Aspects of Native Oxides Etching on N-GaSb(100) Surface*, Appl. Surf. Sci. **363**, 83 (2016).

[65] M. Kodama, J. Hasegawa, and M. Kimata, *Influence of Substrate Preparation on the Morphology of GaSb Films Grown by Molecular Beam Epitaxy*, J. Electrochem. Soc. **132**, 659 (1985).

[66] C. J. Vineis, C. A. Wang, and K. F. Jensen, *In-Situ Reflectance Monitoring of GaSb Substrate Oxide Desorption*, J. Cryst. Growth **225**, 420 (2001).

[67] L. Liu, S. Ryu, M. R. Tomasik, E. Stolyarova, N. Jung, M. S. Hybertsen, M. L. Steigerwald, L. E. Brus, and G. W. Flynn, *Graphene Oxidation: Thickness-Dependent Etching and Strong Chemical Doping*, Nano Lett. **8**, 1965 (2008).

[68] J. D. Thomsen, J. Kling, D. M. A. Mackenzie, P. Bøggild, and T. J. Booth, *Oxidation of Suspended Graphene: Etch Dynamics and Stability Beyond 1000 °C*, ACS Nano **13**, 2281 (2019).

[69] J. Kim, H. Park, J. B. Hannon, S. W. Bedell, K. Fogel, D. K. Sadana, and C. Dimitrakopoulos, *Layer-Resolved Graphene Transfer via Engineered Strain Layers*, Science **342**, 833 (2013).

[70] F. Lukeš, *Oxidation of Si and GaAs in Air at Room Temperature*, Surf. Sci. **30**, 91 (1972).

[71] K. T. He, J. C. Koepke, S. Barraza-Lopez, and J. W. Lyding, *Separation-Dependent Electronic Transparency of Monolayer Graphene Membranes on III−V Semiconductor Substrates*, Nano Lett. **10**, 3446 (2010).

[72] A. J. Way, R. M. Jacobberger, and M. S. Arnold, *Seed-Initiated Anisotropic Growth of Unidirectional Armchair Graphene Nanoribbon Arrays on Germanium*, Nano Lett. **18**, 898 (2018).

[73] S. Xie et al., *Coherent, Atomically Thin Transition-Metal Dichalcogenide Superlattices with Engineered Strain*, Science **359**, 1131 (2018).

[74] Z. Y. Al Balushi et al., *Two-Dimensional Gallium Nitride Realized via Graphene Encapsulation*, Nat. Mater. **15**, 11 (2016).

[75] N. Briggs et al., *Atomically Thin Half-van Der Waals Metals Enabled by Confinement Heteroepitaxy*, Nat. Mater. **19**, 6 (2020).

[76] C. A. Klein and W. D. Straub, *Carrier Densities and Mobilities in Pyrolytic Graphite*, Phys. Rev. **123**, 1581 (1961).

[77] K. Qiao et al., *Graphene Buffer Layer on SiC as a Release Layer for High-Quality Freestanding Semiconductor Membranes*, Nano Lett. **21**, 4013 (2021).

[78] H. Park, C. Lim, C.-J. Lee, J. Kang, J. Kim, M. Choi, and H. Park, *Optimized Poly(Methyl Methacrylate)-Mediated Graphene-Transfer Process for Fabrication of High-Quality Graphene Layer*, Nanotechnology **29**, 415303 (2018).

[79] R. M. Jacobberger and M. S. Arnold, *Graphene Growth Dynamics on Epitaxial Copper Thin Films*, Chem. Mater. **25**, 871 (2013).

[80] S. Manzo, P. J. Strohbeen, Z. H. Lim, V. Saraswat, D. Du, S. Xu, N. Pokharel, L. J. Mawst, M. S. Arnold, and J. K. Kawasaki, *Pinhole-Seeded Lateral Epitaxy and Exfoliation of GaSb Films on Graphene-Terminated Surfaces*, Nat. Commun. **13**, 1 (2022).

[81] S. Ullah, X. Yang, H. Q. Ta, M. Hasan, A. Bachmatiuk, K. Tokarska, B. Trzebicka, L. Fu, and M. H. Rummeli, *Graphene Transfer Methods: A Review*, Nano Res. **14**, 3756 (2021).

[82] G. Lupina et al., *Residual Metallic Contamination of Transferred Chemical Vapor Deposited Graphene*, ACS Nano **9**, 4776 (2015).

[83] Y. Kim et al., *Remote Epitaxy through Graphene Enables Two−dimensional Material−based Layer Transfer*, **544**, 340−343.

[84] B. Kiraly, R. M. Jacobberger, A. J. Mannix, G. P. Campbell, M. J. Bedzyk, M. S. Arnold, M. C. Hersam, and N. P. Guisinger, *Electronic and Mechanical Properties of Graphene–Germanium Interfaces Grown by Chemical Vapor Deposition*, Nano Lett. **15**, 7414 (2015).

[85] R. M. Jacobberger, D. E. Savage, X. Zheng, P. Sookchoo, R. Rojas Delgado, M. G. Lagally, and M. S. Arnold, *Effect of Germanium Surface Orientation*

on Graphene Chemical Vapor Deposition and Graphene-Induced Germanium Nanofaceting, Chem. Mater. **34**, 6769 (2022).

[86] A. Eckmann, A. Felten, A. Mishchenko, L. Britnell, R. Krupke, K. S. Novoselov, and C. Casiraghi, *Probing the Nature of Defects in Graphene by Raman Spectroscopy*, Nano Lett. **12**, 3925 (2012).

[87] R. Beams, L. G. Cançado, and L. Novotny, *Raman Characterization of Defects and Dopants in Graphene*, J. Phys. Condens. Matter **27**, 083002 (2015).

[88] M. D. Bhatt, H. Kim, and G. Kim, *Various Defects in Graphene: A Review*, RSC Adv. **12**, 21520 (2022).

[89] Z. H. Lim, S. Manzo, P. J. Strohbeen, V. Saraswat, M. S. Arnold, and J. K. Kawasaki, *Selective Area Epitaxy of GaAs Films Using Patterned Graphene on Ge*, Appl. Phys. Lett. **120**, 051603 (2022).

[90] J. R. Arthur and A. Y. Cho, *Adsorption and Desorption Kinetics of Cu and Au on (0001) Graphite*, Surf. Sci. **36**, 641 (1973).

[91] I. Lopez-Salido, D. C. Lim, and Y. D. Kim, *Ag Nanoparticles on Highly Ordered Pyrolytic Graphite (HOPG) Surfaces Studied Using STM and XPS*, Surf. Sci. **588**, 6 (2005).

[92] I. N. Stranski, *Zur Theorie des Kristallwachstums*, Z. Für Phys. Chem. **136U**, 259 (1928).

[93] T. Low, V. Perebeinos, J. Tersoff, and Ph. Avouris, *Deformation and Scattering in Graphene over Substrate Steps*, Phys. Rev. Lett. **108**, 096601 (2012).

[94] H. Kuramochi, S. Odaka, K. Morita, S. Tanaka, H. Miyazaki, M. V. Lee, S.-L. Li, H. Hiura, and K. Tsukagoshi, *Role of Atomic Terraces and Steps in the Electron Transport Properties of Epitaxial Graphene Grown on SiC*, AIP Adv. **2**, 012115 (2012).

[95] J. Robinson, X. Weng, K. Trumbull, R. Cavalero, M. Wetherington, E. Frantz, M. LaBella, Z. Hughes, M. Fanton, and D. Snyder, *Nucleation of Epitaxial Graphene on SiC(0001)*, ACS Nano **4**, 153 (2010).

[96] H. Brune, K. Bromann, H. Röder, K. Kern, J. Jacobsen, P. Stoltze, K. msen, and J. No/rskov, *Effect of Strain on Surface Diffusion and Nucleation*, Phys. Rev. B **52**, R14380 (1995).

[97] K. Zhang and M. Arroyo, *Understanding and Strain-Engineering Wrinkle Networks in Supported Graphene through Simulations*, J. Mech. Phys. Solids **72**, 61 (2014).

[98] S. U. Yu, B. Park, Y. Cho, S. Hyun, J. K. Kim, and K. S. Kim, *Simultaneous Visualization of Graphene Grain Boundaries and Wrinkles with Structural Information by Gold Deposition*, ACS Nano **8**, 8662 (2014).

[99] B. Deng et al., *Wrinkle-Free Single-Crystal Graphene Wafer Grown on Strain-Engineered Substrates*, ACS Nano **11**, 12337 (2017).

[100] J. Kim, C. Bayram, H. Park, C.-W. Cheng, C. Dimitrakopoulos, J. A. Ott, K. B. Reuter, S. W. Bedell, and D. K. Sadana, *Principle of Direct van Der Waals Epitaxy of Single-Crystalline Films on Epitaxial Graphene*, Nat. Commun. **5**, 1 (2014).

[101] Y. Kobayashi, K. Kumakura, T. Akasaka, and T. Makimoto, *Layered Boron Nitride as a Release Layer for Mechanical Transfer of GaN-Based Devices*, Nature **484**, 7393 (2012).

[102] D. Du, T. Jung, S. Manzo, Z. LaDuca, X. Zheng, K. Su, V. Saraswat, J. McChesney, M. S. Arnold, and J. K. Kawasaki, *Controlling the Balance between Remote, Pinhole, and van Der Waals Epitaxy of Heusler Films on Graphene/Sapphire*, Nano Lett. **22**, 8647 (2022).

[103] F. Turker et al., *2D Oxides Realized via Confinement Heteroepitaxy*, Adv. Funct. Mater. **33**, 2210404 (2023).

[104] V. O. Shevelev, E. V. Zhizhin, D. A. Pudikov, I. I. Klimovskikh, A. G. Rybkin, V. Yu. Voroshnin, A. E. Petukhov, G. G. Vladimirov, and A. M. Shikin, *Synthesis of Graphene through the Carbidization of Gd on Pyrolytic Graphite*, Phys. Solid State **57**, 2342 (2015).

[105] A. D. Novaco and J. P. McTague, *Orientational Epitaxy---the Orientational Ordering of Incommensurate Structures*, Phys. Rev. Lett. **38**, 1286 (1977).

[106] D. L. Doering, *Rotational Epitaxy of Periodic Overlayers*, J. Vac. Sci. Technol. A **3**, 809 (1985).

[107] C. G. Shaw, S. C. Fain, and M. D. Chinn, *Observation of Orientational Ordering of Incommensurate Argon Monolayers on Graphite*, Phys. Rev. Lett. **41**, 955 (1978).

[108] D. L. Doering and S. Semancik, *Chemisorption and Rotational Epitaxy of Lithium on Ru(001)*, Surf. Sci. **175**, L730 (1986).

[109] Y. Cao, V. Fatemi, S. Fang, K. Watanabe, T. Taniguchi, E. Kaxiras, and P. Jarillo-Herrero, *Unconventional Superconductivity in Magic-Angle Graphene Superlattices*, Nature **556**, 7699 (2018).

[110] K. Badokas, A. Kadys, J. Mickevičius, I. Ignatjev, M. Skapas, S. Stanionytė, E. Radiunas, G. Juška, and T. Malinauskas, *Remote Epitaxy of GaN via Graphene on GaN/Sapphire Templates*, J. Phys. Appl. Phys. **54**, 205103 (2021).

[111] D. Mohanty et al., *Growth of Epitaxial CdTe Thin Films on Amorphous Substrates Using Single Crystal Graphene Buffer*, Carbon **144**, 519 (2019).

[112] X. Sun, Z. Lu, W. Xie, Y. Wang, J. Shi, S. Zhang, M. A. Washington, and T.-M. Lu, *Van Der Waals Epitaxy of CdS Thin Films on Single-Crystalline Graphene*, Appl. Phys. Lett. **110**, 153104 (2017).

[113] J. Jeong et al., *Selective-Area Remote Epitaxy of ZnO Microrods Using Multilayer–Monolayer-Patterned Graphene for Transferable and Flexible Device Fabrications*, ACS Appl. Nano Mater. **3**, 8920 (2020).

[114] J. W. Park et al., *Creation of a Two-Dimensional Electron Gas at an Oxide Interface on Silicon*, Nat. Commun. **1**, 1 (2010).

[115] M. Gajek, M. Bibes, A. Barthélémy, K. Bouzehouane, S. Fusil, M. Varela, J. Fontcuberta, and A. Fert, *Spin Filtering through Ferromagnetic $\mathrm{Bi}\mathrm{Mn}{\mathrm{O}}_{3}$ Tunnel Barriers*, Phys. Rev. B **72**, 020406 (2005).

[116] T. Y. Chien, L. F. Kourkoutis, J. Chakhalian, B. Gray, M. Kareev, N. P. Guisinger, D. A. Muller, and J. W. Freeland, *Visualizing Short-Range Charge*

Transfer at the Interfaces between Ferromagnetic and Superconducting Oxides, Nat. Commun. **4**, 1 (2013).

[117] Z. LaDuca, K. Su, S. Manzo, M. S. Arnold, and J. K. Kawasaki, *Control of Ternary Alloy Composition during Remote Epitaxy on Graphene*, arXiv:2305.07793.

[118] P. J. Strohbeen, S. Manzo, V. Saraswat, K. Su, M. S. Arnold, and J. K. Kawasaki, *Quantifying Mn Diffusion through Transferred versus Directly Grown Graphene Barriers*, ACS Appl. Mater. Interfaces **13**, 42146 (2021).

[119] X. Liu, C.-Z. Wang, M. Hupalo, H.-Q. Lin, K.-M. Ho, and M. C. Tringides, *Metals on Graphene: Interactions, Growth Morphology, and Thermal Stability*, Crystals **3**, 1 (2013).

[120] W. E. McMahon, M. Vaisman, J. D. Zimmerman, A. C. Tamboli, and E. L. Warren, *Perspective: Fundamentals of Coalescence-Related Dislocations, Applied to Selective-Area Growth and Other Epitaxial Films*, APL Mater. **6**, 120903 (2018).

[121] D. J. Ironside, A. M. Skipper, T. A. Leonard, M. Radulaski, T. Sarmiento, P. Dhingra, M. L. Lee, J. Vučković, and S. R. Bank, *High-Quality GaAs Planar Coalescence over Embedded Dielectric Microstructures Using an All-MBE Approach*, Cryst. Growth Des. **19**, 3085 (2019).

[122] H. Kim et al., *Graphene Nanopattern as a Universal Epitaxy Platform for Single-Crystal Membrane Production and Defect Reduction*, Nat. Nanotechnol. **17**, 10 (2022).

[123] G. Wang et al., *Direct Growth of Graphene Film on Germanium Substrate*, Sci. Rep. **3**, 1 (2013).

[124] Y. Zhou and K. P. Loh, *Making Patterns on Graphene*, Adv. Mater. **22**, 3615 (2010).

[125] K. M. McElhinny, R. M. Jacobberger, A. J. Zaug, M. S. Arnold, and P. G. Evans, *Graphene-Induced Ge (001) Surface Faceting*, Surf. Sci. **647**, 90 (2016).

[126] R. D. Bringans, R. I. G. Uhrberg, R. Z. Bachrach, and J. E. Northrup, *Arsenic-Terminated Ge(111): An Ideal 1\ifmmode\times\else\texttimes\fi{}1 Surface*, Phys. Rev. Lett. **55**, 533 (1985).

[127] D. A. Woolf, D. I. Westwood, and R. H. Williams, *The Homoepitaxial Growth of GaAs(111)A and (111)B by Molecular Beam Epitaxy: An Investigation of the Temperature-Dependent Surface Reconstructions and Bulk Electrical Conductivity Transitions*, Semicond. Sci. Technol. **8**, 1075 (1993).

[128] E. Kaxiras, Y. Bar-Yam, J. D. Joannopoulos, and K. C. Pandey, *Ab Initio Theory of Polar Semiconductor Surfaces. I. Methodology and the (22) Reconstructions of GaAs(111)*, Phys. Rev. B **35**, 9625 (1987).

[129] K. W. Haberern and M. D. Pashley, *GaAs(111)A-(2\ifmmode\times\else\texttimes\fi{}2) Reconstruction Studied by Scanning Tunneling Microscopy*, Phys. Rev. B **41**, 3226 (1990).

[130] A. R. Howells, L. Hung, G. S. Chottiner, and D. A. Scherson, *Effects of Substrate Defect Density and Annealing Temperature on the Nature of Pt Clusters Vapor Deposited on the Basal Plane of Highly Oriented Pyrolytic Graphite*, Solid State Ion. **150**, 53 (2002).

[131] S. V. Balakirev, M. S. Solodovnik, I. A. Mikhaylin, M. M. Eremenko, and O. A. Ageev, *Monte Carlo Investigation of the MBE Growth of GaAs on the Surfaces with Different Crystallographic Orientations*, J. Phys. Conf. Ser. **917**, 032034 (2017).

[132] K. Sato, M. R. F. M. R. Fahy, and B. A. J. B. A. Joyce, *The Growth of High Quality GaAs on GaAs (111)A*, Jpn. J. Appl. Phys. **33**, L905 (1994).

[133] M. R. Fahy, K. Sato, and B. A. Joyce, *Reflection High-energy Electron Diffraction Intensity Oscillations during the Growth by Molecular Beam Epitaxy of GaAs (111)A*, Appl. Phys. Lett. **64**, 190 (1994).

[134] T. Yamamoto, M. Inai, T. Takebe, and T. Watanabe, *Pregrowth Treatment Dependence of Surface Morphology for GaAs Grown on Exactly Oriented (111)A Substrates by Molecular-beam Epitaxy*, J. Vac. Sci. Technol. A **11**, 631 (1993).

[135] W. Lee et al., *Confined Monolayer Ag As a Large Gap 2D Semiconductor and Its Momentum Resolved Excited States*, Nano Lett. **22**, 7841 (2022).

[136] N. Briggs, Z. M. Gebeyehu, A. Vera, T. Zhao, K. Wang, A. D. L. F. Duran, B. Bersch, T. Bowen, K. L. Knappenberger, and J. A. Robinson, *Epitaxial Graphene/Silicon Carbide Intercalation: A Minireview on Graphene Modulation and Unique 2D Materials*, Nanoscale **11**, 15440 (2019).

[137] R. S. Weatherup, L. D'Arsié, A. Cabrero-Vilatela, S. Caneva, R. Blume, J. Robertson, R. Schloegl, and S. Hofmann, *Long-Term Passivation of Strongly Interacting Metals with Single-Layer Graphene*, J. Am. Chem. Soc. **137**, 14358 (2015).

[138] J. E. Lee, G. Ahn, J. Shim, Y. S. Lee, and S. Ryu, *Optical Separation of Mechanical Strain from Charge Doping in Graphene*, Nat. Commun. **3**, 1 (2012).

[139] T. Wang, P. Li, M. Gao, Y. Wang, Z. Di, Z. Xue, and M. Zhang, *The Fabrication of Wrinkle-Free Graphene Patterns on Ge(110) Substrate*, Phys. Status Solidi B **258**, 2000560 (2021).

[140] F. Lavini, F. Cellini, M. Rejhon, J. Kunc, C. Berger, W. de Heer, and E. Riedo, *Atomic Force Microscopy Phase Imaging of Epitaxial Graphene Films*, J. Phys. Mater. **3**, 024005 (2020).

[141] E. Malina, *Mechanical Behavior of Atomically Thin Graphene Sheets Using Atomic Force Microscopy Nanoindentation*, Grad. Coll. Diss. Theses (2011).

[142] H. El-Sherif, N. Briggs, B. Bersch, M. Pan, M. Hamidinejad, S. Rajabpour, T. Filleter, K. W. Kim, J. Robinson, and N. D. Bassim, *Scalable Characterization of 2D Gallium-Intercalated Epitaxial Graphene*, ACS Appl. Mater. Interfaces **13**, 55428 (2021).

[143] Y. Dedkov, J. Yang, H. Hu, Y. Jin, M. Yan, Y. Jin, J. Zhou, and E. Voloshina, *Realization of a New Graphene–Ferromagnet Interface with Dirac Linear Band Dispersion*, ACS Appl. Mater. Interfaces **15**, 26190 (2023).

[144] Y. Qi et al., *Unique Transformation from Graphene to Carbide on Re(0001) Induced by Strong Carbon–Metal Interaction*, J. Am. Chem. Soc. **139**, 17574 (2017).

[145] P. Jacobson, B. Stöger, A. Garhofer, G. S. Parkinson, M. Schmid, R. Caudillo, F. Mittendorfer, J. Redinger, and U. Diebold, *Nickel Carbide as a Source of Grain Rotation in Epitaxial Graphene*, ACS Nano **6**, 3564 (2012).

[146] H. Zheng, R. Li, S. Dong, W. Chen, L. Fan, W. Li, P. Zheng, L. Zheng, Y. Zhang, and L. Deng, *Iron Carbide Interface Modulating for Synergies of 3D-Graphene-like and Iron-Coated Fe3O4 Particles for High Microwave Absorption Performance*, J. Alloys Compd. **945**, 169283 (2023).

[147] K. Chu, J. Wang, Y. Liu, Y. Li, C. Jia, and H. Zhang, *Creating Defects on Graphene Basal-Plane toward Interface Optimization of Graphene/CuCr Composites*, Carbon **143**, 85 (2019).

[148] J. L. Dye, *Anionic Electrons in Electrides*, Nature **365**, 6441 (1993).

[149] J. L. Dye, *Electrons as Anions*, Science **301**, 607 (2003).

[150] S. B. Dawes, D. L. Ward, R. He. Huang, and J. L. Dye, *First Electride Crystal Structure*, J. Am. Chem. Soc. **108**, 3534 (1986).

[151] Z. Li, J. Yang, J. G. Hou, and Q. Zhu, *Inorganic Electride: Theoretical Study on Structural and Electronic Properties*, J. Am. Chem. Soc. **125**, 6050 (2003).

[152] J. Chae, J. Lee, Y. Oh, and G. Kim, *First-Principles Study of Two-Dimensional Electron Gas on a Layered ${\mathrm{Gd}}_{2}\mathrm{C}$ Electride Surface*, Phys. Rev. B **104**, 125403 (2021).

[153] S. Y. Lee et al., *Ferromagnetic Quasi-Atomic Electrons in Two-Dimensional Electride*, Nat. Commun. **11**, 1 (2020).

[154] X. Zhang, W. Meng, Y. Liu, X. Dai, G. Liu, and L. Kou, *Magnetic Electrides: High-Throughput Material Screening, Intriguing Properties, and Applications*, J. Am. Chem. Soc. **145**, 5523 (2023).

[155] S. Liu, C. Wang, L. Liu, J.-H. Choi, H.-J. Kim, Y. Jia, C. H. Park, and J.-H. Cho, *Ferromagnetic Weyl Fermions in Two-Dimensional Layered Electride ${\mathrm{Gd}}_{2}\mathrm{C}$*, Phys. Rev. Lett. **125**, 187203 (2020).

[156] S. Hasegawa, *Reflection High-Energy Electron Diffraction*, in *Characterization of Materials* (John Wiley & Sons, Ltd, 2012), pp. 1–14.

[157] A. W. Robertson and J. H. Warner, *Hexagonal Single Crystal Domains of Few-Layer Graphene on Copper Foils*, Nano Lett. **11**, 1182 (2011).

[158] V. Berry, *Impermeability of Graphene and Its Applications*, Carbon **62**, 1 (2013).

[159] Y. Zhao, Y. Xie, Z. Liu, X. Wang, Y. Chai, and F. Yan, *Two-Dimensional Material Membranes: An Emerging Platform for Controllable Mass Transport Applications*, Small **10**, 4521 (2014).

[160] F. Schwierz, *Graphene Transistors*, Nat. Nanotechnol. **5**, 7 (2010).

[161] H.-Y. Kim, C. Lee, J. Kim, F. Ren, and S. J. Pearton, *Graphene as a Diffusion Barrier for Al and Ni/Au Contacts on Silicon*, J. Vac. Sci. Technol. B **30**, 030602 (2012).

[162] C. P. Y. Wong, T. J. H. Koek, Y. Liu, K. P. Loh, K. E. J. Goh, C. Troadec, and C. A. Nijhuis, *Electronically Transparent Graphene Barriers against Unwanted Doping of Silicon*, ACS Appl. Mater. Interfaces **6**, 20464 (2014).

[163] S. Tongay, M. Lemaitre, T. Schumann, K. Berke, B. R. Appleton, B. Gila, and A. F. Hebard, *Graphene/GaN Schottky Diodes: Stability at Elevated Temperatures*, Appl. Phys. Lett. **99**, 102102 (2011).

[164] R. M. Jacobberger, M. J. Dodd, M. Zamiri, A. J. Way, M. S. Arnold, and M. G. Lagally, *Passivation of Germanium by Graphene for Stable Graphene/Germanium Heterostructure Devices*, ACS Appl. Nano Mater. **2**, 4313 (2019).

[165] B. Dlubak et al., *Graphene-Passivated Nickel as an Oxidation-Resistant Electrode for Spintronics*, ACS Nano **6**, 10930 (2012).

[166] J. Kim, S. K. Baek, K. S. Kim, Y. J. Chang, and E. J. Choi, *Long-Term Stability Study of Graphene-Passivated Black Phosphorus under Air Exposure*, Curr. Appl. Phys. **16**, 165 (2016).

[167] D. Jang et al., *Thru-Hole Epitaxy: A Highway for Controllable and Transferable Epitaxial Growth*, Adv. Mater. Interfaces **10**, 2201406 (2023).

[168] M. Zulqurnain, O. J. Burton, M. Al-Hada, L. E. Goff, S. Hofmann, and L. C. Hirst, *Defect Seeded Remote Epitaxy of GaAs Films on Graphene*, Nanotechnology **33**, 485603 (2022).

[169] H. Kum, D. Lee, W. Kong, H. Kim, Y. Park, Y. Kim, Y. Baek, S.-H. Bae, K. Lee, and J. Kim, *Epitaxial Growth and Layer-Transfer Techniques for Heterogeneous Integration of Materials for Electronic and Photonic Devices*, Nat. Electron. **2**, 10 (2019).

[170] H. Yoon et al., *Freestanding Epitaxial SrTiO3 Nanomembranes via Remote Epitaxy Using Hybrid Molecular Beam Epitaxy*, Sci. Adv. **8**, eadd5328 (2022).

[171] E. Cobas, A. L. Friedman, O. M. J. van't Erve, J. T. Robinson, and B. T. Jonker, *Graphene As a Tunnel Barrier: Graphene-Based Magnetic Tunnel Junctions*, Nano Lett. **12**, 3000 (2012).

[172] Y. Chen, X.-L. Gong, and J.-G. Gai, *Progress and Challenges in Transfer of Large-Area Graphene Films*, Adv. Sci. **3**, 1500343 (2016).

[173] S.-J. Yang, S. Choi, F. O. Odongo Ngome, K.-J. Kim, S.-Y. Choi, and C.-J. Kim, *All-Dry Transfer of Graphene Film by van Der Waals Interactions*, Nano Lett. **19**, 3590 (2019).

[174] J. Kang, D. Shin, S. Bae, and B. Hee Hong, *Graphene Transfer: Key for Applications*, Nanoscale **4**, 5527 (2012).

[175] S. S. Roy and M. S. Arnold, *Improving Graphene Diffusion Barriers via Stacking Multiple Layers and Grain Size Engineering*, Adv. Funct. Mater. **23**, 3638 (2013).

[176] J. Yuan, L.-P. Ma, S. Pei, J. Du, Y. Su, W. Ren, and H.-M. Cheng, *Tuning the Electrical and Optical Properties of Graphene by Ozone Treatment for Patterning Monolithic Transparent Electrodes*, ACS Nano **7**, 4233 (2013).

[177] S. Oh, Y. Jung, and J. Kim, *Effects of Defect Density on Ultrathin Graphene-Based Metal Diffusion Barriers*, J. Vac. Sci. Technol. A **33**, 061510 (2015).

[178] X. Y. Dong, C. Adelmann, J. Q. Xie, C. J. Palmstrøm, X. Lou, J. Strand, P. A. Crowell, J.-P. Barnes, and A. K. Petford-Long, *Spin Injection from the*

Heusler Alloy Co2MnGe into Al0.1Ga0.9As/GaAs Heterostructures, Appl. Phys. Lett. **86**, 102107 (2005).

[179] R. Farshchi and M. Ramsteiner, *Spin Injection from Heusler Alloys into Semiconductors: A Materials Perspective*, J. Appl. Phys. **113**, 191101 (2013).

[180] A. C. Ferrari and D. M. Basko, *Raman Spectroscopy as a Versatile Tool for Studying the Properties of Graphene*, Nat. Nanotechnol. **8**, 4 (2013).

[181] S. Doniach and M. Sunjic, *Many-Electron Singularity in X-Ray Photoemission and X-Ray Line Spectra from Metals*, J. Phys. C Solid State Phys. **3**, 285 (1970).

[182] K. W. Edmonds et al., *Mn Interstitial Diffusion in $(\mathrm{G}\mathrm{a},\mathrm{M}\mathrm{n})\mathrm{A}\mathrm{s}$*, Phys. Rev. Lett. **92**, 037201 (2004).

[183] O. Leenaerts, B. Partoens, and F. M. Peeters, *Graphene: A Perfect Nanoballoon*, Appl. Phys. Lett. **93**, 193107 (2008).

[184] N. Li, Z. Zhen, R. Zhang, Z. Xu, Z. Zheng, and L. He, *Nucleation and Growth Dynamics of Graphene Grown by Radio Frequency Plasma-Enhanced Chemical Vapor Deposition*, Sci. Rep. **11**, 1 (2021).

[185] J. Mischke, J. Pennings, E. Weisenseel, P. Kerger, M. Rohwerder, W. Mertin, and G. Bacher, *Direct Growth of Graphene on GaN via Plasma-Enhanced Chemical Vapor Deposition under N2 Atmosphere*, 2D Mater. **7**, 035019 (2020).

[186] R. Vishwakarma, R. Zhu, A. A. Abuelwafa, Y. Mabuchi, S. Adhikari, S. Ichimura, T. Soga, and M. Umeno, *Direct Synthesis of Large-Area Graphene on Insulating Substrates at Low Temperature Using Microwave Plasma CVD*, ACS Omega **4**, 11263 (2019).

[187] A. Srivastava, C. Galande, L. Ci, L. Song, C. Rai, D. Jariwala, K. F. Kelly, and P. M. Ajayan, *Novel Liquid Precursor-Based Facile Synthesis of Large-Area Continuous, Single, and Few-Layer Graphene Films*, Chem. Mater. **22**, 3457 (2010).

[188] B. Zhang, W. H. Lee, R. Piner, I. Kholmanov, Y. Wu, H. Li, H. Ji, and R. S. Ruoff, *Low-Temperature Chemical Vapor Deposition Growth of Graphene from Toluene on Electropolished Copper Foils*, ACS Nano **6**, 2471 (2012).

[189] M. M. Roberts, L. J. Klein, D. E. Savage, K. A. Slinker, M. Friesen, G. Celler, M. A. Eriksson, and M. G. Lagally, *Elastically Relaxed Free-Standing Strained-Silicon Nanomembranes*, Nat. Mater. **5**, 5 (2006).

[190] N. Levy, S. A. Burke, K. L. Meaker, M. Panlasigui, A. Zettl, F. Guinea, A. H. C. Neto, and M. F. Crommie, *Strain-Induced Pseudo–Magnetic Fields Greater Than 300 Tesla in Graphene Nanobubbles*, Science **329**, 544 (2010).

[191] D. Ji et al., *Freestanding Crystalline Oxide Perovskites down to the Monolayer Limit*, Nature **570**, 7759 (2019).

[192] S. S. Hong et al., *Extreme Tensile Strain States in La0.7Ca0.3MnO3 Membranes*, Science **368**, 71 (2020).

[193] D. P. Halliday, J. M. Eggleston, K. Y. Lee, J. E. F. Frost, and S. P. Beaumont, *Optical Properties of Ultrathin 50nm GaAs Membranes*, Solid State Commun. **96**, 359 (1995).

[194] J. L. Snyder, A. Clark, D. Z. Fang, T. R. Gaborski, C. C. Striemer, P. M. Fauchet, and J. L. McGrath, *An Experimental and Theoretical Analysis of Molecular Separations by Diffusion through Ultrathin Nanoporous Membranes*, J. Membr. Sci. **369**, 119 (2011).

[195] D. Z. Fang, C. C. Striemer, T. R. Gaborski, J. L. McGrath, and P. M. Fauchet, *Methods for Controlling the Pore Properties of Ultra-Thin Nanocrystalline Silicon Membranes*, J. Phys. Condens. Matter **22**, 454134 (2010).

[196] D. Sander, S. Ouazi, A. Enders, T. Gutjahr-Löser, V. S. Stepanyuk, D. I. Bazhanov, and J. Kirschner, *Stress, Strain and Magnetostriction in Epitaxial Films*, J. Phys. Condens. Matter **14**, 4165 (2002).

[197] M. Weber, R. Koch, and K. H. Rieder, *UHV Cantilever Beam Technique for Quantitative Measurements of Magnetization, Magnetostriction, and Intrinsic Stress of Ultrathin Magnetic Films*, Phys. Rev. Lett. **73**, 1166 (1994).

[198] E. W. Lee, *Magnetostriction and Magnetomechanical Effects*, Rep. Prog. Phys. **18**, 184 (1955).

[199] E. Callen and H. B. Callen, *Magnetostriction, Forced Magnetostriction, and Anomalous Thermal Expansion in Ferromagnets*, Phys. Rev. **139**, A455 (1965).

[200] Z. Chen et al., *Complex Strain Evolution of Polar and Magnetic Order in Multiferroic BiFeO3 Thin Films*, Nat. Commun. **9**, 1 (2018).

[201] D. Lu, D. J. Baek, S. S. Hong, L. F. Kourkoutis, Y. Hikita, and H. Y. Hwang, *Synthesis of Freestanding Single-Crystal Perovskite Films and Heterostructures by Etching of Sacrificial Water-Soluble Layers*, Nat. Mater. **15**, 12 (2016).

[202] P. Dai, *Antiferromagnetic Order and Spin Dynamics in Iron-Based Superconductors*, Rev. Mod. Phys. **87**, 855 (2015).

[203] B. Lake et al., *Antiferromagnetic Order Induced by an Applied Magnetic Field in a High-Temperature Superconductor*, Nature **415**, 6869 (2002).

[204] J. Zhao et al., *Structural and Magnetic Phase Diagram of CeFeAsO1− XFx and Its Relation to High-Temperature Superconductivity*, Nat. Mater. **7**, 12 (2008).

[205] E. Huber and H. L. Hartnagel, *XPS Analysis of (100) GaAs Surfaces after Applying a Variety of Technology-Etchants*, Solid-State Electron. **27**, 589 (1984).